Ingrid Helene Ellingsen

Internal tides and the spread of river plumes in the Trondheim Fjord

Trondheim, June 2004

Doctoral thesis for the degree of doktor ingeniør

Norwegian University of Science and Technology
Faculty of Engineering Science and Technology
Department of Civil and Transport Engineering

NTNU

URN:NBN:no-3496

Abstract

The Trondheim Fjord receives a substantial amount of freshwater during the year, with a mean runoff of 725 m^3s^{-1} and a spring flood maximum of up to 6430 m^3s^{-1}. How this freshwater spreads and mixes with the ambient presents one of the great challenges in understanding the dynamics of fjord circulation. This problem is approached in the present thesis by performing high-resolution numerical simulations of the physics and circulation of the Trondheim Fjord. The model used is the Navy Coastal Ocean Model (NCOM).

An introductory study is carried out for a river discharge into an idealized basin. The simulations are compared with results from previous studies where laboratory models have been applied to study similar problems.

In the next study the Trondheim Fjord is simulated for different scenarios that include the forcing of river discharges, tides and the effect of the Coriolis force. The simulations show that the river plumes in the fjord are affected by the rotation of the earth, which is to be expected from earlier studies. Further, the internal tide has in certain cases a great influence at the freshwater flow near the surface. These results are used to explain earlier observations of the hydrographic conditions and currents in the Trondheim Fjord.

The NCOM model has also been configured to reproduce the physical circulation in the Trondheim Fjord for a period in April 2002. Different types of data and observations from this period are used to evaluate the model results. Findings from earlier studies are also considered and compared with the results from the high-resolution simulations.

URN:NBN:no-3496

URN:NBN:no-3496

Acknowledgements

This research could not have been completed without the help and guidance of a number of people. First of all I would like to thank my supervisors Dag Slagstad and Karl J. Eidsvik for their advice and support. I owe a special thank to Dag Slagstad for all he has learned me about ocean modelling. He has always been of great help all the times I have been stuck with model problems.

I wish to thank Tom McClimans, SINTEF Fisheries and Aquaculture, for all the interesting discussions related to the physics of river plumes and the physics of fjords in general. His enthusiasm has been of great inspiration and encouragement. I also owe a great thanks to Tom McClimans for spending a lot of time proof reading my thesis.

I would like to thank the TDepartment of Civil and Transport Engineering, and Øyvind Arntsen in particular, for all the help with all sorts of practical problems.

The research presented in this thesis has been a part of the interdisciplinary Strategic University Program MODTEQ (Model based development of technical ecuipement), supported by the Norwegian Research Council. I wish to thank everyone who participated in this project for an interesting and motivating cooperation; Egil Sakshaug and Geir Johnsen at the Department of Biology, Øyvind Tangen Ødegaard, Martin Ludvigsen and Bjørn Sortland at the Department of Marine Technology.

Many thanks to Dr. James O'Brien for his hospitality during my stay at COAPS (Florida State University, Tallahassee) during the spring 2002. I am very grateful to Steve Morey for introducing me to and for all the help with the NCOM model. Thanks also to Paul J. Martin for allowing me to use NCOM. I also wish to thank all the people that made this stay in Tallahassee interesting and fun, both socially and professionally (none mentioned, none forgotten).

Thanks to Statoil ASA for bottom current data from the Trondheim Fjord. I am grateful to Statens Kartverk that has kindly provided tidal data and depth data from the fjord. Thanks also to Kraftverkene I Orkla that provided me temperature data of the Orkla River water and to the Norwegian Water Resources and Energy Directorate (NVE) for river discharge data. The Norwegian Meteorological Institute (Met.no) has provided meteorological data applied in the simulations. CTD data from Station 15 in the Trondheim fjord have kindly been provided by Trondheim biological Station, Departement of Biology.

Thanks to NTNU for local quota at the SGI Origin 3800 and the staff at NOTUR for their support.

I wish also to thank SINTEF Fisheries and Aquaculture and everybody who works there. It has been a great environment to work in, both socially and professionally.

Finally, I would like to thank my friends and family for their support and encouragement. Especially I would like to thank Ole Jacob for his kindness and endless support, and for proof reading my thesis.

Contents

URN:NBN:no-3496

URN:NBN:no-3496

Chapter 1

Introduction

URN:NBN:no-3496

URN:NBN:no-3496

Introduction

The Trondheim Fjord receives a substantial amount of freshwater during the year, with a mean runoff of 725 m^3s^{-1} and a spring flood maximum of up to 6430 m^3s^{-1}. How this freshwater spreads and mixes with the ambient presents one of the great challenges in understanding the dynamics of fjord circulation. This problem is approached in the present thesis by performing high-resolution numerical simulations of the physics and circulation of the Trondheim Fjord (Figure 1.1). The model used is the Navy Coastal Ocean Model (NCOM), a parallelised 3-D, hydrostatic, primitive equation model developed at the U.S. Naval Research Laboratory. The model has been configured for the Trondheim Fjord in cooperation with the Center of Ocean-Atmospheric Prediction Studies (COAPS), Tallahassee, Florida , USA.

The high-resolution simulations have made it possible to study the fjord's "weather", i.e. the eddies and frontal systems in the brackish surface layer in the fjord. The complex physics at this scale of the world's oceans has for instance been demonstrated by a large number of observations of so-called spiral eddies in the sun glitter from space shuttles. Remote sensing such as color sensing satellites further show the great variability of mesoscale and submesoscale processes including fronts, eddies and so forth.

There have been a few previous studies dealing with the physics of freshwater plumes in Norwegian fjords. These studies showed that background rotation has a significant effect on the river plumes formed by freshwater discharges. One example is the freshwater discharge into the Orkdal Fjord, an arm of the Trondheim Fjord This has been one of the cases studied by means of laboratory models. Based on these studies, the NCOM has been applied to simulate similar scenarios.

There are six major rivers transporting freshwater into the Trondheim Fjord and the interactions between different plumes is another subject of my research.

The river plume development and behavior may be influenced by tides. However, the Trondheim Fjord is relatively deep and the barotropic tidal current is not expected to be significant. Yet, there is a great variability during a tidal period of the surface flow and the hydrographic conditions in the Orkdal Fjord, Gaulosen and the Cross Fjord. Patterns at the surface

produced by subsurface phenomena are often observed either as the accumulation of debris, from changes in sea color or from changes in sea surface roughness. The high-resolution simulations performed with NCOM show the same complexity. Some of the processes are reproduced by the simulations and will be shown in this thesis. It will further be shown that the internal (baroclinic) tide influences the transport of freshwater masses near the surface. The effect is significant in some parts of the fjord.

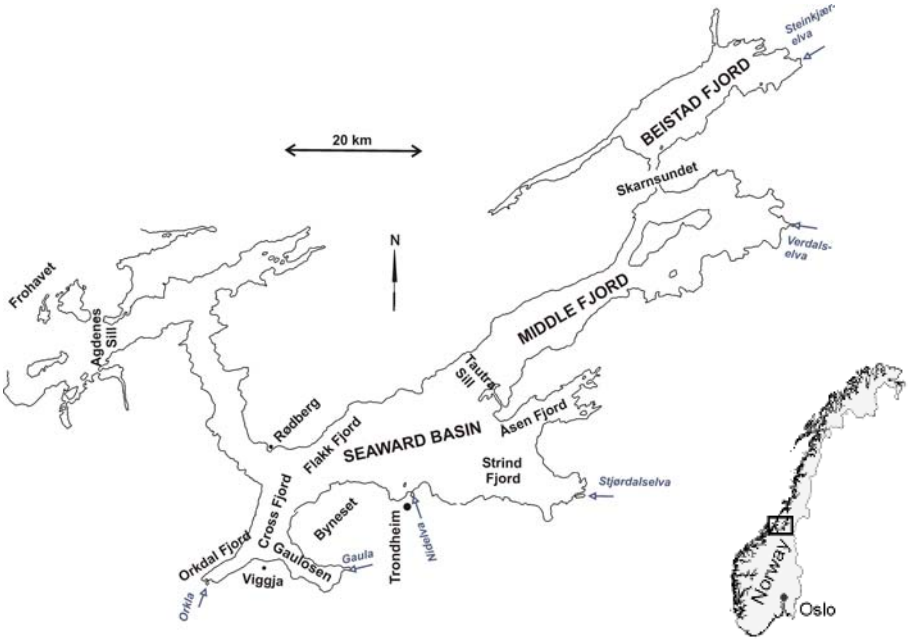

Figure 1.1 The Trondheim Fjord.

Outline of the thesis

Chapter 2 introduces the reader to the physical oceanography of the Trondheim Fjord. Chapter 3 introduces NCOM and the main properties of the model. Chapter 4 describes results from simulations with NCOM for a discharge into a calm ambient in a rectangular basin. This set-up has been run both with and without background rotation. The study focuses on the physical properties of a river plume in an environment like the one in the Trondheim

Fjord. Previous studies of river plumes in the laboratory are used as a reference to evaluate the model results obtained with NCOM. In Chapter 5 a realistic bathymetry of the Trondheim Fjord is introduced. Simulations are run both with and without tides, but are otherwise still to some degree simplified. In Chapter 6 the results are presented where NCOM has been configured to simulate the fjord for April 2002. The model is configured to cover the whole Trondheim Fjord and two configurations of different horizontal grid spacing of 500 m and 100 m are applied. In the high resolution case, the total number of degrees of freedom is of order $O(10^9)$ and 16 processors at a SGI Origin 3800L are used to run the model. In chapters 7 and 8 Observations from April 2002 including both field measurements and aerial photography are used to evaluate how well the model performs for simulating selected fjord processes. Chapter 9 summarizes the main results from the research presented in this thesis.

URN:NBN:no-3496

Chapter 2

The physical oceanography of the Trondheim Fjord

URN:NBN:no-3496

2.1 The physical oceanography of the Trondheim Fjord

Topography

The Trondheim Fjord is the third largest fjord in Norway. It has a surface area of 1420 km^2 and a volume of 235 km^3. The length of the fjord from Agdenes to Steinkjer is approximately 185 km. The deepest seaward sill depth is 217 m (Karl Tangen, personal communication). The fjord has three main basins: the Seaward Basin, the Middle Fjord and the Beistad Fjord. Figure 2.1 shows the bathymetry of the fjord used in the simulations. The same orientation will be applied.

Of the three basins, the Seaward Basin is the largest with a volume of 158 km^3. The Tautra Sill, which is around 77 m at the deepest, separates this basin from the Middle Fjord (Karl Tangen, personal communication). A sill in Skarnsundet, around 140 m deep, separates the two innermost basins. A more thorough description of the topography of the fjord is given in Jacobson (1977).

The estuarine circulation

The Trondheim Fjord has three main fluid layers. The basin water found below sill level is the densest. A less dense intermediate layer, consisting of a mixture of coastal and Atlantic waters, separates this layer from the brackish upper layer. The latter forms as river discharges water mix with surrounding water. There is a substantial amount of freshwater discharged into the fjord each year from the rivers Orkla, Gaula, Nidelva, Stjørdalselva, Verdalselva and Steinkjærelva. The maximum is reached during the spring flood, usually in April/May. A maximum of 6430 $m^3\ s^{-1}$ is found during this period (Sakshaug and Killingtveit, 2000). It is the forcing by river discharges that gives rise to the estuarine circulation. As the buoyant water is driven seaward by the horizontal pressure gradients it mixes with water from below. To maintain continuity, a countercurrent forms beneath the upper brackish layer.

The large discharge of water during the spring flood leads to large density differences between the two uppermost layers (Jacobson, 1977). This is a quite stable situation that inhibits mixing across the pycnocline. The thickness of the upper layer in spring and summer is around 5 - 10 m. In late

summer, or early autumn, the river discharge decreases. Mixing by wind and tides causes the thickness of the upper layer in the Seaward Basin and the Middle Fjord to increase to 10 - 20 m before it breaks down, usually in September. The Beistad Fjord is generally more stratified throughout the year

Exchange with the sea

The meteorological and hydrographic conditions of the sea outside the fjord are important for the exchange between the fjord and the sea. This is well demonstrated by Jacobson (1977; 1983) by showing the high correlation between the depth of the $S = 34$ isohaline at Bud, a station located around 180 km south of the inlet of the Trondheim Fjord, and at Station 15 located right outside Rødberg in the Seaward Basin.

The Norwegian Coastal Current (NCC) transports water of primarily Baltic origin that is mixed with brackish water from fjords on the way northwards along the coast of Norway. During spring the freshwater run off is at its maximum due to melting of snow. The prevailing winds during this time of the year are from the north. The NCC is thus generally shallow and broad. The Atlantic water beneath is accordingly thicker (Sakshaug and Killingtveit, 2000). This is believed to explain a nearly continuous inflow of dense Atlantic water observed in the period from February to June, which replaces the slightly less dense bottom water in the fjord. In late summer/early autumn an inflow of coastal water at intermediate depths is typical. The NCC is generally thicker during this period, due to a prevailing wind from the southwest and downwelling. Water at intermediate depths is observed to flow out of the fjord and replaced by coastal water from the NCC at shallower depths. As this water mixes vertically with the more saline water below, the deep layer is once more exchanged. The deep layer in the Trondheim Fjord is thus replaced twice a year. The residence time of the water masses above sill depth is considerably shorter; about 1 month accoring to Jacobson (1977; 1983).

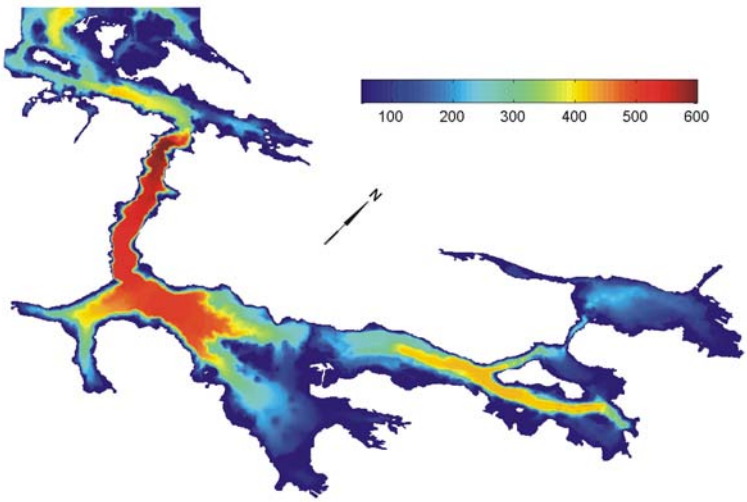

Figure 2.1 The bathymetry of the Trondheim Fjord (depths are given in m).

URN:NBN:no-3496

Tides

The tides in the Trondheim Fjord are semi-diurnal with a mean range of 1.8 m. The dominant components are M_2 and S_2, the semi diurnal Lunar and Solar principal components, respectively. The diurnal Luni-Solar tide contributes to produce a daily difference in the amplitude of the tides in the fjord. The tides are considered to be the dominant energy source of the fjord, nearly 100-1000 times larger than energy supplied by the wind and river discharges (Jacobson, 1983). The barotropic tide in a fjord may loose energy to friction or to internal responses due to interaction between the tides, the stratification and topographical features. The Trondheim Fjord, as most fjords, is generally deep and the barotropic tidally generated current accordingly weak.

Interaction between tides and horizontal and vertical constrictions in topography and stratification may result in the generation of internal tides (internal waves of the same frequency as the external tidal forcing), and in non-linear, high frequency waves. The internal tide and how it contributes to mixing and fjord circulation has been studied by Stacey (1985), Stacey and Pond (1992), Stigebrandt (1976; 1980) and Stigebrandt and Aure (1989). Stacey (1985) and Stacey and Pond (1992) found that in the Knight Inlet in British Columbia (Canada) most of the energy lost from the barotropic tides was lost to the internal tides. More high-frequency waves were also observed, but the energy loss from the tide to these waves was found to be smaller. Tidally generated internal waves are further reviewed in Chaper 5.1.

Surface Currents

Jacobson (1977; 1983) presents two surface current maps for the Trondheim fjord, one for the currents during ebb and one for flood. These maps represent a situation where the tides dominate the flow. For the surface layer, however, the effect of wind stress on the fresh surface layer near to river discharges may induce large velocities, much larger than the tidal currents. The density driven currents formed from the river discharges are also generally stronger than the barotropic tidal currents. Internal tides and waves may also contribute to the surface velocities as will be shown later. The meteorological conditions, river discharges and thus stratification also

change seasonally. The maps by Jacobson are further based on data that are widely spread in time. They are interesting in the sense that they contain information gathered on the surface currents in the Trondheim Fjord during several years.

The surface maps by Jacobson will be compared with simulation results. The results presented in this thesis are from the Seaward Basin and we will focus on this part of the fjord. The surface currents for the Middle Fjord and the Beistad Fjord are found in Jacobson (1977; 1983) and Sakshaug and Killingtveit (2000). Figure 2.2 displays the surface current for the Seaward Basin during ebb and flood. A more or less persistent cyclonic boundary current around the Seaward Basin is seen. The currents are stronger near the basin's northern side during flood tides and along the southern side during ebb. Between these currents and the shore there are vortices of various size and character (these details of the currents are not included in the maps). Away from the shore there are two gyres that dominate the surface currents of the Seaward Basin. One is located near the Strind Fjord. Jacobson (1977) suggests that this gyre generates as the tide turns from flood to ebb. The other cyclonic circulation is found in the area around the shoals north of the Strind Fjord in the eastern part of the basin and the gyre may therefore be topographically bound.

During flood tide these gyres are of comparable sizes and strengths. As the tides turn to ebb, however, the gyre located near the Strind Fjord is greatly reduced by the strong incoming tidal current along the coast of Fosen. The other circulation increases slightly in area and is displaced further to the south.

In the Cross Fjord, water is observed to flow inwards along the western shore of the fjord during flood. This flow continues partly into the Orkdal Fjord. Both during ebb and flood, the flow is outward along the southeastern shore of the Orkdal Fjord. The flow continues to follow the shore on the right hand side out of the fjord and into Gaulosen. East of Viggja, there are two branches of the current, one into Gaulosen and one in a more northerly direction. There is a flow out of Gaulosen along the fjord's northern shore that continues out of the Cross Fjord along the coast of Byneset. The outflow along this coast is stronger and broader during flood than ebb. The current

map also includes an eddy that is located right at the outlet of Orkdal Fjord during flood but moves towards Gaulosen as the tide falls.

The current maps just described for the Cross Fjord, Gaulosen and the Orkdal Fjord are based on measurements of hygrography and currents during 24 and 25 June 1975. The variation of the different water masses in this area is shown in Figure 2.3. The low salinity measured at 1 m depth shown in this figure indicates a high discharge rate from the Gaula and Orkla rivers that transport freshwater into Gaulosen and the Orkdal Fjord, respectively. This figure further demonstrates how the discharge from this river forms river plumes that are trapped to the shore by the Coriolis effect. This will be discussed further in the next chapter.

a)

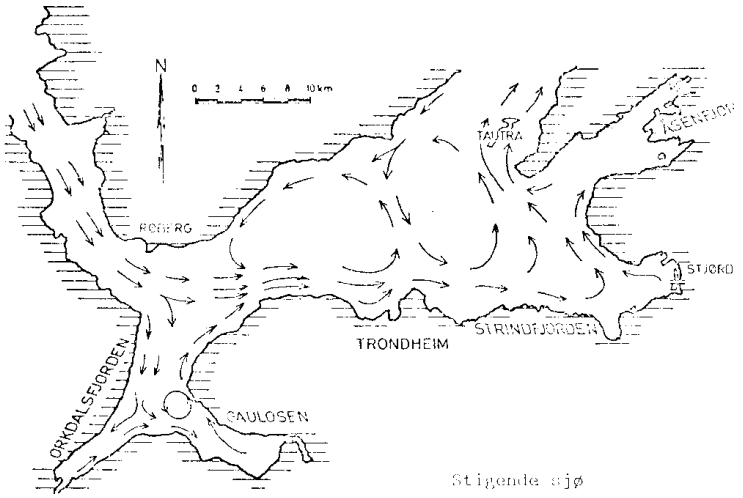

b)

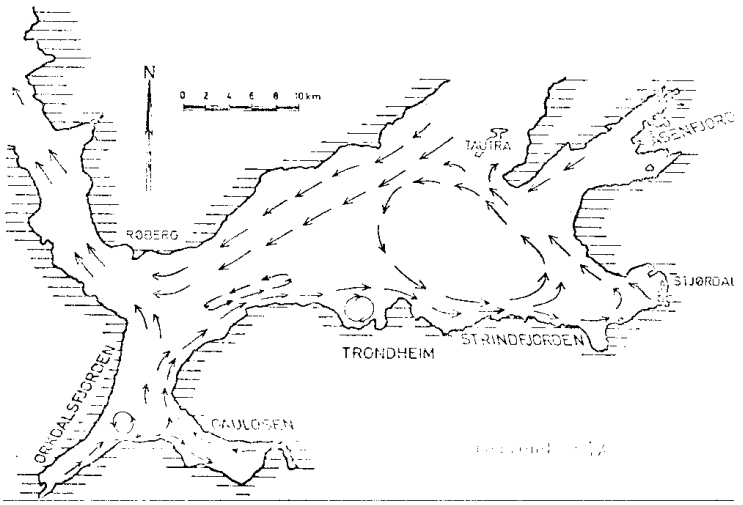

Figure 2.2 The surface current map for the Seaward Basin for **a)** flood and **b)** ebb. The figure is from Jacobson (1977,1983).

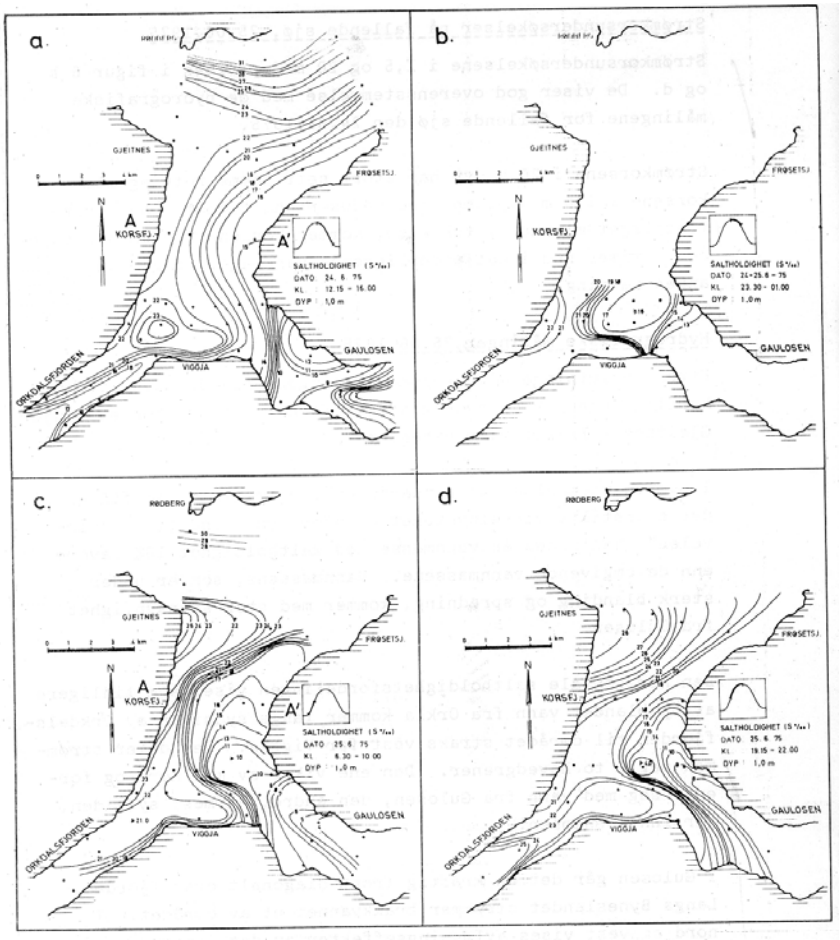

Figure 2.3 Salinity at 1 m depth measured 24 and 25 June 1975. The contours are drawn for different stages of the tidal cycle (Jacobson , 1977).

URN:NBN:no-3496

Chapter 3

The Navy Coastal Ocean Model (NCOM)

URN:NBN:no-3496

3.1 Introduction

The Navy Coastal Ocean Model (NCOM) was developed at the Naval Research Laboratory (NRL), USA, (Martin, 2000). It is a parallelized three-dimensional primitive equation ocean model. The model has been implemented and tested for use in the Trondheim Fjord during my stay at the Center of Ocean-Atmospheric Prediction Studies (COAPS) at Florida State University, USA, where it for instance has been used for high-resolution simulations of the Gulf of Mexico (Morey et al., 2003). The NCOM has some properties that differ from other ocean models and which make it suitable for modelling the Trondheim Fjord. The parallellization has further made it possible to run the model with a horizontal grid spacing of 100 m over the entire fjord. To run this particular case, a total of 16 processors at the SGI Origin 3800L machine at NTNU have been used.

3.2 The Basic Equations

NCOM is based on the primitive equations. We will present the equations here in a Cartesian coordinate system. The primitive equations are Reynolds-averaged to exclude turbulent variations of the quantities at small time scales. There are two main assumptions made to derive the equations: the hydrostatic and Boussinesq approximations. Both are widely applied in numerical models used to study the physical oceanography of the ocean. The hydrostatic approximation requires that the vertical acceleration is much smaller than the horizontal accelerations, so that it can be neglected. This leaves only the pressure term and the buoyancy term in the vertical component of the momentum equation, i.e. the hydrostatic equation. (Equation (3.3)). The equation thus expresses a balance between the pressure and the weight of the fluid. The major benefit obtained by applying this assumption is a simpler set of equations that is computationally more efficient to solve numerically. It is not generally valid, however, for a variety of phenomena and processes. High frequency internal waves, internal bores, and the head of gravity currents are among these.

In the Boussinesq approximation, the difference in density is neglected in all terms except in the gravity term. This assumption is generally considered to be valid for most studies of ocean physics (Gill, 1982).

The set of primitive equations consists of the non-linear Reynolds momentum equations (3.1 and 3.2), the hydrostatic equation (3.3), the equation of continuity (3.4) and the conservation equations for heat and salt (3.5 and 3.6). The density (3.7) is calculated using the formulation by Mellor (1991).

Equation Chapter 3 Section 3

$$\frac{\partial u}{\partial t} = -\nabla\bullet(\mathbf{v}u) + Qu + fv - \frac{1}{\rho_0}\frac{\partial p}{\partial x} + F_u + \frac{\partial}{\partial z}(K_M \frac{\partial u}{\partial z}) \tag{3.1}$$

$$\frac{\partial v}{\partial t} = -\nabla\bullet(\mathbf{v}v) + Qv - fu - \frac{1}{\rho_0}\frac{\partial p}{\partial y} + F_v + \frac{\partial}{\partial z}(K_M \frac{\partial v}{\partial z}) \tag{3.2}$$

$$\frac{\partial p}{\partial z} = -\rho g \tag{3.3}$$

$$\frac{\partial u}{\partial x} + \frac{\partial v}{\partial y} + \frac{\partial w}{\partial z} = Q \tag{3.4}$$

$$\frac{\partial T}{\partial t} = -\nabla\bullet(\mathbf{v}T) + QT + \nabla_h (A_H \nabla_h T) + \frac{\partial}{\partial z}(K_H \frac{\partial T}{\partial z}) + Q_h \tag{3.5}$$

$$\frac{\partial S}{\partial t} = -\nabla\bullet(\mathbf{v}S) + QS + \nabla_h (A_H \nabla_h S) + \frac{\partial}{\partial z}(K_H \frac{\partial S}{\partial z}) \tag{3.6}$$

$$\rho = \rho(T, S, z) \tag{3.7}$$

The source/sink volume variable, *Q*, is used to specify river discharges. The notation is given in Table 3.1.

Boundary conditions

The free surface is subject to both surface stresses and fluxes between the ocean and atmosphere. A new subroutine calculating the heat flux is added to the NCOM to be used in the Trondheim Fjord simulations. This routine calculates the heat flux based on meteorological data, local surface temperature and solar radiation. The stresses at the bottom, $z = H(x, y)$, are

parameterized by a quadratic drag law. Fluxes of salt and heat are set equal to zero at solid boundaries.

Table 3.1 Notation

x, y, z	Cartesian coordinates
σ	Transformed vertical coordinate
ζ	Surface elevation
H	Depth
$v = (u, v, w)$	Velocity components in *x*, *y*, and *z* directions, respectively.
f	The Coriolis parameter
ρ, ρ_0	Density, reference density
p	Pressure
g	Gravity
K_H	Vertical eddy diffusivity
K_M	Vertical eddy viscosity
A_H	Horizontal eddy diffusivity
A_M	Horizontal eddy viscosity
F_u, F_v	Horizontal diffusion terms (Laplacian)
S	Salinity
T	Temperature
Q	Volume source/sink
Q_h	Heatflux rate at the surface
∇_h	Horizontal gradient operator

Open boundary conditions

The NCOM model provides several choices for treatment of open boundaries. The choice made for the Trondheim Fjord simulations is a radiation boundary condition of the Orlansky type, (e.g. Tang et al., 1996).

Horizontal and vertical mixing

The advection scheme applied for the simulations is a third-order upwind scheme (Holland et al., 1998). It keeps overshooting effects at a minimum

and dissipation reasonably small. It has proven to work well in the Trondheim Fjord simulation; frontal regions where the gradients are large are well preserved. The scheme also includes biharmonic diffusive terms that smoothes grid scale noise and presents physical subgrid scale mixing processes. The Laplacian horizontal mixing terms, F_u and F_v are therefore set to zero for the simulations presented in the following chapters.

The vertical mixing parameterization used in the computations is the level $2\,{}^1/_2$ turbulence closure scheme by Mellor and Yamada (1982).

3.3 Model numerics

The variables in NCOM are staggered horizontally and vertically according to the Arakawa C-grid. NCOM applies a combination of σ level and z level vertical grids with σ layers to a user specified depth and from this depth, z levels down to the bottom. At least one σ layer is needed at the surface to allow changes in the surface elevation. In the σ layer part, the water volume is divided into a fixed number of layers that are assigned some fraction of the total depth. The coordinate transformation is given by

$$\sigma = \frac{z - \zeta}{\zeta - \max(H, z_\sigma)}.$$

The water depth is here $z = H$, ζ the surface elevation and $z = z_\sigma$ is the depth that defines the transition from σ layers to *z* layers.

The σ-coordinate resolves topography better than the *z* coordinate. The disadvantage of using the σ coordinate is that errors may occur when calculating horizontal pressure gradients in regions where the bottom slopes steeply. A correction is employed to reduce this problem, following a procedure by Blumberg and Mellor (1987).

The topography in the Trondheim Fjord is very steep. At the same time a high resolution in the surface is needed to resolve the fresh upper layer. To avoid problems that the σ coordinate has in combination with steep topography, the total thickness of the σ levels is chosen to be only 6 m in the simulations presented here.

Internal waves are not exactly represented by σ coordinate or z coordinate and this may cause artificial vertical diffusion. This is of importance for the Trondheim Fjord simulations where there is an abundance of internal waves.

Temporal Differencing

The leapfrog scheme is used for temporal differencing except for some terms that are treated implicitly to avoid time step restrictions. To filter noise produced by the second order leapfrog scheme, an Asselin filter is applied (*Martin*, 2000).

Chapter 4

On river plumes in a rectangular basin

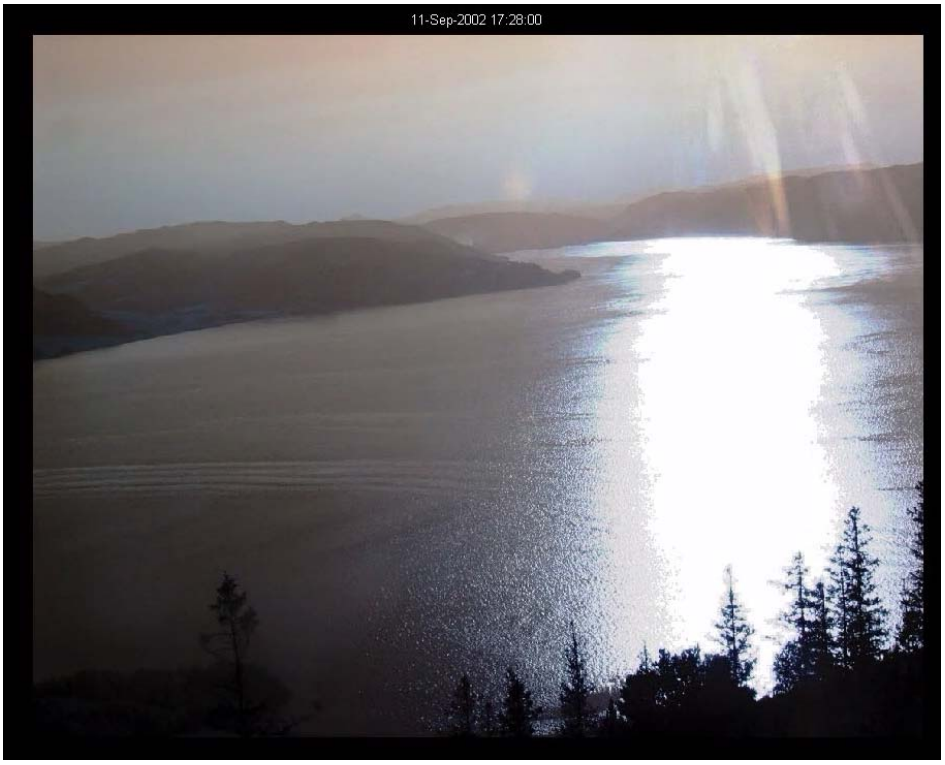

Internal waves observed in the Cross Fjord, near the inlet of Gaulosen. The photo is taken from Byneset looking toward Viggja to the left and the Orkdal Fjord to the right.

Abstract

The development of river plumes in a rectangular basin has previously been modeled in the laboratory. This work has motivated a similar study using the Navy Coastal Ocean Model (NCOM). The rectangular basin and the discharge have been given a scale based on the Orkdal Fjord, one of the arms of the Trondheim Fjord. The results show that different flow regimes occur as the river plume develops. Background rotation is further found to significantly effect the river plume behavior. Similar results were obtained from laboratory modeling. Another problem considered is freshwater discharge into a stratified ambient.

Keywords: river plume, jet, 2-D channel flow, internal hydraulic jump, internal waves, anticyclonic circulation.

4.1 Introduction

River plumes form in fjords when freshwater is discharged into a more saline, and hence a more dense, ambient. There may also be differences in temperature, but this has only a comparatively small effect on the resulting density. The river plume development and behavior is here studied in an idealized fjord environment. The Navy Coastal Ocean Model (NCOM) has been used to simulate discharge of freshwater at a constant rate into a calm ambient in a basin with a rectangular cross section. Numerical simulations are performed both with and without background rotation. Furthermore, the effect of introducing a stratified ambient is studied. The development and behavior of river plumes in a rectangular basin has been studied by Eidnes (1982) and McClimans (1979;1980) using laboratory models. Their results will be compared qualitatively with simulation results.

4.2 Background

Subcritical and supercritical flow in river plumes

River plumes are characterized by the non-dimensional densimetric Froude number *F*. For a two-layer deep fjord *F* is given by

$$F = \frac{U}{\sqrt{g'h}} \tag{4.1}$$

where *U* is a characteristic velocity, *h* is the plume thickness, and $c = \sqrt{g'h}$ is the phase velocity of long interfacial waves. The reduced gravity is given by $g' = g(\rho_2 - \rho_1)/\rho_2$ where *g* is the acceleration due to gravity, ρ_1 is the density of the upper layer and ρ_2 the density of the lower layer. A flow is known to be supercritical when $F > 1$, subcritical when $F < 1$, and critical when $F = 1$. An internal hydraulic jump occurs when the fluid transforms from a supercritical to a subcritical flow and energy dissipation and mixing may be involved (Baines, 1995).

Field studies of a variety of river plumes report supercritical conditions at the leading front (Garvine, 1984; Luketina and Imberger, 1987; Marmorino and Trump, 2000; McClimans, 1978; O'Donnell, 1998; Pritchard and Huntley, 2002). Many of these are studies of fronts of plumes formed from a tidally regulated buoyant outflow. The plumes have thus only a few hours in

which to develop. The conditions of the plume and the front may change if the river plume is allowed to develop over time. In a deep fjord such as the Trondheim Fjord the tidal velocities are generally weak. There are further no topographical restrictions near the river mouths that suggest a similar regulation of the freshwater outflow to the Trondheim Fjord. There may, though, be other processes influencing the development of the freshwater plumes in the fjord. This will be discussed further in the next chapter. I will here consider the general situation where a river plume forms and develops under a constant discharge rate into a calm ambient. The leading front, that immediately forms as the freshwater is transported into the basin, will propagate farther and farther away from the source. During this process the properties of the front and the plume change. McClimans (1994) discusses this situation in terms of the near and far field of river plumes. The near field is characterized by a supercritical Froude number and the energetics are dominated by the inflow of buoyant river water. In the far field, other conditions such as wind and tides are more important for the mixing between the river water and the ambient fjord water. The far field is further characterized by subcritical flow.

Fjords are generally stratified. A freshwater discharge into a stratified ambient represents a more complex situation than the case with discharges into a homogenous environment. Internal waves and internal bores (propagating internal hydraulic jumps) are further commonly generated when a gravity current propagates into a stratified ambient (Simpson, 1997).

Maxworthy et al. (2002) consider dense gravity currents propagating into a linearly stratified ambient. Results are presented both from laboratory and numerical modelling. Supercritical gravity currents were observed to slow down monotonically after an initial phase where the current propagated at a constant velocity. This was explained from generation of an energetic primary wave that removed energy from the gravity current. A different behaviour was observed in subcritical cases where the velocity of the nose of the current was found to oscillate. The leading edge of the current slowed down as the trough of the first wave passed but reinforced again as the current interacted with the crest of a second wave.

Mixing

Mixing between discharged freshwater and the denser ambient may occur already in the river channel or right at the outlet (Luketina and Imberger, 1987). When the freshwater enters the more dense ambient, a frontal boundary immediately forms with large gradients in both density and cross-frontal velocity. The surface flow decelerates toward the frontal boundary. By continuity, this horizontal convergence of the flow at the front leads to downwelling. Water ahead of the plume is thus transported toward the front and sinks along it. During this process mixing occurs between the water masses, as observed by Garvine (1984). The mixture of water produced has a lower velocity than the fresher plume water and forms a return flow relative to the plume. This secondary circulation pattern of the river plumes is for instance discussed in McClimans (1978; 1994). Britter and Simpson (1978) discuss the processes of mixing along a freshwater front based on laboratory models of gravity currents. Their study showed that at the leading slope of the wegde-shaped gravity current head, Kelvin Helmholtz billows were formed resulting in mixing between plume water and the ambient. Mixing was further found to increase the densimetric Froude number at the front.

There are also other processes that may result in mixing between the plume and the ambient. The three dimensional shape of the river plume may consist of both supercritical and subcritical flow regime. Garvine (1984) developed a numerical model of a buoyant surface plume that spreads radially from a continuous source. The front in this model was treated as a discontinuity, while the rest of the flow was treated as inviscid, where the gravitational spreading was dominated by non-linear internal waves (non-linear shallow water equations). The model results showed the development of two flow regimes. One was a circular regime bounded by the leading front and an internal hydraulic jump that developed behind it. This internal hydraulic jump formed as a consequence of an interfacial wave interaction. Internal waves travelling from the source coalesced with waves that were generated earlier in the plume and that had been reflected from the leading front. The second regime was a spreading regime where the thickness sloped gently from a minimum value in front of the internal jump and to an initial value at the discharge point. Thus, Garvine proposed two regions of mixing

within the river plume, one at the leading front and one in connection with the internal hydraulic jump behind the leading front. The results were found to fit well with high-resolution measurements of a river plume front by Pritchard and Huntley (2002). A similar feature is also seen in laboratory simulations (McClimans, 1978). Two photographs from his experiment with a freshwater discharge into a basin with an upper brackish layer are shown in

Figure 4.2. The figure illustrates how the upper brackish layer is entrained into the plume and then transported underneath it toward the left. A vortex entrains the brackish water transported into the region with the return flow. The numerical simulations presented in this chapter exhibit some of the same structure, even though of a different scale.

Influence of the rotation of the earth

River plumes in fjords may be influenced by background rotation as shown by Eidnes (1982) and McClimans (1980). Some of these results are given below. This influence is quite important as it affects the development of the river plume and consequently the mixing between the plume and the ambient.

When considering the effect of background rotation on river discharges, there are two radii of interest, the inertia radius, Equation (4.2), and the baroclinic Rossby deformation radius, Equation (4.3).

(4.2) $$r_i = \frac{U}{f}$$

(4.3) $$r_o = \frac{\sqrt{g'h}}{f}$$

U is a characteristic velocity, g' is the reduced gravity and h is a characteristic thickness as defined above. Equation (4.2) is the radius of influence that the background rotation has on a jet while Equation (4.3) gives information about the rotation effect upon an interfacial wave with phase velocity $c = \sqrt{g'h}$. Note further that the ratio between the two radii is the same as the densimetric Froude number.

(4.4) $$F = \frac{r_i}{r_o} = \frac{U}{\sqrt{g'h}}$$

Thus, a smaller baroclinic Rossby radius than inertial radius accordingly characterises a supercritical river plume, while it is the other way around for subcritical plumes. The flow closest to the inlet of the buoyant discharge has the character of a jet. Such a current may turn according to the inertial radius, as found by McClimans (1979; 1980). As the flow turns and hits the shore on the right hand side, a density driven current trapped to the shore is formed, driven by buoyancy, in the direction of Kelvin Wave propagation. The width of this current is of the same scale as the baroclinic Rossby deformation radius.

Garvine (1995) introduced a system to characterise river plumes in general based on the non-dimensional Kelvin number, *Ke.* This number is the ratio of an across–shore length scale to the baroclinic Rossby deformation radius.

(4.5) $$Ke = \frac{L}{r_o}$$

A small-scale discharge is characterized by $Ke \ll 1$ and a large-scale discharge by $Ke \gg 1$. In the former case, the Coriolis effect is negligible while it is an important part of the dynamics in the latter. These two classes of river discharges have both their characteristic properties and many features in common within each class. When $Ke \approx 1$, however, the dynamics is more complicated and may share properties and features with the above two classes. Let us first consider a discharge into a basin with a straight coast where $Ke \gg 1$. In this case the river plume will develop two distinct dynamical regions. A bulge region with anticyclonic circulation near the river outlet or estuary mouth develops and a density driven coastal current is established in the direction of Kelvin wave propagation farther downstream (see for instance Fong (1998) and references therein). An anticyclonic circulation is also observed in gulf-type basins with large freshwater discharge (Fujiwara et al., 1997; James 1997). This has also been observed in the Orkdal Fjord (McClimans, 1979). The significance of this circulation is that it recirculates the discharged freshwater. Further, as pointed out by Fujiwara et al. (1997) and shown by James (1997), this circulation may also influence the direction of subsequent discharges. They further suggest two different mechanisms for the generation of this type of circulation found in gulf type basins forced by river discharges. Fujiwara et al. (1997) apply a

two-layer model to show that an anticyclonic circulation was necessary for the potential vorticity to be conserved in a system where the discharge causes the development of an estuarine circulation. James (1997) on the other hand showed by numerical simulation that anticyclonic circulation is formed even with a small vertical diffusivity. He found that the anticylonic circulation observed was analogous to the bulge region of river plumes associated with large Kelvin numbers, and is thus due to a geostrophic adjustment process. For the discharges located around the Trondheim Fjord the Kelvin number is generally expected to be close to 1, i.e. the width of the density driven current formed from the discharge is of the same scale as the baroclinic Rossby deformation radius (McClimans, 1980). The plumes may then according to Garvine (1995) exhibit features of both the case in which the effect of Coriolis is large and the other where the rotation only has a negligible effect on the dynamics in an open ocean. The simulations presented here show that even though the earth rotation significantly changes the development of the river plumes, they still exhibit many of the properties found for plumes when rotation is not included.

The Orkla River Plume

The Orkla River Plume (ORP) has its origin in the freshwater runoff from the Orkla River at the head of the Orkdal Fjord. This is a relatively small arm of the Trondheim Fjord with a width of about 2 km and a length of about 7 km before it widens into the Cross Fjord. In 1977 a field study of this area was carried out by McClimans (1979). The results showed that even though the freshwater from the river is transported toward the northwestern side, the plume deflects to the right and leaves the fjord along the other side. Near the river mouth an anticyclonic circulation was found. The fluorescent tracer Rhodamine was added to the river water and then traced over a period of 3 days. A distribution of Rhodamine in the Orkdal Fjord is shown in Figure 4.1. The dynamics strongly indicated an effect of the rotation of the earth. To study this further, laboratory experiments were performed in a rotating basin (Eidnes, 1982; McClimans, 1983). The river plume flow was visualised by adding colour to the river water. Two photos of the river plume flow are shown in Figure 4.3. More results from these laboratory simulations are

shown in Figure 4.4. Figures 4.3 a) and 4.4 a) display the results in cases of no background rotation. Two instabilities of the flow were observed. Small-scale eddies were generated as a result of shear instability on both sides of the plume. As time progressed the whole plume meandered. This meandering was not observed when background rotation was introduced. The behaviour of the plume in this case is shown in Figure 4.3 b) and Figure 4.4 b) and c). When rotation is included we see that the plume is diverted across the fjord and produces an anticyclonic circulation to the right of the discharge, confined between the plume and the walls of the basin. McClimans (1983) further showed that the radius of the anticyclonic backwater circulation scales as the inertia radius, while the width of the resulting coastal current can be determined from the Rossby radius of deformation.

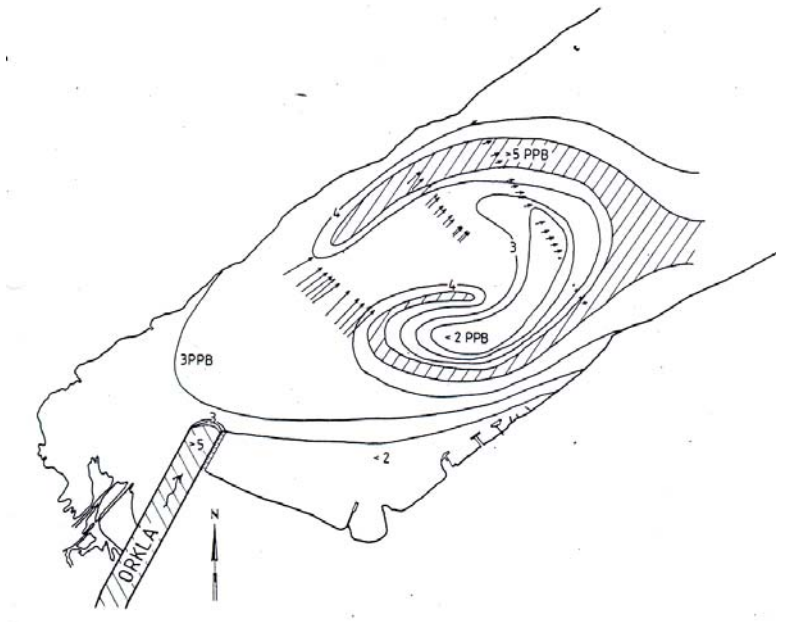

Figure 4.1 The horizontal distribution of Rhodamine concentration in the Orkdal Fjord (McClimans, 1979).

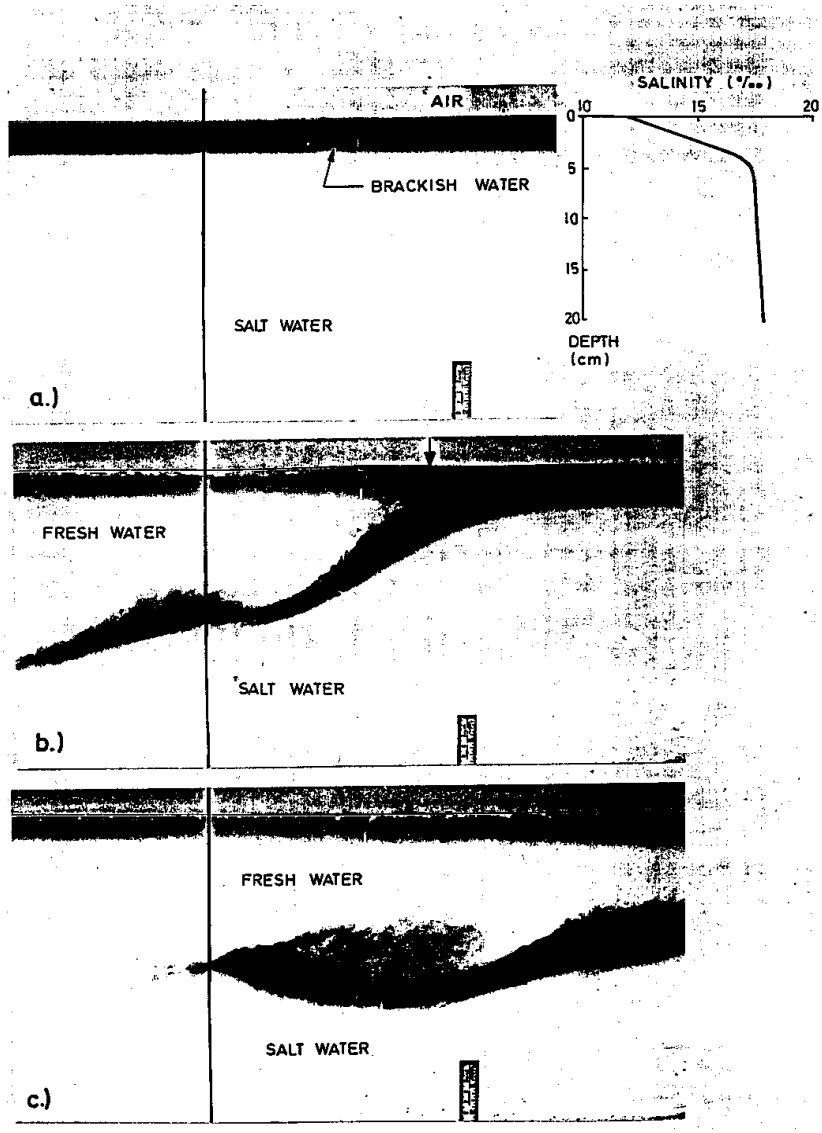

Figure 4.2 A river plume propagate into a two a stratified ambient (McClimans, 1988). The initial stratification is shown in **a)** where the upper layer is coloured. The head of the plume is shown in **b)**. The snap shot in **c)** is taken at a later time and shows the vertical overturning behind the front.

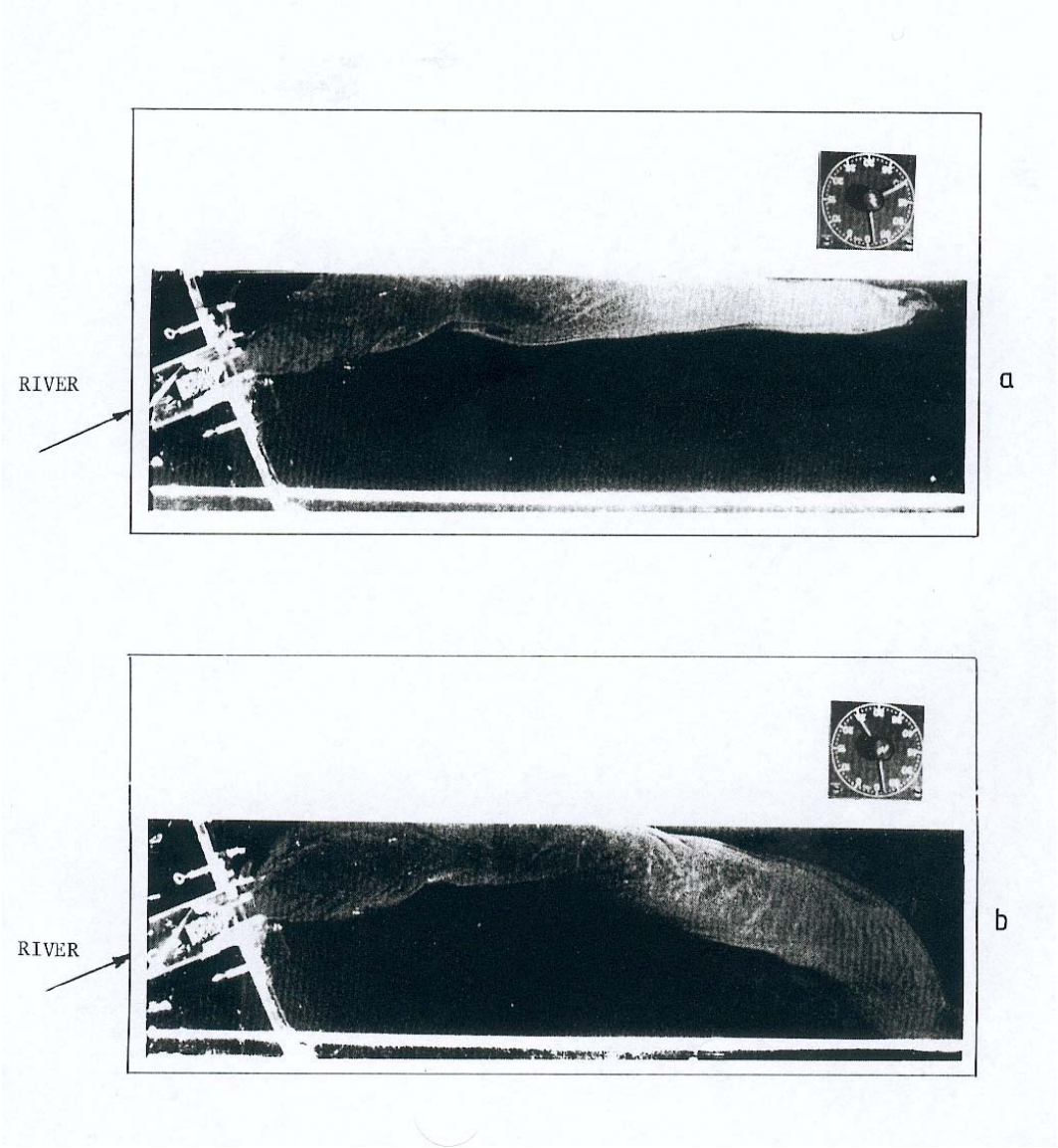

Figure 4.3 Photographs of the plumes simulated in the laboratory for **a)** without background rotation and **b)** with background rotation (McClimans, 1979).

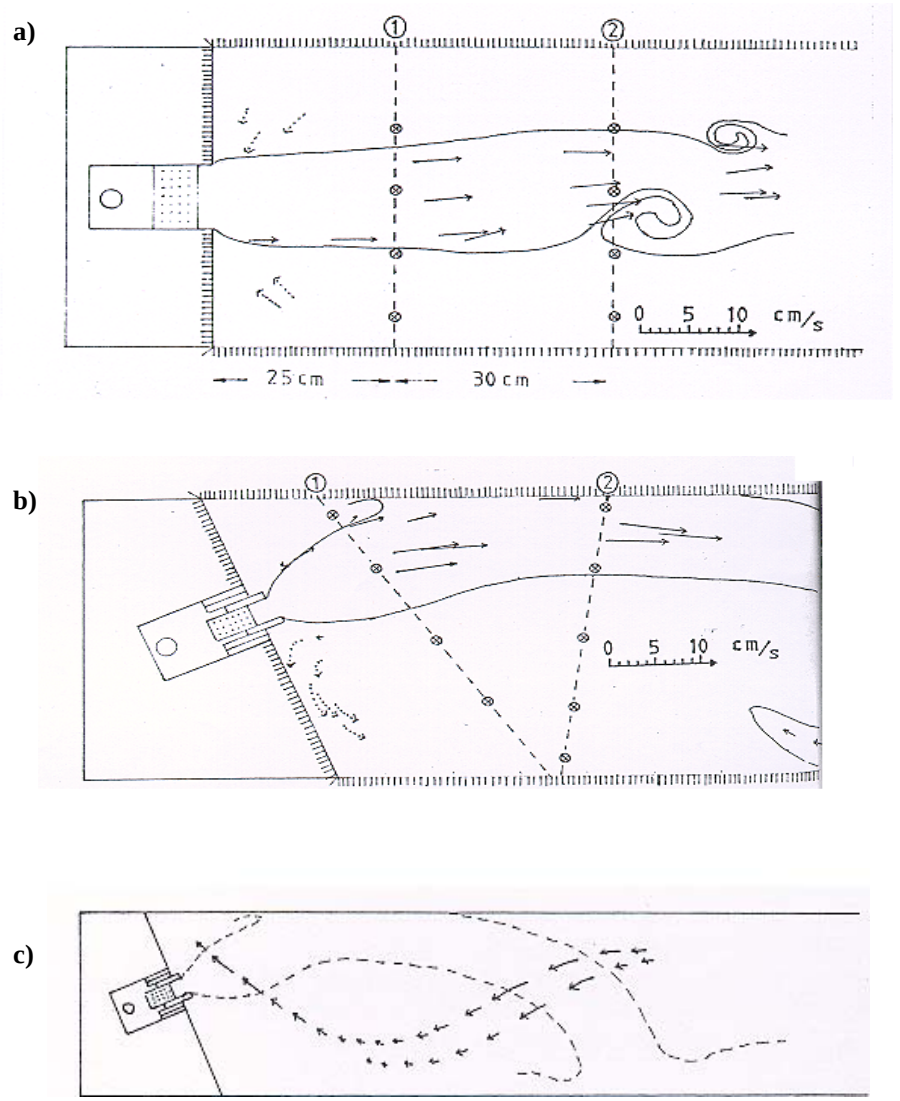

Figure 4.4 Results from laboratory simulations from Eidnes (1982). In **a)** the development of a river plume in a non- rotating basin, similar to Case 1. In **b)** rotation is included and **c)** shows the return current observed underneath the plume in **b)**.

4.3 The Rectangular Basin: Model configuration

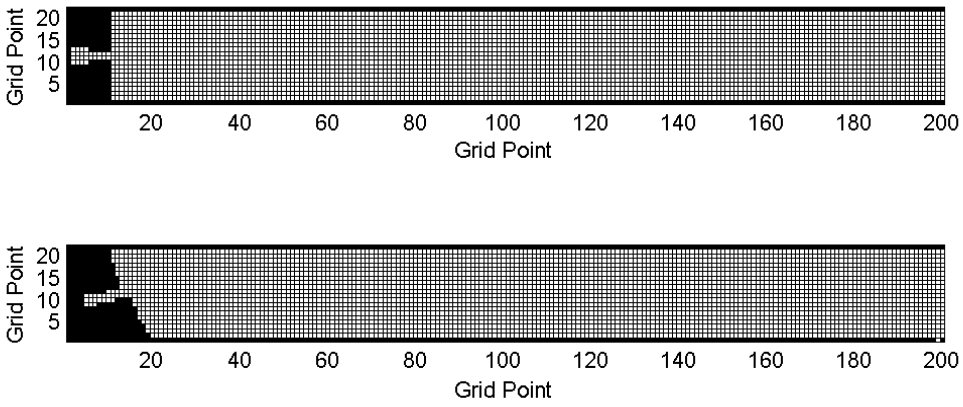

Figure 4.5 Test Basin I (upper) and II (lower) with 100 m horizontal grid spacing. The total length of the basin is 20 km and the width 2.2 km including land points.

The NCOM model is configured to model river discharges in an idealised basin as shown in Figure 4.5. The geometry of the basins is similar as to the one applied by Eidnes (1982) and McClimans (1980).

The depth of the basin is 200 m and the width is 2.2 km. The horizontal grid spacing is 100 m. Vertically, 14 σ levels and 26 z levels are employed. The total thickness of the σ layers is 6 m. The uppermost layer is 0.7 % of this, or approximately 4 cm thick. The thickness then increases linearly until reaching 25 %, or around 1.5 m. (The thickness of the z levels are 1.8, 2.1, 2.5, 2.9, 3.4, 3.9, 4.6, 5.4, 6.3, 7.4, 8.6, 10.1, 11.8, 13.8, 16.2, 18.9, 22.1, 25.9, 30.3, 35.4, 41.4, 48.4, 56.6, 66.2, 77.5, and 90.6 m).

Tests with twice as high resolutions both vertically and horizontally have been performed. Vertical and horizontal gradients were better resolved. Otherwise the results showed low sensitivity to an increase of resolution of this order.

The river discharges are implemented by defining flux and river water salinity. Further, a vertical profile of the discharge is defined. Model results were not found to be sensitive to how this was implemented and a linear profile over a depth of 1 m is applied. River channels with a depth of 3 m are

implemented both to steer the transport of the discharge in a desired direction and to make the river discharge into the basin more smoothly. The river sources are implemented at the head of the river channel as sources of momentum and buoyancy. The discharge rate and initial salinity distribution for the different cases are given in Table 4.1. A ramp function is applied in order to achieve a smooth start up of the simulations causing the river discharge to increase over a period of three hours before the constant rate as given in Table 4.1 is reached.

The distribution of a passive tracer is included in the simulations. The basin water has been given an initial vertical distribution with a weakly increasing concentration with depth. The discharged freshwater is given a slightly lower concentration than the surface water in the basin. This way the tracer is configured to visualise vertical displacements of the basin water.

Table 4.1 Input parameters for cases 1 to 10. April I: Initial vertical stratification interpolated from data from Station 15. April II: Same as April I but with a 0.5 m thick upper brackish layer with a salinity of S = 20. The vertical profiles of salinity from Station 15 in April are given in Figure 5.1

Case	***Q*(m^3m^{s-1})**	***Initial Stratific.***	***Coriolis***	**Test Basin**
1	100	S_0=10	-	I
2	25	S_0=10	-	I
3	100	S_0=20	-	I
4	100	April I	-	I
5	100	April II	-	I
6	100	S_0=20	x	I
7	25	S_0=10	-	II
8	25	S_0=10	x	II
9	100	April I	x	II
10	200	April I	x	II

4.4 Results

No rotation, no stratification: Cases 1 to 3

Cases 1 to 3 are run applying Test Basin I, with no background rotation, and with only a weak stratification initially defined. The stratification was introduced in order to avoid grid scale noise. When a completely homogeneous ambient was applied, grid scale noise was produced in the parts of the basin with no stabilising vertical stratification. The plots presented will be from Case 1. The changes in the initial set-up for cases 2 and 3 do not give any qualitatively different river plume development, except where it is explicitly mentioned.

The non-dimensional densimetric Froude number, F, is calculated by approximating the physics as a two-layer flow where the plume is a fresher upper layer propagating as an upper boundary current above a more dense layer. The depth, $z = -h(x, y)$, of the plume is defined to be the depth of the inflection point of vertical density distribution at each location. The reduced gravity, g', is calculated by choosing ρ_1 to be the mean density of the water above $z = -h(x, y)$ and ρ_2 the density of the water below. Further, I have chosen the characteristic velocity, U, to be the mean velocity above $z = -h(x, y)$. The densimetric Froude number is then calculated according to Equation (4.1).

Initial development

Figure 4.6 a) shows the horizontal surface distribution of salinity after 4 h for Case 1. There is an initial radial spread of the buoyant water transported into the basin and it forms a nearly semi-circular boundary toward the ambient water (Figure 4.6). In Figure 4.7 a) a vertical section of the salinity is displayed, also after 4 h simulation. It shows how the freshwater from the river mixes immediately with the more dense surroundings at the river mouth. The horizontal resolution of 100 m is coarse, especially in the river channel and the area close by. In combination with steep topography and high river outflow velocities, some noise is produced near the river channel inlet resulting in spurious values of salinity at a few grid points.

There is an outflow at all depths from the river channel, as seen in Figure 4.7 c), and no hydraulic control is therefore expected at the river mouth. In Case 2, however, the river discharge was reduced to $Q = 25\ \mathrm{m^3 s^{-1}}$. In this case a salt wedge is observed intruding partly into the river channel (not shown). The flow is thus regulated by a hydraulic control, as expected from theory (Stommel and Farmer, 1953). In Case 1 the flow is supercritical up to a distance from the river mouth with values up to F = 2-3, but becomes subcritical at each side of the basin, i.e. there is a large cross-basin gradient of F as seen in Figure 4.6 c).

The surface distribution of a passive tracer for Case 1 is displayed in Figure 4.6 b). Again, we can see the radial spreading of the plume. There is also a band of higher concentration of the passive tracer behind the leading front. The initial phase of the plume development, as shown in Figure 4.7, includes an overturning of the water column, visible in the vertical distribution of the passive tracer. Water with origin below the depth of the river channel, is lifted up and mixes with the plume water. The circulation in the rotor is completed by the sinking of water ahead of the front (Figure 4.7 b). When the leading front progresses further downstream, the distance between the overturning region and the leading front increases (Figure 4.8). Surface water is entrained from ahead of the plume into the front where it sinks and mixes along the frontal interface. A small part of this mixture is lifted toward the surface again right behind the front, which indicates the formation of a second overturning, extending over only a few grid points in the horizontal, i.e. over a few hundred meters. The major part of the water entrained and partly mixed along the frontal head moves, relative to the plume, in the other direction. This flow continues until it interacts with the vertical overturning described above. A more pronounced return flow is found towards the sides of the basin. Similar behaviour is also observed for cases 2 and 3.

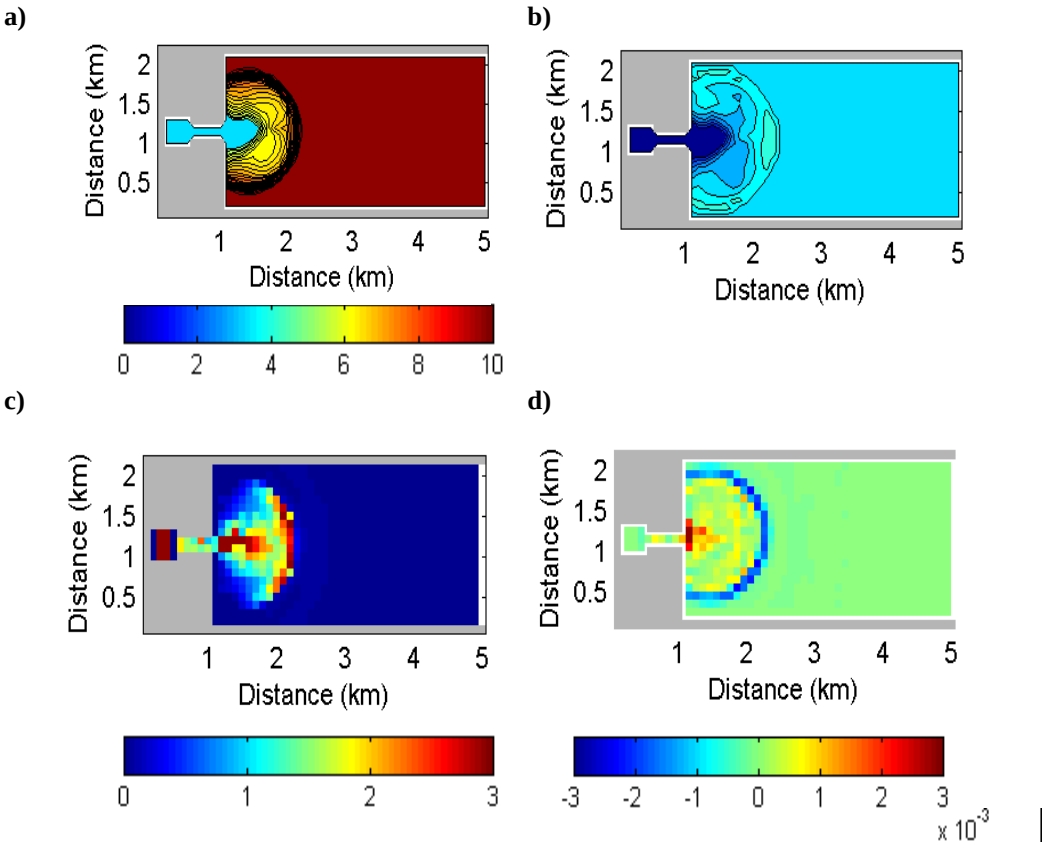

Figure 4.6 Results from Case 1 after 4 h simulation; **a)** surface salinity, **b)** horizontal surface distribution of a passive tracer, **c)** densimetric Froude number, and **d)** horizontal divergence of the surface layer.

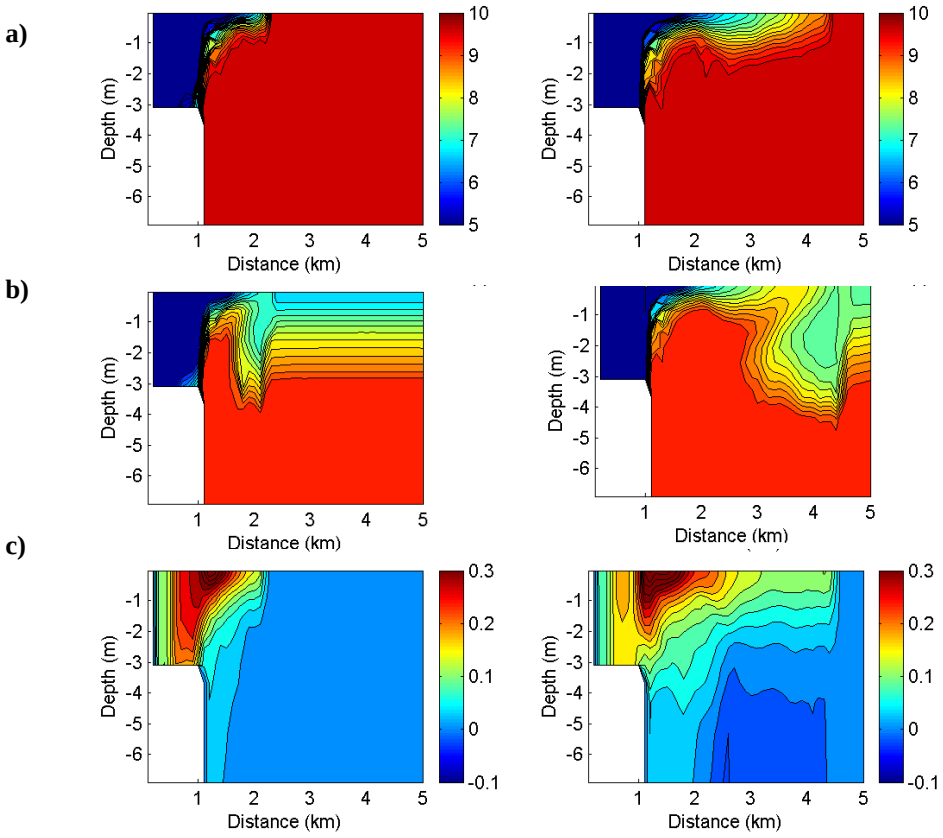

Figure 4.7 Vertical distributions along y = 1.1 km of **a)** salinity, **b)** passive tracer and **c)** u-velocity after 4 h simulation (left) and 12 h (right).

Transition from 3-D radial flow to 2-D parallel channel flow

The initial radial spread of the plume continues until the leading front hits the vertical walls at each side of the rectangular channel. This is shown for Case 1 in Figure 4.9. An immediate accumulation of fresh plume water is observed at the locations where the leading front collides with the walls. This results in the generation of internal bores that propagate away from the walls at approximately the same velocity as the leading front had before the collision. The convergence lines produced by these internal waves are seen in Figure 4.9 b). A similar situation where a bore was generated after the collision of a gravity current with a solid wall has been modelled in the laboratory and is described in Simpson (1997).

Buoyant water continues to accumulate at the outer edges of the front after the collision. The pressure gradient across this part of the front therefore gets larger than in the middle of the basin. There is thus an increase of the frontal propagation velocity near the walls. The process continues until the front approaches a straight line across the channel, spreading only in the *x*-direction.

After a few hours, the leading front observed for cases 1 to 3 propagates outward at a constant speed, c_f. This is displayed for Case 1 in Figure 4.10. In Case 3, where the initial salinity of the basin water was 20 instead of 10, the front propagates at a higher velocity than in Case 1 due to the greater density difference between the discharged river water and the environment.

The different flow regimes of a river plume

A 2-D channel flow with negligible lateral gradients in the across-basin direction develops behind the leading front, as described above. The flow maintains this character up to a distance behind the leading front. In the vicinity of the river inlet, the across-basin gradients of scalars and velocity, u in particular, are large, giving the flow a jet character. This jet intrudes further into the basin as time progresses and eddies develop at its edges, these leads to a subsequent meandering of the jet (Figure 4.11). The 2-D channel flow is subcritical while the jet is associated with supercritical flow conditions. A snapshot of this is shown in Figure 4.13. It appears that the

vertical overturning behaviour of the interface beneath the plume is the transition between the supercritical jet and the subcritical 2-D channel flow.

Return Flow

Figure 4.12 displays currents at four depths for Case 1 after 36 h simulation. The flows at the surface and at 0.6 m depth are quite similar. At 2 m depth a return flow at each side of the basin is set up to replace the ambient fluid mixed into the plume near the river outlet. Water is further entrained into the jet along the sides. A similar pattern at 3 m depth is shown. The divergence zone at this depth is related to the vertical overturning described above.

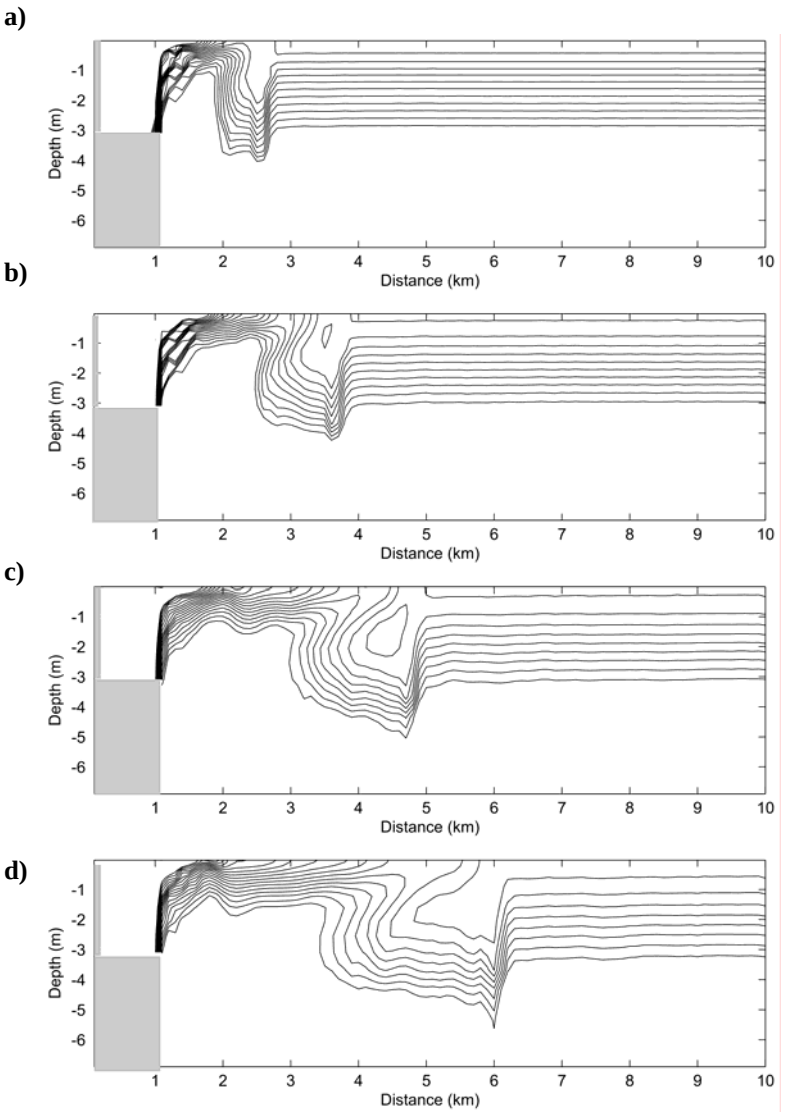

Figure 4.8 Vertical sections of passive tracer for Case 1 for a) t = 6 h, b) t = 10 h. c) t = 14 h and d) t = 18 h.

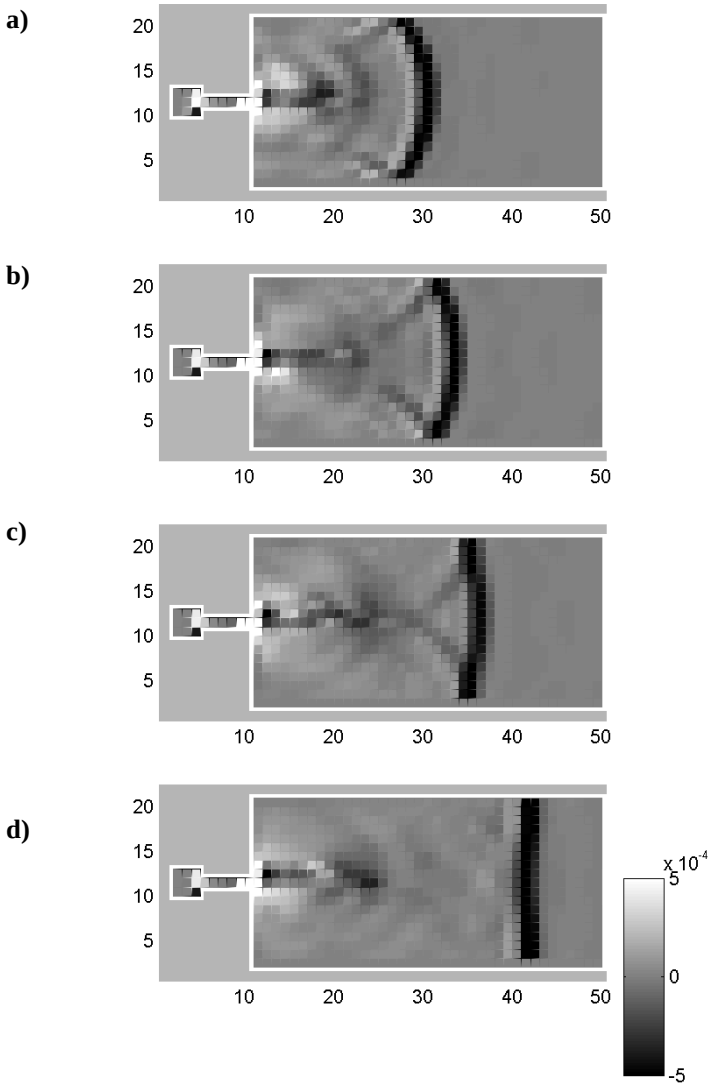

Figure 4.9 The surface flow at fronts is convergent. Lines of convergence and divergence are further associated with internal waves. The figure shows the horizontal divergence field at the surface at **a)** t = 3 h, **b)** t = 4 h **c)** t = 4 h 30 min and **d)** t = 7 h 10 min. Negative values indicate convergence.

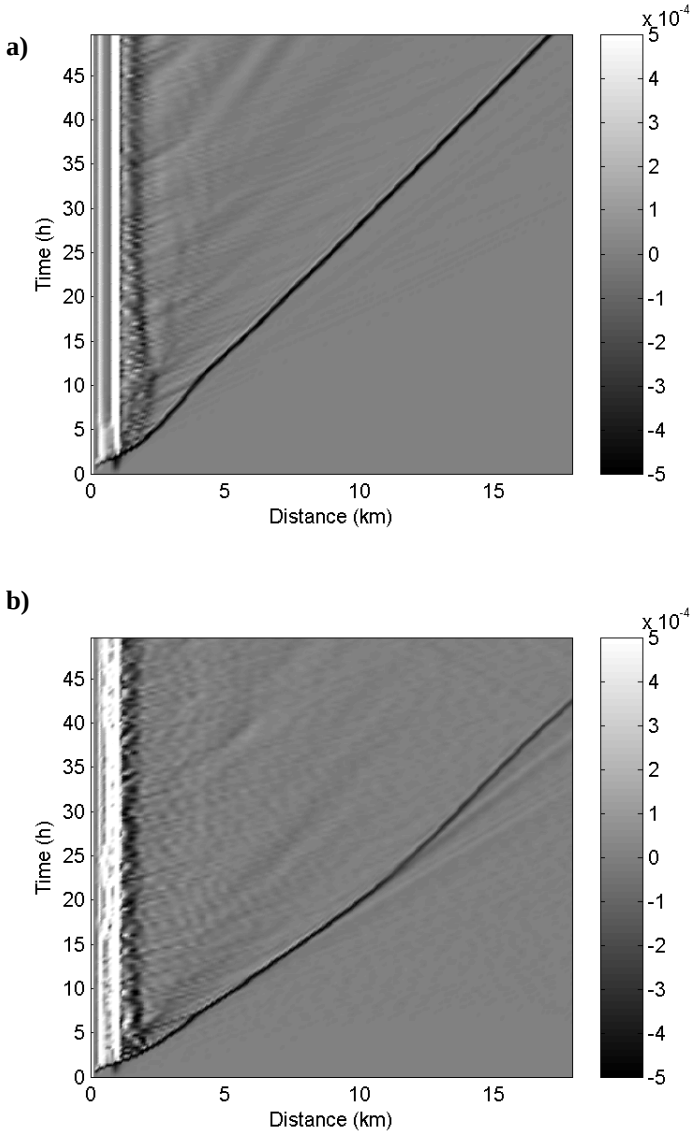

Figure 4.10 The horizontal divergence in the surface and along y = 1.2 km is plotted against distance in the along-basin direction along the x-axis, and time along the y-axis. The front is here identified as a narrow band of negative values of horizontal divergence. The results are from **a)** Case 1 and **b)** Case 4.

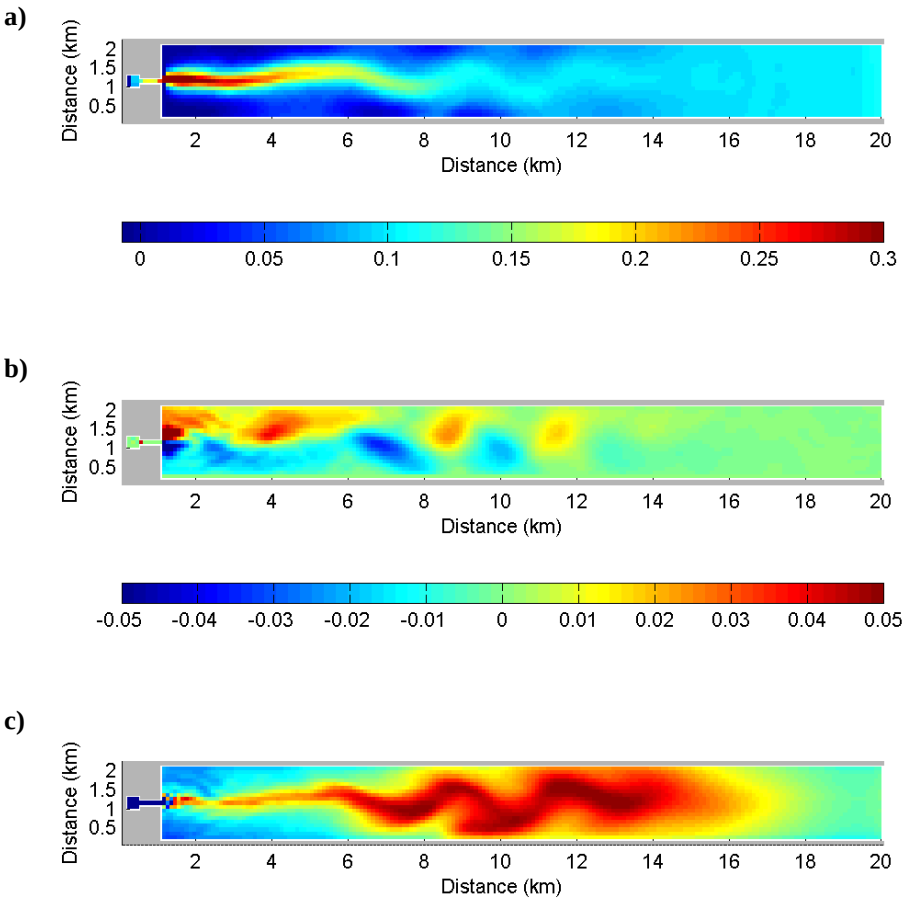

Figure 4.11 Results from Case 1 showing eddies forming at both sides of the jet. The *u*-velocity is displayed in **a)** and *v*-velocity in **b)** for the surface layer. The horizontal distribution of a passive tracer at 1m depth is given in **c)**.

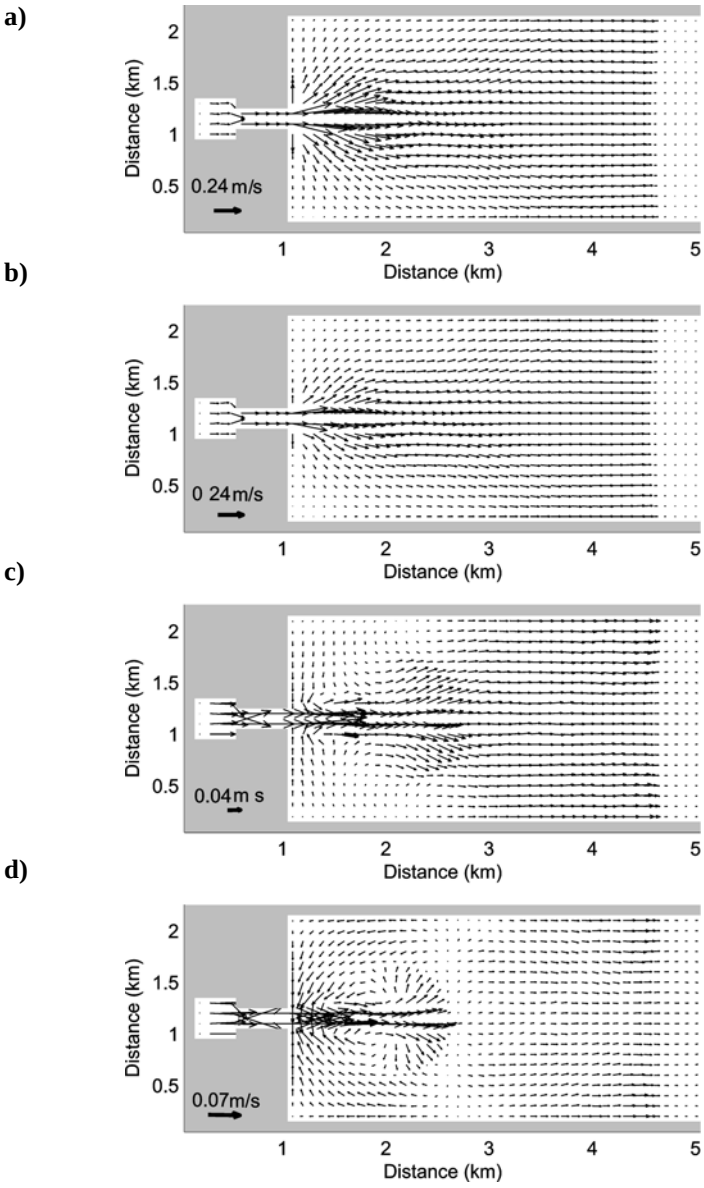

Figure 4.12 Currents for Case 1at t = 12 h, **a)** at the surface, **b)** at 0.6 m depth, **c)** at 2 m depth, and **d)** 3 m depth.

Ambient stratification: Case 4 and Case 5

The initial stratification applied in cases 4 and 5 is obtained from salinity data for April 2002 from Station 15 in the Trondheim Fjord. This is the same stratification that will be used in the following studies in Chapter 5. Figure 4.14 displays the evolution of the river plume in Case 4, similar to what is done for Case 1 in Figure 4.8. The plume in Case 4 travels at a higher velocity compared to that in Case 1, which is expected, considering the larger density difference between the fresh river water and the ambient in the former case (Figure 4.10). The river plume development during the first 13 h is similar to Case 1, but there are some important differences. Internal waves are generated in Case 4 that envelope the head of the river plume (Figure 4.14 a) and b)). After approximately 13 h the waves separate from the plume and propagate downstream (Figure 4.14 c) and d)). The sudden change of the propagation speed of the leading front, and the internal waves propagating away from it, is seen in the horizontal divergence field presented for Case 4 in Figure 4.10 b). The head of the plume is disrupted, but a new one soon forms and the process is repeated. Energy is extracted from the river plume into the internal waves and in time the frontal region starts loosing identity; the cross-frontal gradients are reduced and the convergence rate decreases.

Case 5 is configured like Case 4, except that a 0.5 m thick surface layer with S = 20 is introduced. The increased vertical stratification in Case 5 implies higher vertical stability and lower densimetric Froude numbers. The development of the plume in Case 5 is displayed in Figure 4.15, and may be compared to similar plots from Case 1 and Case 4 in Figure 4.8 and Figure 4.14, respectively. There is not a distinct frontal boundary associated with large gradients observed to form for Case 5. Internal waves are nearly from the start of the simulation observed to generate and propagate downstream away from the plume.

Snapshots of the local densimetric Froude number distributions for cases 4 and 5 are displayed in Figure 4.13 b) and c). In Case 4 the conditions at the leading front are near critical with $F \approx 1$ after 14 h, but become subcritical as time passes. Characteristic for all cases is the development of a supercritical jet and a subcritical 2-D channel flow. The transition between the two is associated with a vertical overturning, as has been described for Case 1.

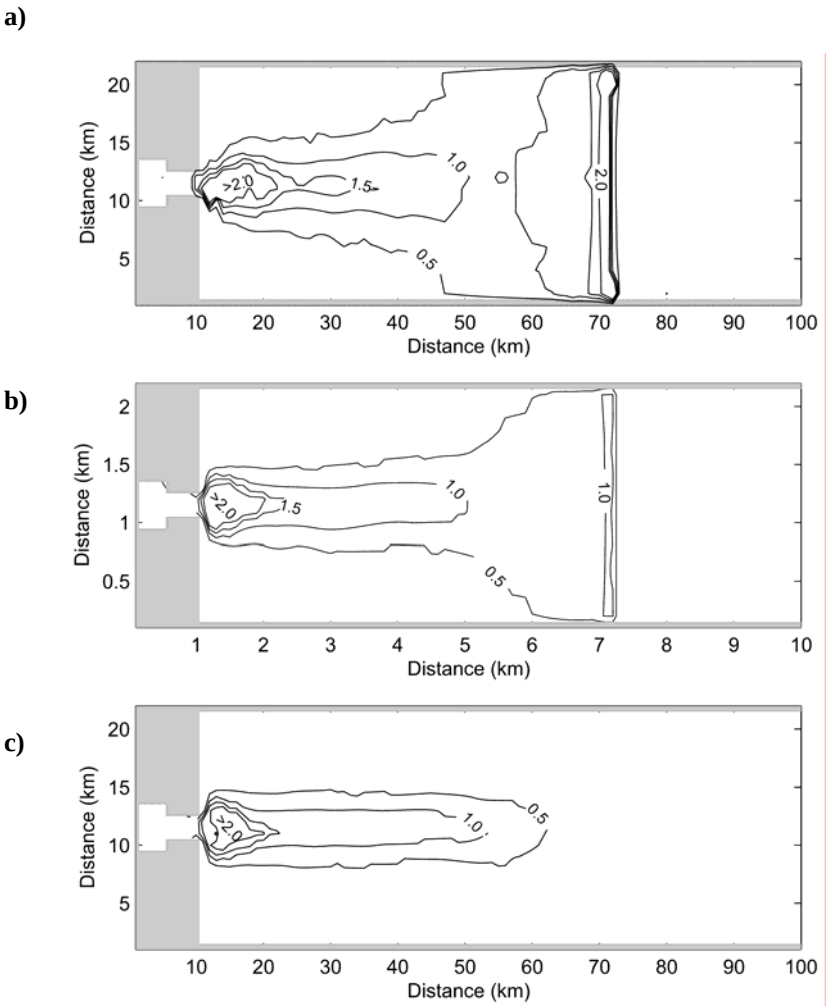

Figure 4.13 Local densimetric Froude number distributions: **a)** Case 1 after 21 h 20 min **b)** Case 4 after 14 h and **c)** Case 5 after 14 h.

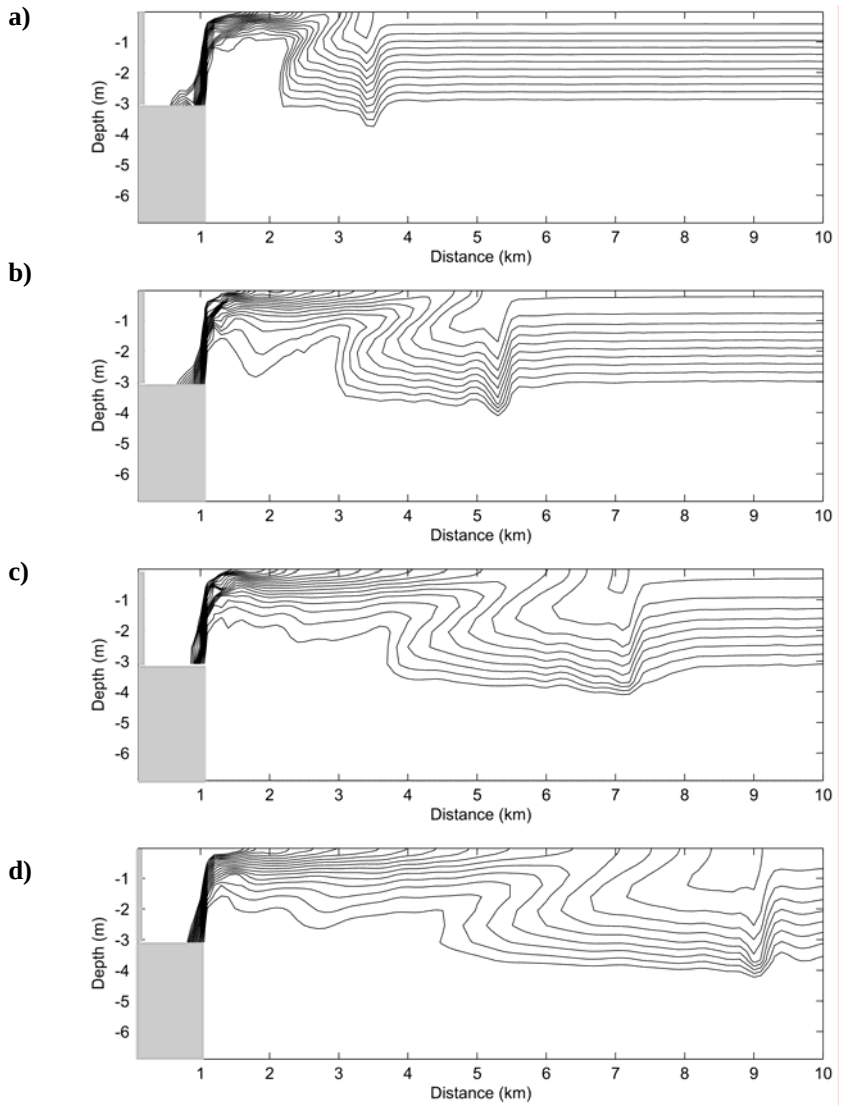

Figure 4.14 Vertical sections of a passive tracer for Case 4 along y = 1.2 km for **a)** t = 6 h, **b)** t =10 h, **c)** t =14 h, and **d)** t =18 h.

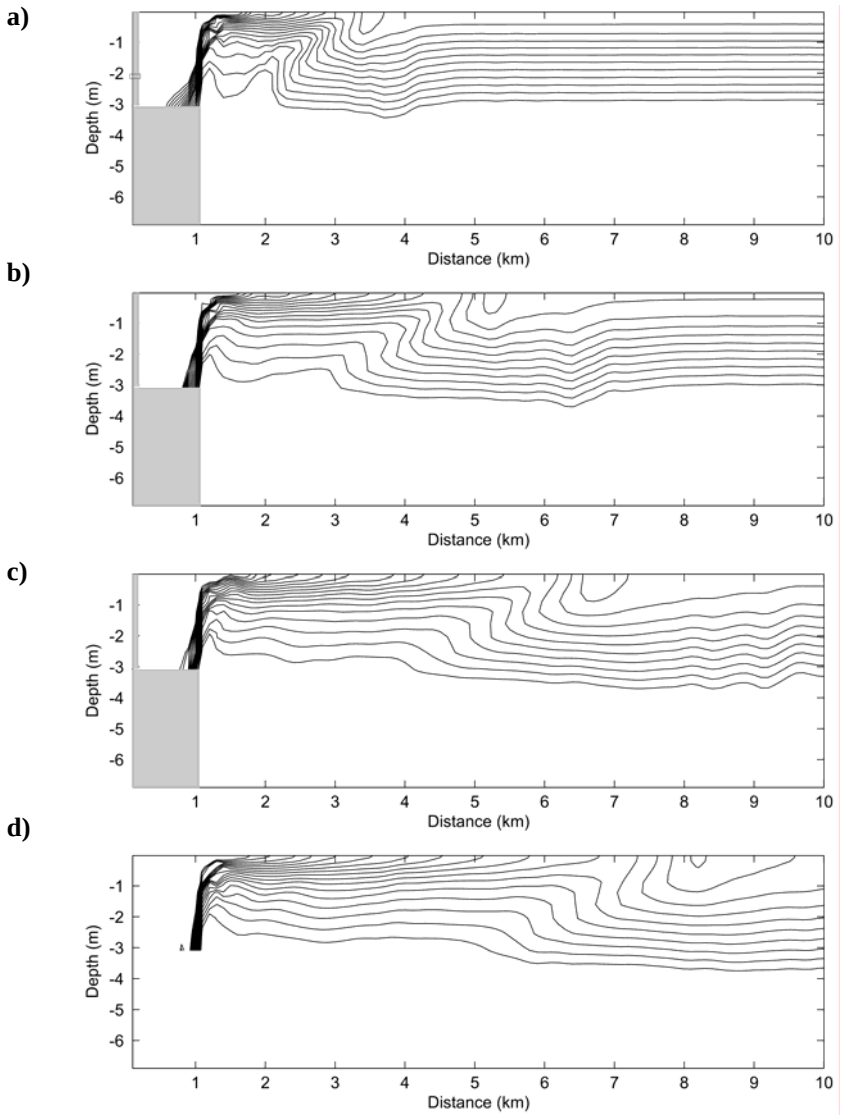

Figure 4.15 Vertical sections of a passive tracer for Case 5 along y= 1.2 km at **a)** t=6 h**, b**) t=10 h, **c)** t=14 h, and **d)** t=18 h.

Figure 4.16 displays results from cases 7 and 8. The currents in Figure 4.16 a) and b) are from the surface and at 1.6 m depth, respectively, after 36 h simulation. The two cases are equally configured, except that background rotation is included in the computations in Case 8.

In the case of no rotation the jet is observed to follow the left hand shore. In time, the pressure gradients across the basin cause the flow to deflect slightly towards the right. Initially, a radial spread of the discharged buoyant water is observed also for Case 8, as in the non-rotational cases. As time progresses the leading front collides first with the left hand shore, generating an internal bore traveling in the opposite direction. The current jet formed by the river discharge deflects to the right and hits the wall at the other side where a coastal-trapped current starts to form. The frontal part of this is observed to propagate at a higher velocity than the leading front in Figure 4.16 a). The background rotation causes the plume to be thicker at the right hand shore, thicker than the plume in the non-rotational case where the plume is evenly distributed in the lateral direction behind the leading front. A thicker plume gives a higher hydrostatic pressure gradient in the along-basin direction causing the plume to propagate at a higher velocity. The difference is demonstrated in Figure 4.17 showing vertical sections of the salinity distribution in the two cases.

Along the right hand wall, there is a stagnation point in the flow field (Figure 4.16 c)). When the jet hits the wall, the main part of the forms a coastal-trapped current propagating along the right hand sidewall of the basin. A small part of the flow is directed in the other direction. A backwater of anticyclonic circulation forms. A simulation with background rotation has also been performed with Test Basin I (Case 6). The overturning of the jet is in this case not observed to be as violent as in Case 8, due to the different discharge directions in Test Basin I and Test Basin II.

Case 9 is initially stratified and the discharge rate is 200 $m^3 s^{-1}$. The currents at four depths are displayed in Figure 4.18 for Case 9. At the surface and at 0.6 m depth, the strong and deflected jet dominates the flow at this time. In the backwater of the jet there is an anticyclonic circulation as described for Case 8. At 1.6 m depth, just beneath the plume, an anti-cyclone

dominates the flow. At greater depths the flow is toward the head of the basin. The currents at 3 m depth are shown in Figure 4.18. This return flow is stronger on the left hand side of the basin except in the vicinity of the river outlet. The return flow is here observed to turn and cross beneath the jet to the other side and continues thereafter toward the head of the basin. This is a similar pattern to the one described by Eidnes (1982) (Figure 4.4). An anticyclonic circulation that does not seem to be correlated with the one at shallower depths is seen near the head of the basin.

To find a representative inertial radius, $U = 0.1\ \mathrm{m\ s^{-1}}$ is chosen as a characteristic value. This gives an inertial radius of approximately 0.8 km for Case 8. This is close to the radius of the anticyclonic circulation in the backwater of the jet. As the discharge rate is increased, the jet intensifies accordingly, resulting in a larger inertial radius. For the results presented in Figure 4.18 $U = 0.4\ \mathrm{m\ s^{-1}}$ giving $r_i \simeq 3\ \mathrm{km}$. The baroclinic Rossby radius is calculated using the same procedure to that described for calculating the densimetric Froude number. For Case 8 after 40 h the radius ranges from 0.8 km to 1.2 km, depending on location. The thickness of the river plume decreases downstream, and it gets denser due to mixing. Consistently, the width of the coastally trapped current decreases downstream.

The frontal boundary is deformed as the plume adjusts to the effect of background rotation. It is still observed to be supercritical with F = 1 to 2 for all cases run with background rotation, i.e. the baroclinic Rossby deformation radius and the inertia radius are approximately of the same scale. The horizontal distribution of the densimetric Froude number is shown in Figure 19 a) for Case 8, at the same time as presented in Figure 4.16. The Froude number is found to be greatest at the head of the coastally trapped density driven current. A vertical overturning as described for the non-rotational cases is also observed as the flow goes from a supercritical state of the overturning jet to the subcritical current behind the supercritical frontal region,(Figure 4.19 c) and d)).

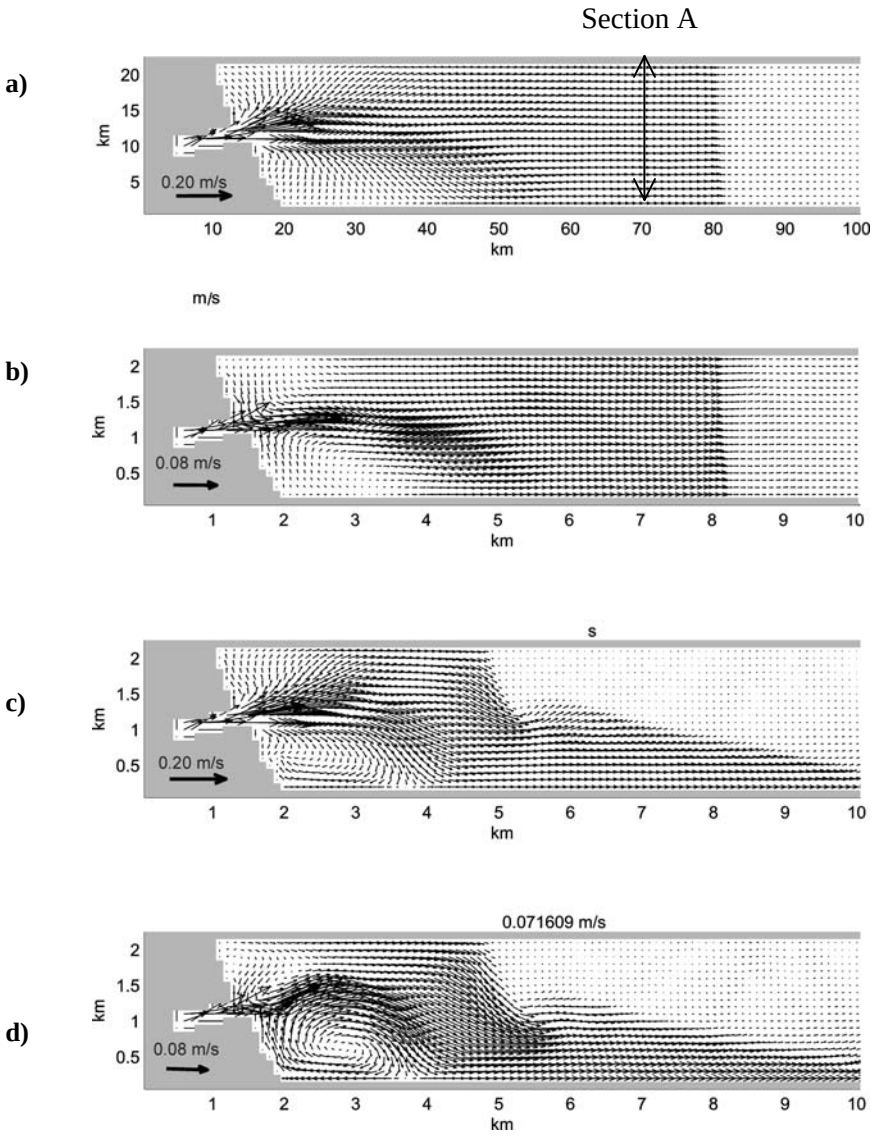

Figure 4.16 Currents presented for Case 7 at **a)** 0.02 m and **b)** 0.7m depth after 40 h simulation, and for Case 8 at **c)** 0.02 m, and **d)** 0.7 m depth.

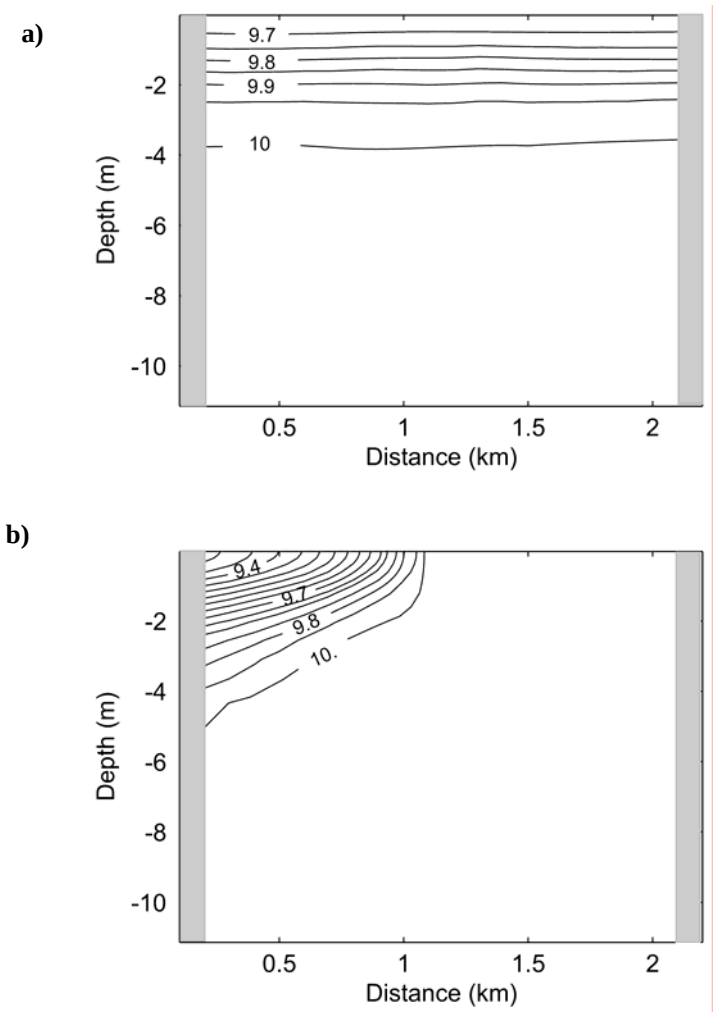

Figure 4.17 Vertical distribution of salinity after 40 h simulation along section A shown in Figure 4.16 for **a)** Case 7 and **b)** Case 8.

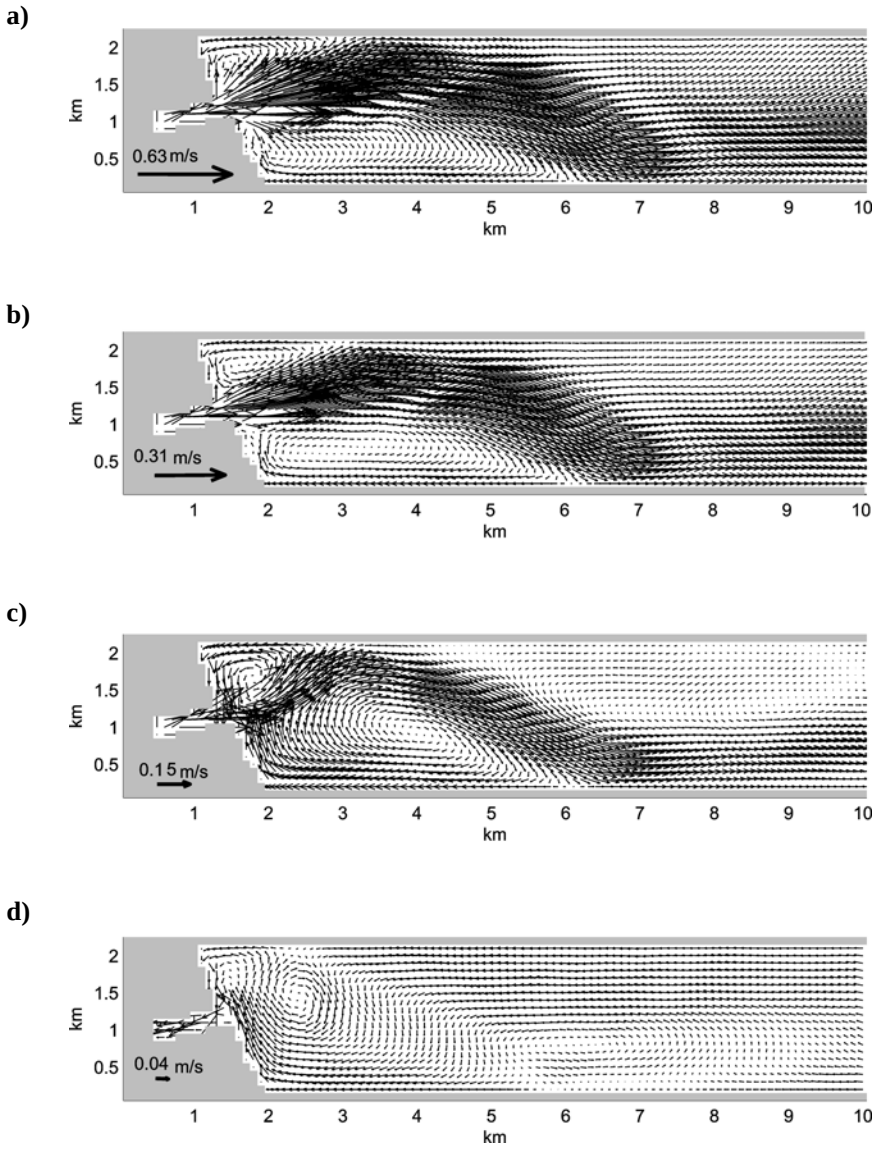

Figure 4.18 Currents for Case 9 at **a)** 0.02 m, **b)** 0.6 m **c)** 1.6 m and **d)** 3 m depth after 60 h simulation.

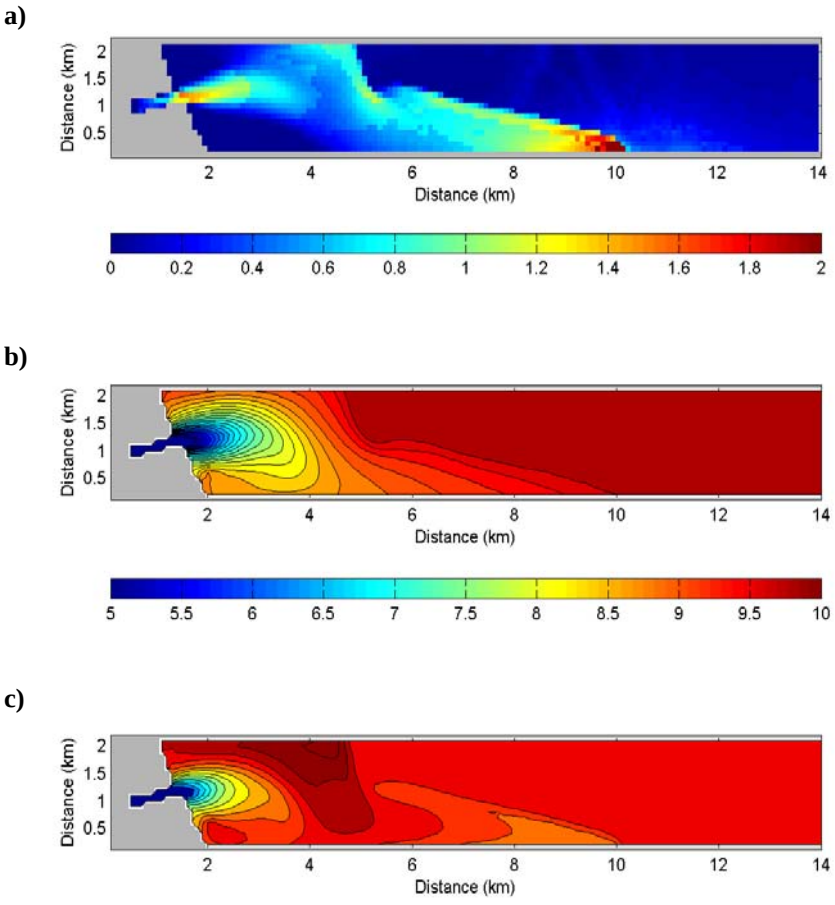

Figure 4.19 The distribution of **a)** densimetric Froude number, **b)** surface salinity and **c)** passive tracer at the surface.

4.5 Discussion

No rotation

The simulation results showed that two distinct flow regimes developed: a supercritical jet and a downstream subcritical flow with small gradients in the cross-basin direction. The transition from the jet-dominated part of the plume to the subcritical flow farther downstream was through an internal hydraulic jump characterised by a vertical overturning. The thickness of the plume was found to be greater farther downstream than in the jet dominated part upstream. The overturning is very interesting regarding mixing of plume water with the ambient. Water transported into the area by the jet mix with saltier water both from below and with a mixture of plume water and the ambient that form a return (compesation) flow beneath the plume. Water ahead of the leading front was observed to be drawn into and mix along the convergent front. This mixture is slower than the plume above and forms as such a return flow relative to the leading front. This is similar to the secondary circulation described by McClimans (1978; 1988; 1994) among others. A vortex forming beneath the plume similar to the one described for the numerical simulations is described in McClimans (1988) (Figure 4.2).

As the freshwater leaves the river channel it is mixed with saltier water from below. To replace this fluid, a return flow on each side of the jet, where the flow is subcritical, was found to maintain continuity. Along the jet, horizontal shear eddies develop on each flank. In time, these cause the jet to meander. This behavior was also observed by Eidnes (1982) and McClimans (1980) in their similar simulations of river plumes in a laboratory model (Figure 4.3 and Figure 4.4)

Internal waves were generated when freshwater was discharged into a stratified ambient. In Case 4 these waves were observed to envelope the head part of the plume the first 12-13 h. The velocity of the front during this period was constant. After this the wave separated from the plume and propagated away downstream. The waves extracted energy from the plume and subsequently caused it to slow down. This behavior is similar to that observed by Maxworthy et al. (2002) for supercritical gravity currents. In Case 5, a distinct supercritical frontal boundary was not observed. Internal

waves were observed to continuously radiate away from the plume. This behavior is though different from the subcritical situation described by Maxworthy et al. (2002), where the velocity of the nose of the current oscillated. They describe a detailed interaction processes between the head of the current and internal waves. The head part of the river plume, however, is not well resolved in the simulations presented here.

The internal wave and river plume interaction seems to be similar in cases 4 and 5. In the latter case, the increased stratification induced higher internal wave speeds. The interaction between the head of the plume and the internal waves can therefore be expected to happen earlier than in Case 4, probably within the period when the river discharges were ramped. This may explain why a supercritical front never was observed in Case 5.

When the conditions at the leading front became subcritical in Case 5, the front started to loose identity. This is a typical detrainment example, i.e. the fresher water of the plume is entrained into the surrounding fluid. This is partly consistent with the considerations of McClimans (1994). He associated supercritical or critical fronts to be associated with entrainment, and detrainment for fronts that were subcritical in the far field.

The influence of the rotation of the earth

Results from Eidnes (1982) and McClimans (1980) are shown in figures 4.3 and 4.4. The similar simulations presented here show some of the same dynamical behavior as described for the results from the laboratory experiments. A jet is observed to develop within the plume. In the case of no rotation, the jet in the laboratory was observed to stick to the left hand shore. Simulations showed similar tendencies. At a distance away from the river inlet, however, the flow turned toward the middle of the basin. In time, the flow adjusted to a 2-D channel flow like the cases with Test Basin I without rotation.

The effect of background rotation is conspicuous and affects both the development and characteristics of the river plume. The jet was observed to turn according to the inertial radius. An anticyclonic circulation was observed in the backwater of the jet. As the frontal part of the plume hit the wall on the right hand side, internal bores were generated. The flow continued as a

coastal trapped density driven current. The width of the current seems to scale with the baroclinic Rossby radius, also found by McClimans (1980). Quantitative properties are difficult to compare between the different types of modeling. There is a general tendency, though, that the entrainment was low in the laboratory, lower than indicated by field measurements (Eidnes, 1982). The simulation results do show generally high values of salinity. This may be partly due to the salinity of the discharged water which is $S = 5$ in the simulations, while the discharged water in the laboratory models was nearly zero. Negative values might be produced if a lower salinity value were applied in the numerical simulations. If the mixing is generally lower in the results by Eidnes (1982) and McClimans (1980), this will consequently give larger velocities and a correspondingly larger inertial radius. Qualitatively, though, the model reproduces a similar plume development as observed using the laboratory models. The return flow shown in Figure 4.4 c) and the simulation results also compare well.

James (2002) showed by numerical simulations that an anticyclonic circulation developed in a rectangular basin that was forced by a freshwater discharge, even in low mixing cases. The results implied that, in a semi-enclosed basin with a buoyant discharge at the head, the resulting plume has the same dynamical properties as in river discharges associated with a high Kelvin number. The anticyclonic circulation is in this way the equivalent of the bulge region. Simulations presented here show similar patterns as shown by James (2002), even though the scale is much smaller.

The simulations show anticylonic circulation patterns beneath the plume. The circulations are found in connection with the strong divergence field beneath the jet part of the plume. The divergence of heavier fluid upwards to a level of lighter fluid may result in this circulation following the arguments by Fujiwara et al. (1997).

4.6 Summary and conclusions

The motivation for the simulations presented here were two-fold. First, to evaluate the model's ability to simulate river plumes in a rotating basin and secondly, to provide insight on the development of river plumes in a fjord environment. An agreement is found between the results from laboratory modelling of river plumes and the numerical simulations presented in the present chapter. This has shown that the model reproduces the behaviour and characteristics of river plumes fairly well. However, the results can be improved quantitatively.

The simulations have shown that the mixing between river plume water with the surrounding water may occur in several regions. The river water mixed with surrounding water already in the river channel or immediately after discharging into the basin, depending on the discharge conditions. Water from the surface ahead of the plume was entrained into the leading front and sank along it. A small part of this water was brought to the surface again right behind the front. The main part formed a secondary flow beneath the plume. This flow continued until reaching the region where an internal hydraulic jump, that separated the supercritical jet part of the plume and the 2-D channel flow farther downstream, further mixed this water with the more dense water from below.

The behaviour of the plume became significantly changed when background rotation was included in the simulations. The river plume diverted to the right and got trapped to the right hand side of the basin. Near the river inlet the flow developed a jet character. An internal hydraulic jump, as observed in the non-rotational cases, separated this jet part of the plume with the subcritical part farther downstream. When reaching the right hand side of the basin, a part of the plume water was observed to flow in the other direction, i. e. toward the head of the basin, and an anticyclonic circulation was formed to the right of the river mouth.

When stratification was introduced, internal bores and internal waves were generated. If the frontal part of the plume were subcritical, internal waves beneath the main plume body propagated away from the plume and transported energy away from the plume. A web camera was placed at Byneset in September and October 2002 and took pictures every third

minute. The frames showed a high variability of the freshwater fronts in this part of the fjord. During this period, bands of slicks typical for high frequency internal waves were commonly observed. I believe they are related to freshwater fronts. A snapshot of this situation is shown in the front page of this chapter.

Chapter 5

Effect of internal tides and rotation of the earth at the spread of freshwater from rivers in the Trondheim Fjord

A freshwater front in the Cross Fjord. Gaulosen is to the right in the photo.

Abstract

The Navy Coastal Ocean Model (NCOM) is used to simulate the Seaward Basin, the largest and widest basin in the Trondheim Fjord. The discharge from four rivers located in this part of the fjord is included in the simulations. The results show that processes related to the rotation of the earth, interaction between different river plumes, and the internal tides are important for the spread of freshwater from rivers.

Keywords: river plumes, anti-cyclonic circulation, frontal occlusion, spiral eddies, internal tide, internal wave resonance.

URN:NBN:no-3496

5.1 Introduction

The NCOM has been run applying a realistic bathymetry for the Trondheim Fjord and discharges at a constant rate from the rivers Orkla, Gaula, Nidelva and Stjørdalselva, all located along the southern coast of the Seaward Basin. The simulations have been run for a few days using an initially defined stratification. The effect of rotation on river plumes in the Trondheim Fjord was seen in the previous chapter. I now continue simulating discharges into a more realistic environment. Tides are introduced to investigate the effect of tidal forcing on the freshwater spread.

The effect of the earth's rotation on river plumes

The rivers Orkla, Gaula and Nidevla discharge into three somewhat different environments with regard to local topography. The hydrographic conditions of the ambient, however, are the same. It is thus interesting to study how the developments of the plumes in each case are affected by the rotation of the earth. Gaula and Orkla discharge freshwater into two fjord arms of the Seaward Basin that are similar to the Gulf type ROFI (Region Of Freshwater Influence) studied by Fujiwara et al. (1997) and James (1997). The river Nidelva, on the other hand, enters the fjord along the southern side of the Seaward Basin and is less restricted by topography. Even though of a different scale, the situation is similar to the classical studies of river discharges from a source along a coast and into an open ocean; see for instance Fong (1998) and references therein. The Stjørdal River plume is not studied in detail.

Colliding river plumes

Since there are four plumes developing within the Seaward Basin, they will collide and interact. The part of the basin that is in this sense the most interesting is the Cross Fjord through which both the Orkla River plume (ORP) and the Gaula River Plume (GRP) propagate on their way to the wider part of the Seaward Basin. As the plumes collide, surface water piles up between the plumes and may lead to the generation of internal bores travelling away from the collision site in both directions. The behavior is

similar to a river plume colliding with a vertical wall, as discussed in the previous chapter. The phenomenon is described by Simpson (1997) for the collision of gravity currents in the laboratory. He found that, after the collision, the plume of higher density submerged beneath the other, consistent with the results from the simulations with NCOM.

Spiral eddies

Spiral eddies have been long known to be typical surface features of the world's oceans seen in the sun glitter from space. They are documented in a large number of images taken from space shuttles, some of which are included in Munk et al. (2000). They give a detailed history of the discovery of sea spirals and address questions of how the eddies develop, why they are dominantly cyclonic and what makes them visible. Assuming a frontal preconditioning stage producing cyclonic vorticity, they suggest that the spirals are wound up by the Kelvin's "cat's eye" circulation associated with horizontal shear instability. Eldevik and Dysthe (2002) and Shen and Evans (2002) show how spiral eddies may be generate in the ocean applying numerical simulations. Eldevik and Dysthe (2002) suggest that an ageostrophic baroclinic instability mechanism causes the spirals to form. Sea spirals are in this sense the ocean analogue to cyclonic frontal systems in meteorology. Shen and Evans (2002) show that density stratification is not required for spiral eddies to form. In their case, the inertial instability of anticyclonic shear leads to the enhancement of cyclonic shear, which in turn produces a cyclonic spiral eddy by (barotropic) shear instabilities.

The high resolution of the simulations of the Trondheim Fjord produce cyclonic eddies that spin up frontal interfaces into spirals. Eldevik and Dysthe (2002) show that large horizontal density gradients have strong cyclonic vorticity. The fronts that form from freshwater discharges in the Trondheim Fjord have the same property. Fronts and spiral eddies are thus ubiquitous features of both the horizontal divergence field and the vorticity field. The structure of the spirals is similar to the ones shown in Munk et al. (2002). The initial phase of the simulated spiral eddies is found to be associated with frontal occlusion processes, either when two plumes collide or when the frontal interface of the plume interacts with itself. In these

processes, cyclonic eddies are generated and result in local pools of cyclonic vorticity. A couple of days later, these eddies are observed to grow further and develop a spiral structure as a horizontal shear develops across the frontal boundary. This implies that the spiral eddies simulated in the Trondheim Fjord are generated from both baroclinic and barotropic instability mechanisms.

Internal tides

The Trondheim Fjord has depths mostly larger than 200 m (see Figure 5.2). The tidal currents are accordingly weak. The exceptions are across horizontal and vertical contractions, such as the Agdenes, Tautra and Skarnsund silll, through which the tidal flow accelerates. Interaction between these topographical features, stratification and tides may give rise to internal tides, high frequency internal waves, and internal hydraulic jumps. Energy is in this way extracted from the tidal currents. The internal tide may be important for deep water mixing in fjords (Stigebrandt, 1976; Stigebrandt and Aure, 1989). The internal waves may also cause enhanced exchange of water between two basins separated by a sill as heavy water may be lifted above sill level. This is studied by Vlasenko et al. (2002). They have applied a nonhydrostatic 2-D numerical model to perform high-resolution simulations of an idealised case configured to represent the Skarnsund sill.

The NCOM model reproduces internal waves of tidal frequency seen to propagate around the Seaward Basin in the direction of Kelvin waves. Non-linear waves of higher frequencies are also generated, but these are not considered to be well simulated by the NCOM model that is based on the hydrostatic approximation.

Resonance of internal waves

The Trondheim Fjord includes several fjord arms and bays. In specific cases the length of these can be such that there may be a resonance of the internal tidal wave. First, consider an idealized basin of length L that is being exposed to a periodic forcing of period *T*. For simplicity, consider a configuration of a two-layer model where the upper layer has the thickness h and density ρ_1, and let the lower layer be infinitely deep with density ρ_2.

For this case the speed of the interfacial wave is $c_i = \sqrt{g'h}$ where $g' = g(\rho_2 - \rho_1)/\rho_2$ is the reduced gravity. In the case of a basin closed at both ends, resonance may occur if the period of the natural oscillation of the basins equals a whole numbers of periods of the external forcing (Pond and Pickard, 1995):

(5.1) $$T = \frac{2L}{nc},\ n = 1, 2, 3..$$

In the case where one end of the basin is open, the system may behave as half of the basin considered above. The condition for resonance then requires that the length of the open basin to be ¼ of the wavelength of the external wave. The fundamental natural oscillation of the basin is then given by

(5.2) $$T_f = \frac{4L}{c}\ ,$$

where L is now the length of the open fjord arm. Resonance of an internal tide may occur in the Orkdal Fjord, depending on stratification conditions. The length of the Orkdal Fjord is $L_o \approx 7$ km, and the frequency of the internal tide is by definition approximately 12.42 h (same as the semi-diurnal tide). Resonance occurs if $c_i \approx 0.62$ m s^{-1}, according to Equation (5.2). This phenomenon is quite interesting when studying the spreading of freshwater from the Orkdal Fjord. Simulations presented below imply that resonance of the internal tide in the Orkdal Fjord may significantly influence the outflow of buoyant water from the fjord arm.

5.2 Model configuration

The NCOM (Navy Coastal Ocean Model) is configured for the Trondheim Fjord to simulate scenarios both with and without rotation, and with rotation including the forcing by semi-diurnal tides. The bathymetry applied in the simulations is shown in Figure 5.2. To save computational time and cost, only the central part of the Trondheim Fjord is included for cases without tidal forcing. There are a total of four rivers implemented: Orkla, Gaula, Nidelva and Stjørdalselva. To control both the direction of the buoyant outflow and the momentum flux from the rivers, river channels are implemented. The salinity of the discharged river water is $S_{riv} = 5$.

The horizontal grid spacing is 100 m in all cases. Vertically, 15 σ levels and 25 z levels are employed. The same levels are applied as described in Chapter 4.

The tides in the Trondheim Fjord are semi-diurnal. For simplicity M_2 is the only tidal component implemented for the runs with tidal forcing in addition to the river discharges (Table 5.1). The model is further configured with an initial stratification that is interpolated from data from Station 15 in the Trondheim Fjord (Figure 5.3). Data from both 12 March 2002 and 15 April 2002 are applied and are displayed in Figure 5.1. The configuration of the model is otherwise similar as in chapters 3 and 4.

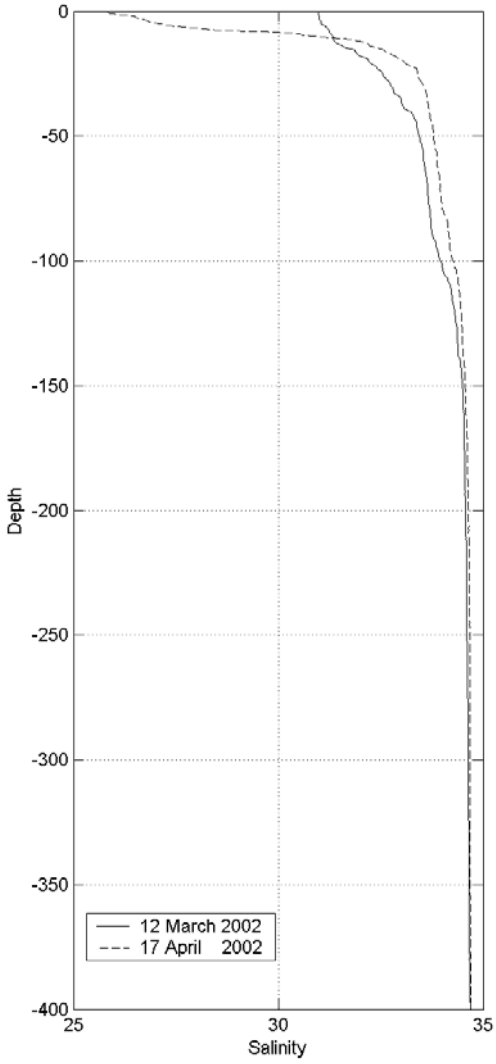

Figure 5.1 Vertical salinity distribution for 12 March and 17 April 2002 at Station 15 in the Trondheim Fjord.

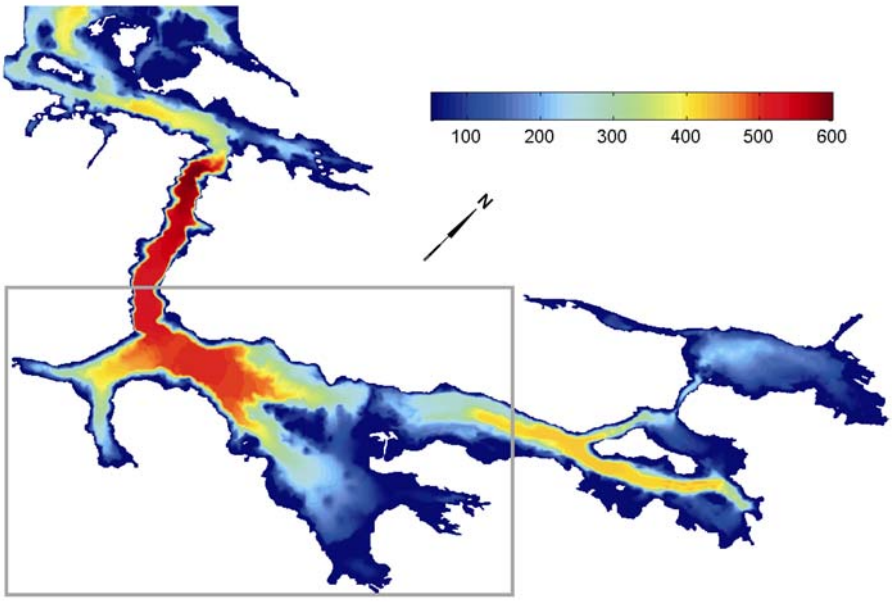

Figure 5.2 The bathymetry of Trondheim Fjord. The gray rectangle demarks the part used in simulations in which tidal forcing is not included.

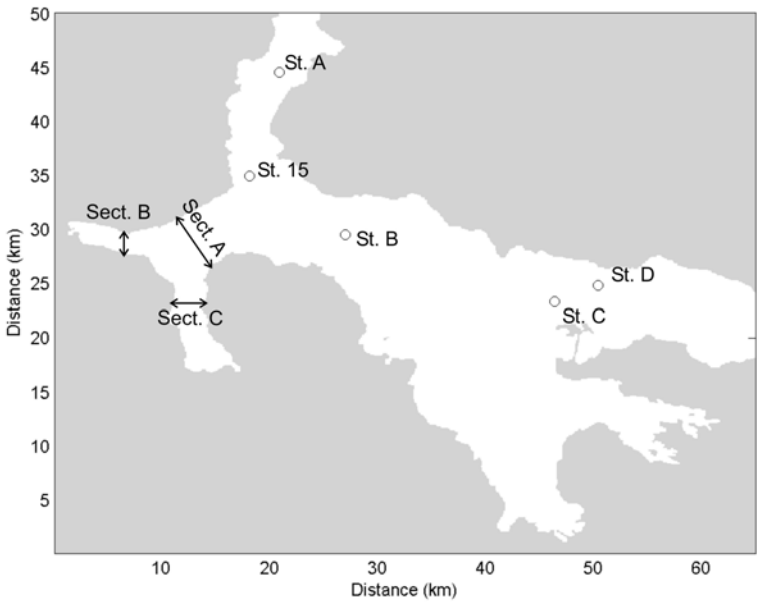

Figure 5.3 The location of stations (St.) and Sections (Sect.) referred to in the text. (Stations A to D are used in Chapter 7)

Table 5.1 Configuration information for cases 1 to 3. The river discharge, Q_{riv}, is equal for all the rivers.

Case	*Days*	*Coriolis*	*Tides*	*Initial Stratification*	Q_{riv} (m^3s^{-1})
1	0- 10	x	-	April	100
	10-12	x	-	-	0
	12-14	x	-	-	50
2	0-5	x	x	April	100
3	0-3	x	x	March	100

5.3 Results

5.3.1 Case 1: No tidal forcing

In Case 1 the model has been run for a total of 14 days: 10 days with river discharge, 2 following days without discharge and then 2 more days with half the earlier discharge (see Table 5.1 for details). The internal Rossby radius and the inertial radius, presented in Chapter 4, are calculated by approximating the plume and the deep water below as two layers. The velocities and density of the upper layer are found by calculating the mean values within the plume, and the lower layer is represented by the density and velocity found underneath the plume. The radii are then calculated according to equations 4.2 and 4.3.

Development of anticyclonic circulation

The Orkla discharge is directed toward the northwestern shore of the Orkdal Fjord. The surface salinity distribution in the Orkdal Fjord after 24 h is presented in Figure 5.4 for Case 1. In the absence of rotation the plume thickness is greatest along the northwestern coast of the fjord. The rotation causes the jet induced by the river discharge to turn according to a radius comparable to the inertial radius. As observed in Chapter 4, the plume further progresses as a coastal trapped current driven by buoyancy. The width of the current is of the same scale as the baroclinic Rossby radius, r_o. Consistent with laboratory simulations (McClimans, 1983), an anticyclonic circulation develops in the backwater of the jet. The radius of this anticyclonic circulation is further observed to increase and so is the radius of the turning of the jet. This is to be expected as the plume is in a developing phase and the jet associated with high velocities grows larger. The anticyclonic circulation is, however, not as conspicuous as one would expect from the field measurements presented in McClimans (1979).

Figure 5.6 presents simulated currents in the surface and at 3 m depth after 4 days of simulation. Beneath the plume, at approximately 3 m depth, the anticyclonic circulation dominates the currents in the innermost part of the Orkdal Fjord, even though the flow at this depth is comparatively weak. A cyclonic eddy is located farther out in the Orkdal Fjord. The cyclonic eddy is

related to the return flow. The return flow is stronger along the northwestern shore of the Orkdal Fjord, consistent with the influence of rotation. The ORP is found to be thicker along the southeastern coast of the Orkdal Fjord, and the flow is observed to be still out of the fjord arm at 3 m depth. Together with the return flow on the other side, this flow seems to generate the cyclonic eddy seen in Figure 5.6 b).

The river Gaula is located at the northeastern corner of the Gaulosen fjord arm. The outflow is found to be initially radial. The plume of freshwater is transported toward the southwestern shore before it turns to the right. The surface distribution of salinity after 1 day is given in Figure 5.5. There is no further sign of an anticyclonic circulation generated within the river plume, which can also be seen after 4 days (Figure 5.6 a)). Beneath the plume, at around 3 m depth, the flow is more complicated. The flow is weak, but is found to form a system of cyclonic and anticyclonic eddies and circulations. An anticyclonic circulation pattern is seen where there is a flow in toward the head of the fjord along the northwestern shore, and to the right along the southeastern shore. A similar pattern is found farther out, though weaker. Outside Børsa, a cyclonic eddy is observed. It is generated as the flow of GRP interacts with the local topography. This eddy is observed for all the simulations performed for the Trondheim Fjord. At 3 m depth an outflow is found along the southwestern side of Gaulosen north of Børsa. This flow continues following the shore of Viggja nearly reaching the Orkdal Fjord.

The Nidelva River Plume (NRP) is free to expand into the widest part of the fjord. A coastal current is seen to develop and propagate along the coast to the left of Lade, as seen from the surface currents in Figure 5.7 a). A bulge region with a tendency to anticyclonic circulation builds up in time. At 3 m depth this circulation is even more evident. A cyclonic circulation is also found closer to the river inlet. As time passes, a turning of the jet region of the NRP is observed. Instead of deflecting to the right, as expected from the Coriolis effect, the jet deflects to the left, i.e. to the west. As the fresh water discharges into the fjord, the plume thus builds up an anticyclonic circulation that in turn interferes with the outflow from Nidelva.

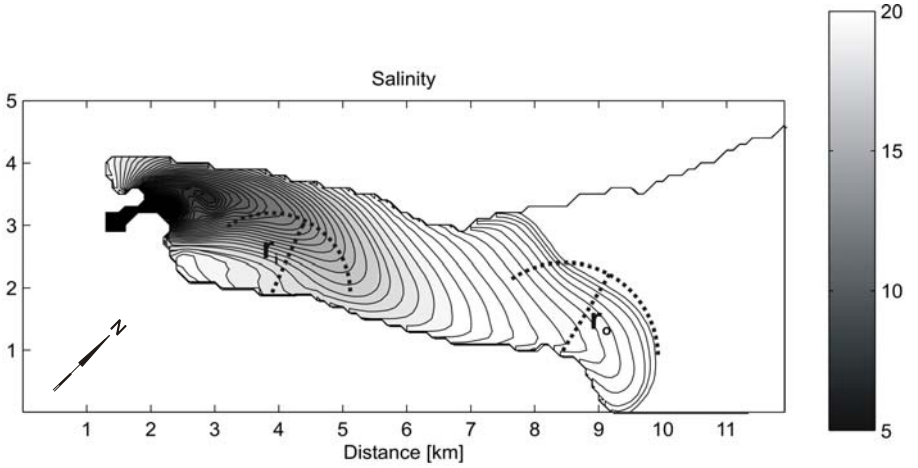

Figure 5.4 Surface salinity in the Orkdal Fjord after t = 24 h. The contour interval is 0.5. The baroclinic Rossby radius and the inertial radius are calculated from values representative for the area where they are drawn.

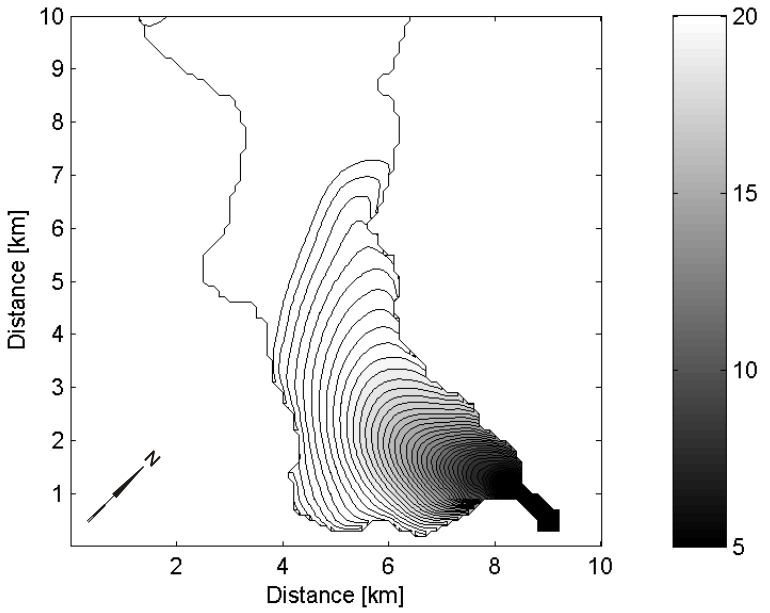

Figure 5.5 Salinity distribution in Gaulosen at t = 24 h. The contour interval is 0.5.

a)

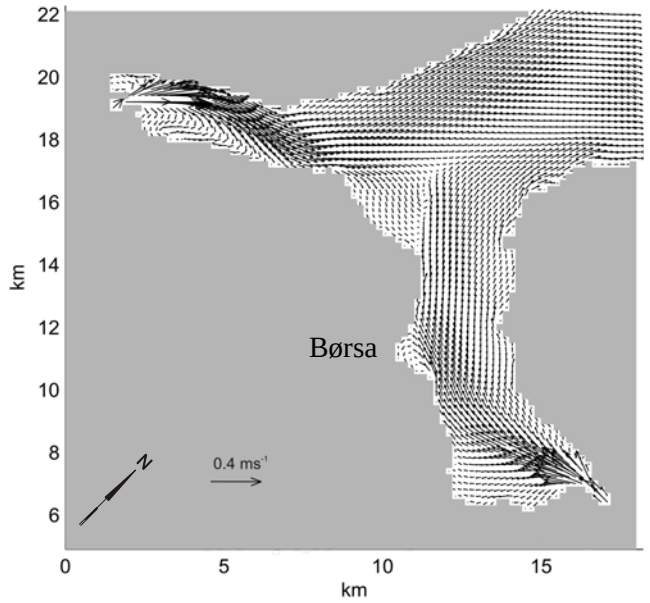

b)

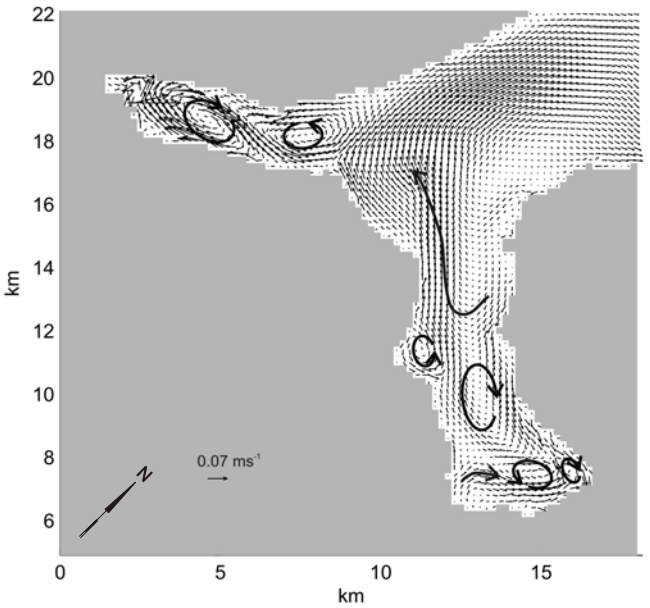

Figure 5.6 a) Surface currents and **b)** currents at 3 m depth in Gaulosen, the Orkdal Fjord and the Cross Fjord after 4 days of simulation.

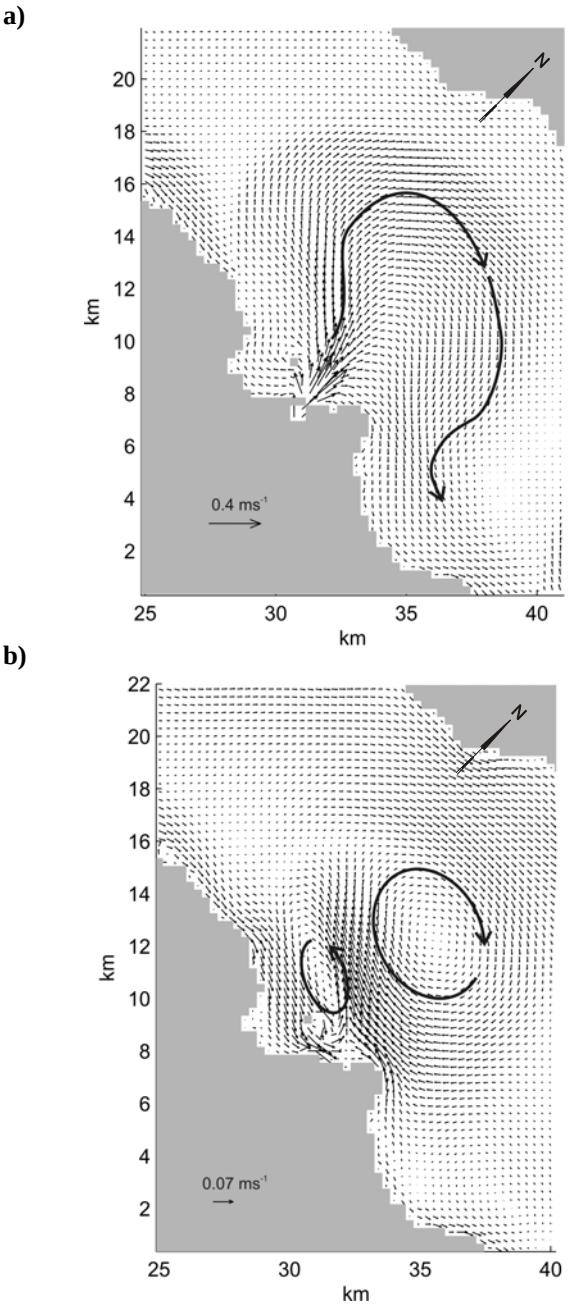

Figure 5.7 Currents outside Trondheim for **a)** the surface layer and **b)** at 3m depth after 4 days of simulation.

Interaction between the Orkla River plume and the Gaula River plume

The Cross Fjord is a particularly interesting part of the Trondheim Fjord since it is the meeting place of two buoyant plumes entering from the Orkdal Fjord and Gaulosen. The plumes have to some degree formed density driven coastal currents travelling in the direction of Kelvin wave propagation. ORP propagates toward Gaulosen along the shore of Viggja. From Gaulosen, the GRP enters the Cross Fjord, trapped to the shore of Byneset (Figure 5.8). Even though the Coriolis force causes the plumes to deflect to the right and the plumes are accordingly thicker on their right hand side, the buoyant water of the plumes is found to cover the whole surface of both fjords. This means that the ORP is not free to propagate further into Gaulosen. The collision between the plumes starts in the outermost part of Gaulosen. It happens gradually, starting with the outer tongue of ORP colliding with the GRP. Initially, after the collision, the ORP manages to push the GRP partly back towards Gaulosen along the southwestern coast of Byneset. The buoyant outflow from Gaulosen is now constrained by ORP and topography into a narrow outflow along Byneset (Figure 5.8). The occluded front and the two fronts associated with the ORP and the GRP forms now a y- shaped structure seen both in the surface divergence field and in the vorticity field as shown in (Figure 5.11). Along the occluded part of the front, a cyclonic eddy develops and forms a pool of local positive (cyclonic) vorticity.

The GRP is slightly less dense than the ORP. As the occlusion process continues, the saltier and hence less buoyant water of the ORP partly submerges beneath the GRP (Figure 5.10). This was observed by McClimans (1979).

The passive tracer applied to the discharge from Orkla is shown in Figure 5.9 for the surface and at around 3 m depth for three points in time. It is seen that traces of Orkla water are found further into Gaulosen at 3 m depth than in the surface layer. An eddy is also seen generated as a filament of the ORP intrudes along the southeastern coast of Gaulosen. Some of the ORP water is entrained into the GRP, as seen from the surface plots in Figure 5.9. The ORP partly blocks the outflow from Gaulosen and buoyant water accumulates in the Gaulosen. A horizontal pressure gradient builds up, which, at one point gets large enough to enable the GRP to force the ORP back and out of the Gaulosen again (Figure 5.9 b) and c)). This in turn causes

the outflow from the Orkdal Fjord to be directed more to the north in the Cross Fjord. As the ORP expands in the Cross Fjord, it manages once again to push the GRP toward the shore of Byneset. The GRP accelerates in the part constrained by the ORP and topography and spreads horizontally immediately after passing the ORP in the Cross Fjord. As the GRP expands, the fronts of the GRP and ORP occlude and form another y-shaped front. A cyclonic eddy develops as described above. In time, the eddy generated earlier in the occlusion process is observed to catch up and merge with the new one. In the center of the cyclonic eddies small local pools of cyclonic vorticity are observed (Figure 5.11). The frontal region is relatively narrow and this seems to limit eddies from further growth.

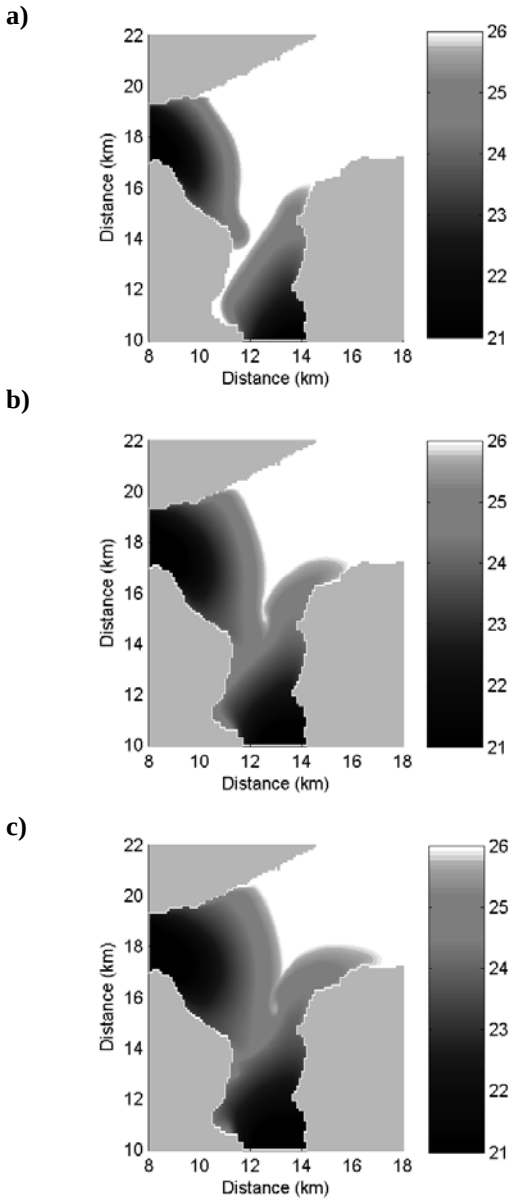

Figure 5.8 The surface collision of the GRP and ORP. Surface salinity at **a)** t = 34 h, **b)** t = 42 h and **c)** t = 48 h.

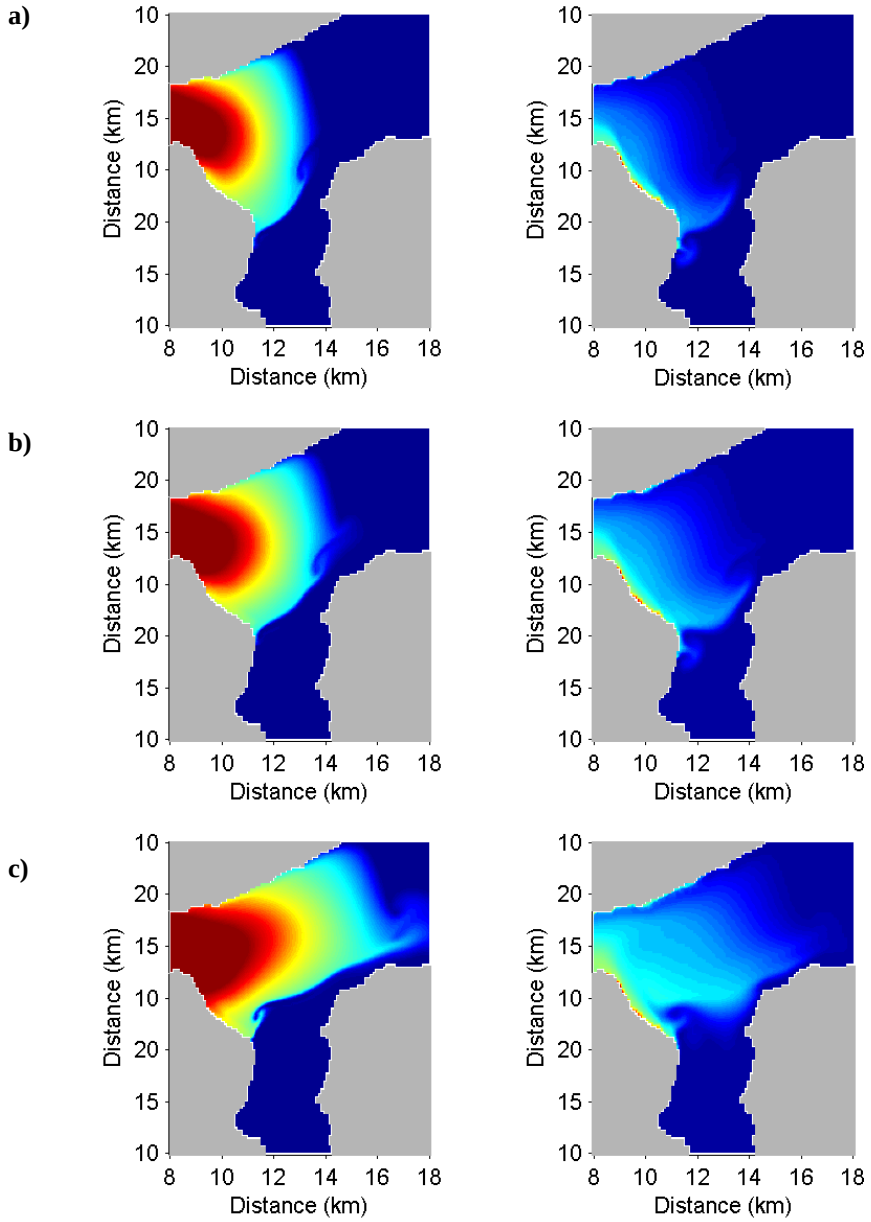

Figure 5.9 The distribution of a passive tracer at the surface (left panel) and 3 m depth, (right panel) at **a)** t = 48 h, **b)** t= 56 h and **c)** t = 72 h.

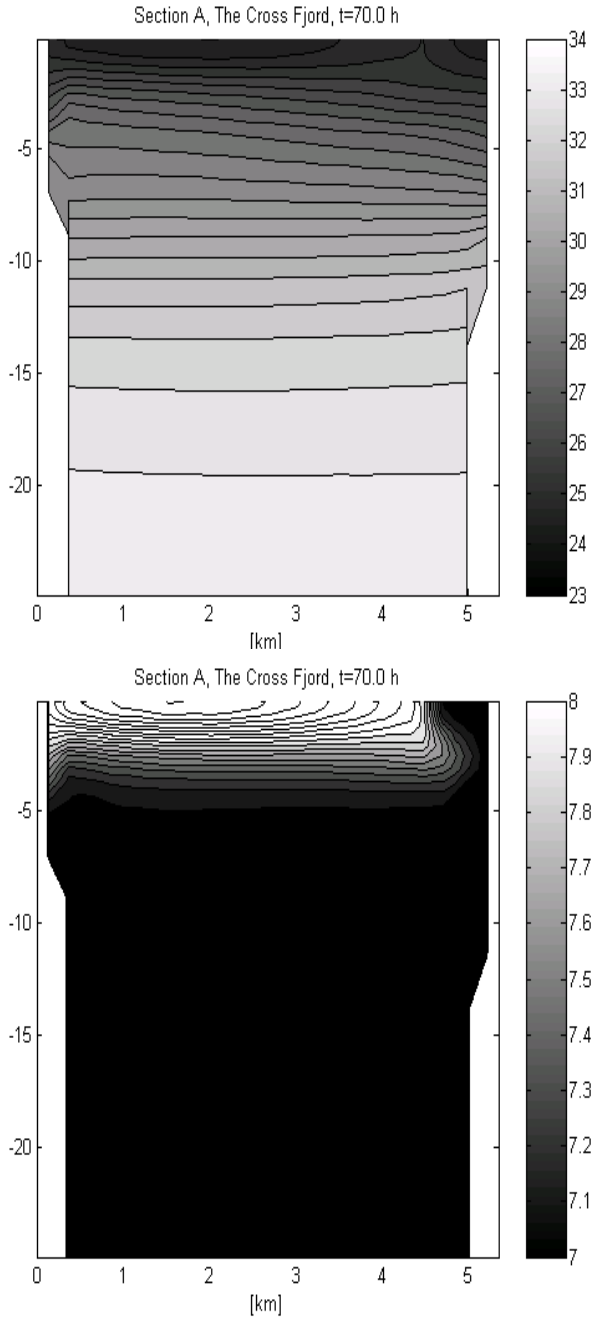

Figure 5.10 Vertical section of salinity (upper) and a passive tracer used to mark Orkla water (below) along Section A (Figure(5.3)) after 3 days of simulation,.

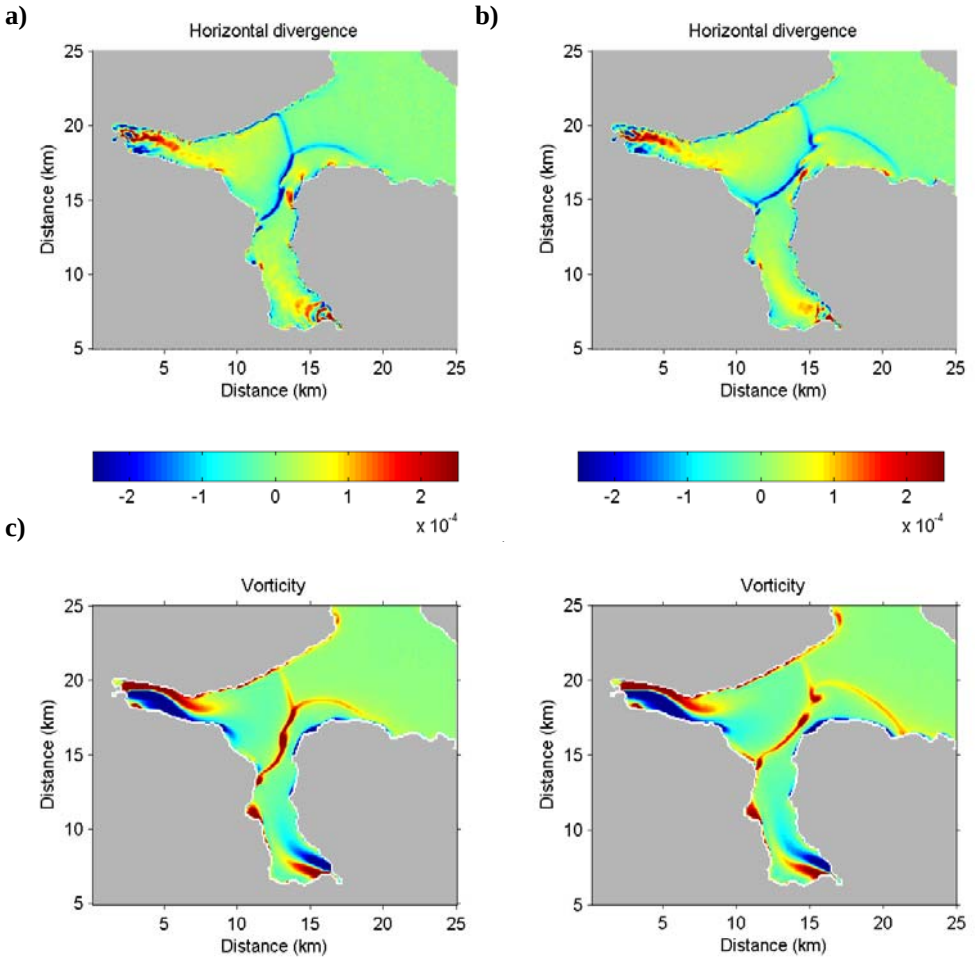

Figure 5.11 Horizontal divergence at the surface for **a)** t = 48 h, **b)** t = 60 h. Surface vorticity for **c)** t = 48 h and **d)** t = 60 h**.**

Cyclonic spiral eddies

The cyclonic eddies generated along the occluded front mixes the ORP and GRP waters. This mixture, in addition to the GRP water closer to the shore, continues to propagate as a density driven coastal current along the northern side of Byneset. After approximately 5 days of simulation start this coastal current collides with the NRP. Another y-shaped frontal structure appears as the fronts occlude. After 10 days, the occluded front between the nearly mixed GRP and ORP plume and the NRP is seen in Figure 5.12 a) and c) along the west side of the NRP. To the left of this front a pool of cyclonic vorticity is seen. This originates from the cyclonic eddy formed from the interaction between the GRP and ORP in the Cross Fjord. After 2 more days of simulation a spiral eddy has developed at this location as seen in Figure 5.12 b), d), e) and f). This eddy develops as a result of the interaction between the NRP with the mixture of ORP and GRP water. The latter manages to propagate further towards the east along the southern side of the Flakk Fjord. On the other side of the fjord the flow is in the other direction. Water of NRP origin is found closest to the shore and pushes the water on the other side of the front towards the west. There is thus a horizontal cyclonic shear in the flow that supplies the eddy with energy to grow.

On the east side of the NRP there is another cyclonic eddy. The eddy is initially formed along the part of the front that separates the bulge region of the plume to the left from the coastally trapped density driven current to the right. At this location the front occludes with itself as the NRP becomes unstable and an eddy develops at the end of this occluded front. The process is thus similar to the eddies forming in the Cross Fjord as described above. As time progresses, a horizontal shear flow results from the interaction between the plumes in the area that further feed the eddy with energy. After 12 days, the frontal interface has wound up into a spiral. It then gets advected with the anticyclonic circulation set up by the Nidelva discharge, towards the west.

The river discharges are set to zero after 10 days and the flow is allowed to develop over 2 days before two more days of river discharge is simulated with $Q_{riv} = 50$ m s^{-1}. The horizontal divergence of the surface flow is shown in Figure 5.13 after 13 days. Again the lines of convergence are used to study

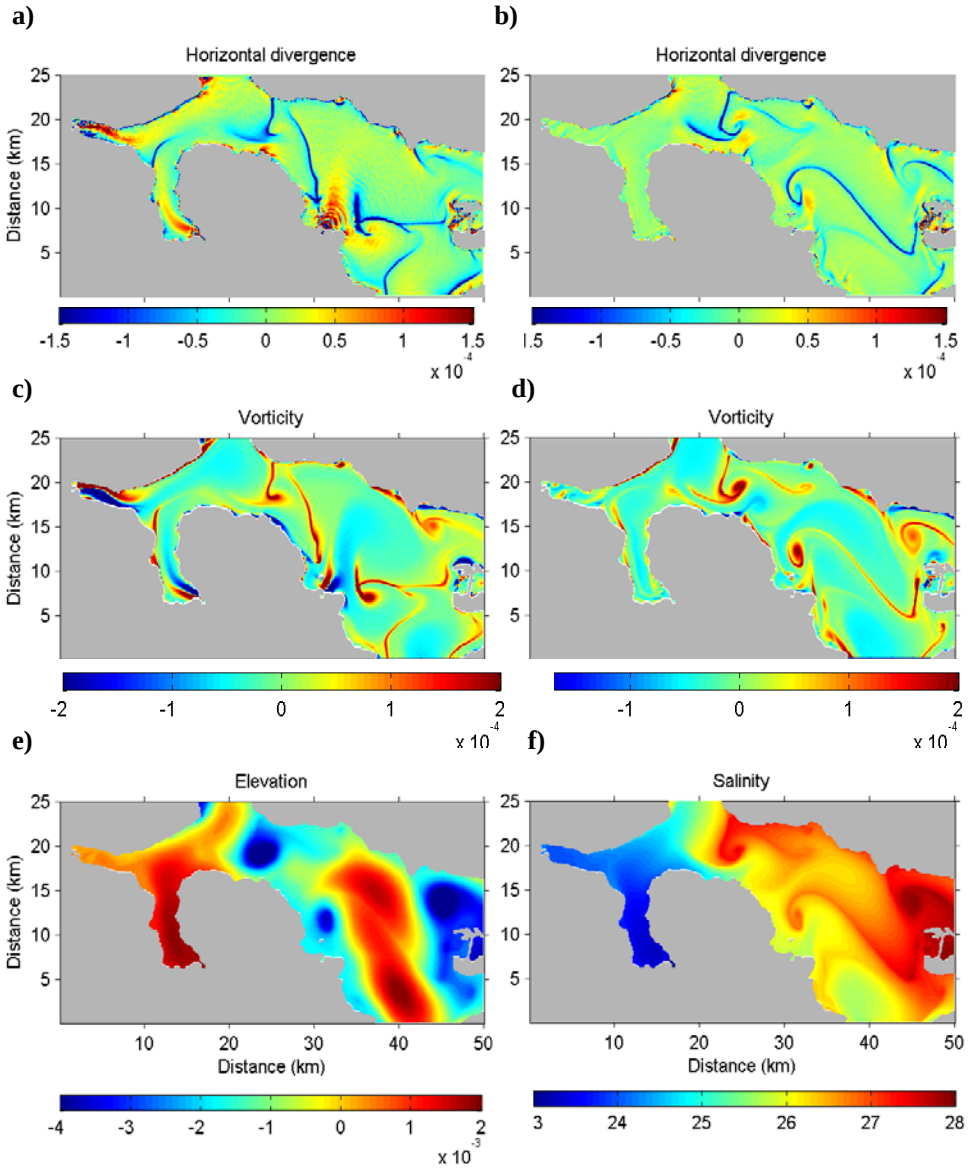

Figure 5.12 The figure shows the development of cyclonic eddies. In a) and b) horizontal divergence calculated for the surface layer is shown for t = 10 d and 12 d, respectively. The surface vorticity is shown for c) t =10 d and d) t = 12 d. In e) the elevation is displayed for t = 12 d and in f) surface salinity for t =12 d.

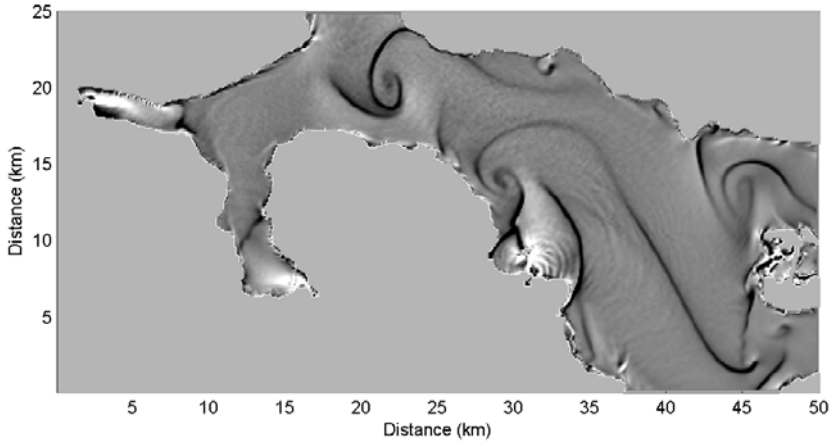

Figure 5.13 The surface horizontal divergence in the surface after 13 days.

the behaviour of the river plumes. The Nidelva River discharge is seen to divert to the left, and the front associated with this plume is observed to merge into the spiral eddy found in the area.

5.3.2 Cases 2 and 3

Characteristics of the internal tide in the Seaward Basin

In cases 2 and 3, the simulations are performed with forcing of semi-diurnal tides. Long waves are generated as the tides flush back and forth over the Tautra sill. The period of these waves is the same as the semi-diurnal barotropic tide, i.e. 12.4 h and the wave propagates cyclonically around the Seaward Basin.

The phase and amplitude of the waves are found by performing a Fourier analysis of the time series of the depth of one particular isohaline. The phase and amplitude obtained by this analysis will depend on which ishohaline is chosen. A comparison of the amphidromic systems for different isohalines shows that the main properties of the phase are only slightly changed in the upper 100 m. The amplitude decreases, on the other hand, naturally towards the surface. The phase and amplitude for the $S = 33$ isohaline for Case 4 is displayed in Figure 5.14. The phase decreases with distance to the west and to the east of the Tautra sill. The only way this is possible is if the waves are generated at the sill. The generation of internal waves is shown in Figure

5.14. Internal waves of different wavelengths propagate at nearly constant velocities away from the Tautra sill. Waves are also seen to propagate in the other direction in the left part of the plot. These are long waves that propagate along the shore on the other side of the basin, and hence in the other direction. The phase velocity calculated on the basis of this plot is estimated to be $c_f^{33} \approx 0.55$ m s^{-1}, where the superscript 33 indicates that this is for the S = 33 isohaline. This gives a wavelength $L^{33} = c_f^{33} / T \approx 24.6$ km. The baroclinic Rossby radius is further found to be $R_b = c_f^{33} / f \approx 4.2$ km.

There are several amphidromic points in the basin: in the Åsen Fjord, in the southern part of the Strind Fjord, near the coast west of Trondheim, near the coast of the northern part of Byneset and there is also a hint of one in the southern part of Gaulosen. The largest amplitudes of the internal tide are found at the northern part of the shore west of Tautra, and along the southern part of the shore east of Tautra. This is consistent with the effect of Coriolis at long waves. In the Orkdal Fjord the amplitude is also found to be comparatively large with values up to 8 m. The amplitude elsewhere in the area including the Cross Fjord and Gaulosen are associated with relatively low amplitudes, around 0 - 2 m.

The high amplitude of the internal wave in the Orkdal Fjord, that increase from nearly zero near the inlet to around 8 m near the river mouth, may be explained by wave resonance. The length of the internal Kelvin wave was estimated to be around 24.6 km and the Orkdal Fjord is around 6 - 7 km. Quarter wave resonance may then occur, as discussed in 5.1, causing a significant amplification of the internal wave.

Case 3 is configured with an initial stratification based on data from Station 15 from 17 April 2002. The amphidromic system calculated for this simulation shows no characteristic resonance in the Orkdal Fjord. The phase speed of the wave is found to be approximately $c_f^{33} \approx 0.70$ m s^{-1}, and the wavelength accordingly $L^{33} \approx 31.2$ km. The internal tide studied in the next chapter has the resonance effect, and is therefore of interest.

Internal waves and internal hydraulic jumps

NCOM is based on the hydrostatic form of the primitive equations. It is generally known that this is not a valid approximation when dealing with

waves of high frequencies. The model does, however, reproduce the generation of internal waves for instance over the Tautra sill and their propagation away from the sill in both directions (Figure 5.15). There are fluctuations of the 33 isohaline at the sill that have maximum amplitudes of 10-15 m when the tidal currents are at the strongest. When the tidal flow weakens, high frequency internal waves are observed to propagate away from the sill in both directions, in addition to the internal Kelvin waves studied above. These waves are conspicuous features of both surface elevation and also of the horizontal divergence of the surface flow.

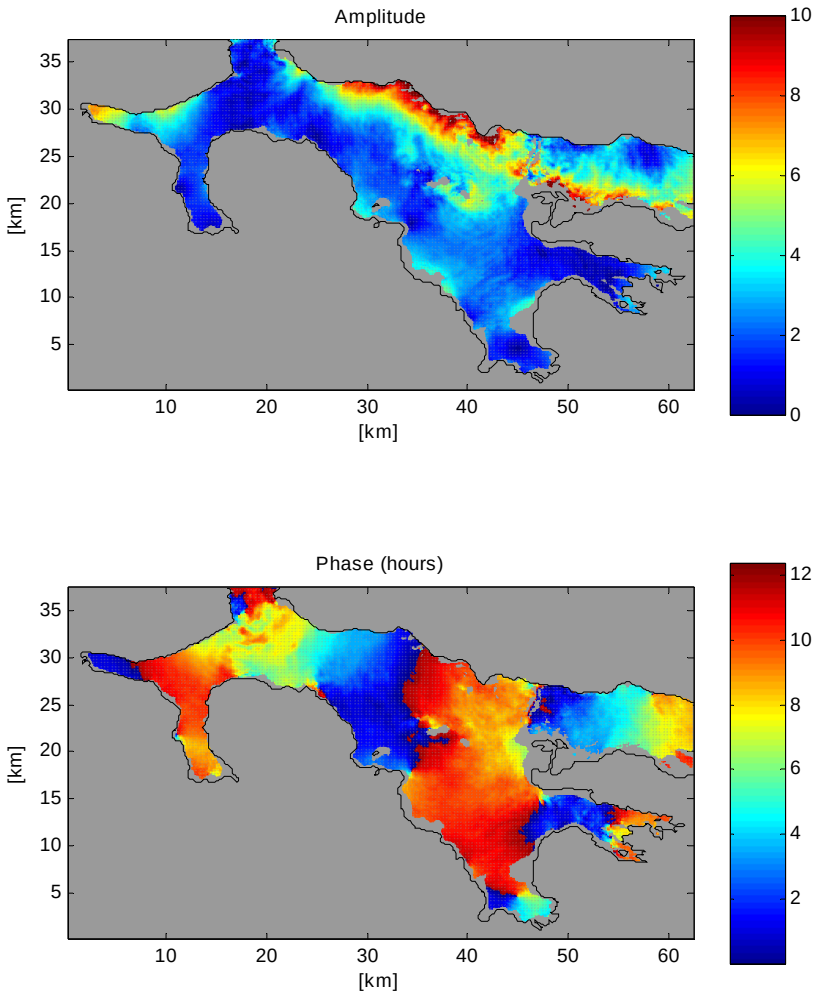

Figure 5.14 a) Amplitude and **b)** phase of the internal tides simulated in Case 3.

URN:NBN:no-3496

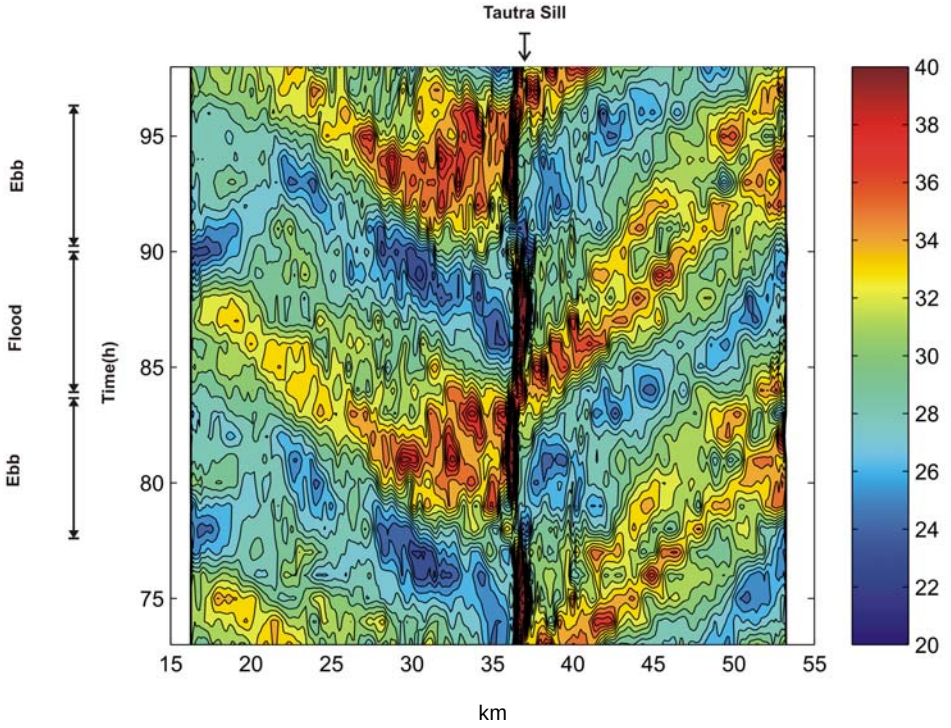

Figure 5.15 The depth of the *S* = 33 isohaline across the Tautra Sill plottet for y = 27 km, see Figure 5.14, along the x-axis and time along the y-axis.

Influence of the internal tide

In case of no tides the buoyant outflow from the Orkdal Fjord was more or less constant due to the constant discharge from the Orkla River. When simulations are performed with the forcing of tides, this is no longer necessarily found to be the case. The outflow is much more irregular. There are periods when the outflow from the Orkdal Fjord is at a minimum and during other periods an energetic outflow is observed. What may at first seem like a paradox is that the outflow occurs as the surface elevation increases, or during rising tide. The tidal currents associated with the surface tides are small and much smaller than the buoyancy driven current of the ORP. The correlation though seems to be with the internal tide. Internal tides are not necessarily in phase with the barotropic tide. The surface currents of the internal tide may also be comparatively large, especially in the environment studied here, with a relatively large depth and a relatively shallow brackish surface layer. The model produces velocities of order 10^{-2} m s^{-1} beneath the upper buoyant layer, and of order 10^{-1} m s^{-1} within the upper layer. For Case 2 without tides, the total transport through Sections B and C in Figure 5.3 is found to vary around 100±5 $m^3 s^{-1}$, consistent with the constant discharges of 100 $m^3 s^{-1}$ each transported into the respective fjords by Gaula and Orkla.

The variations of the volume transports with the tides across Sections B and C is shown in Figure 5.16 and Figure 5.17. The depth of the plume is here computed in a similar manner as in Chapter 4. In Figure 5.16 a) the volume transports of the ORP are shown together with the transport below the river plume. These two transports are out of phase. The barotropic tidal current dominates the transport beneath the plume, while the transport within the plume behaves oppositely. The surface elevation for a location along Section B is shown together with the depth of the S = 33 isohaline for comparison. The correlation between the internal tide and the volume transport in the GRP is significant, even though there are variations beyond this. The anticyclonic circulation driven by the river discharge may also influence the transports in the area. Generally, the outflow in the buoyant surface layer across Section B becomes greater as the internal tide turns from flood to ebb, i.e. when the surface currents associated with the wave are

divergent. Similarly, a flow toward the head of the Orkdal Fjord is found when the internal tide turns from flood to ebb.

The variations of the volume transport within the GRP are less than observed for the ORP (Figure 5.17). The internal tide is observed to have less amplitude and is in this sense weaker in Gaulosen than in the Orkdal Fjord. The outflow in the buoyant layer in Gaulosen is also less influenced by the internal tide. There are, however, fluctuations of shorter time scale seen in both Figure 5.17 a) and Figure 5.17 b) that are more dominating.

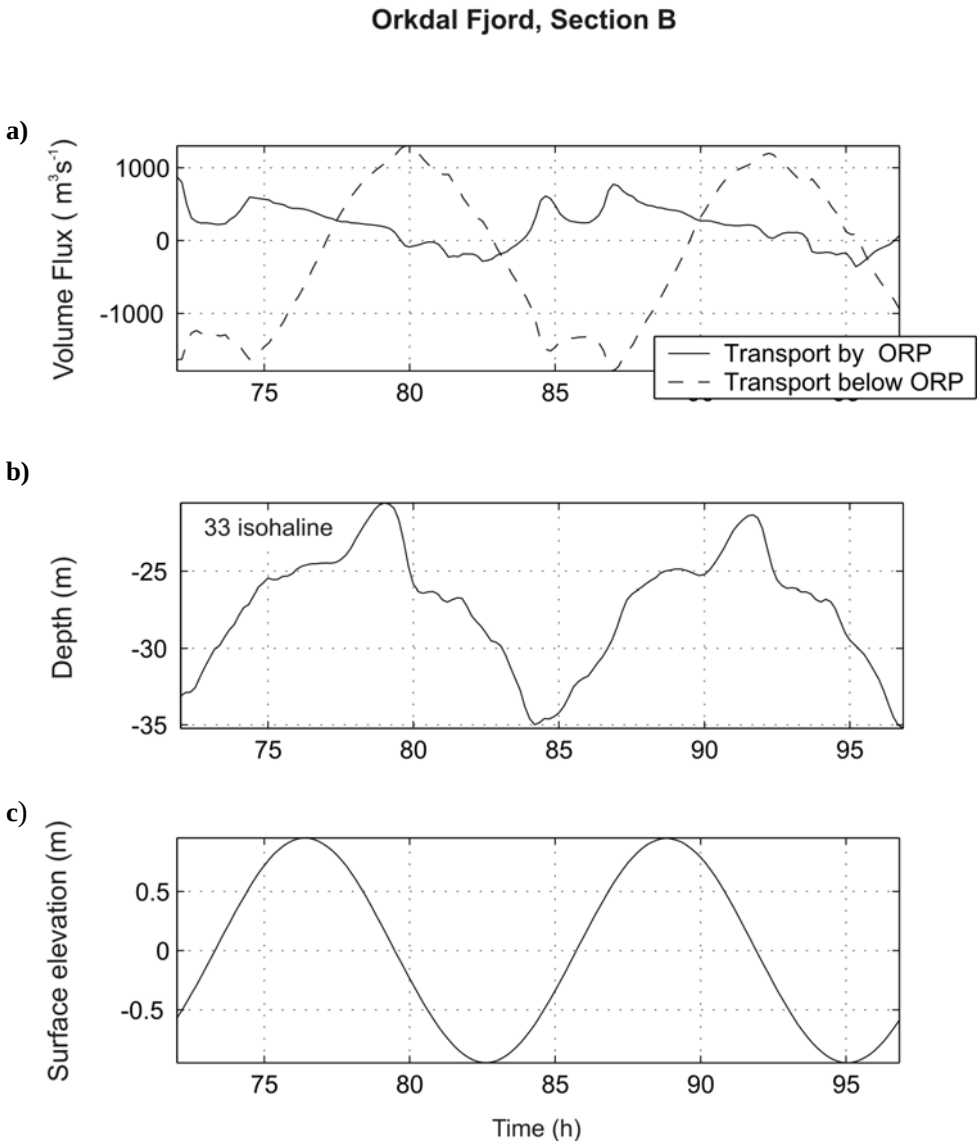

Figure 5.16 Upper plot, **a)**, shows transports through Section B separated into the transport by the Orkla River Plume (ORP) (solid line) and beneath the plume (dashed line). The two lower plots demonstrate the tidal activity by the **b)** barotropic and **c)** baroclinic tides.

URN:NBN:no-3496

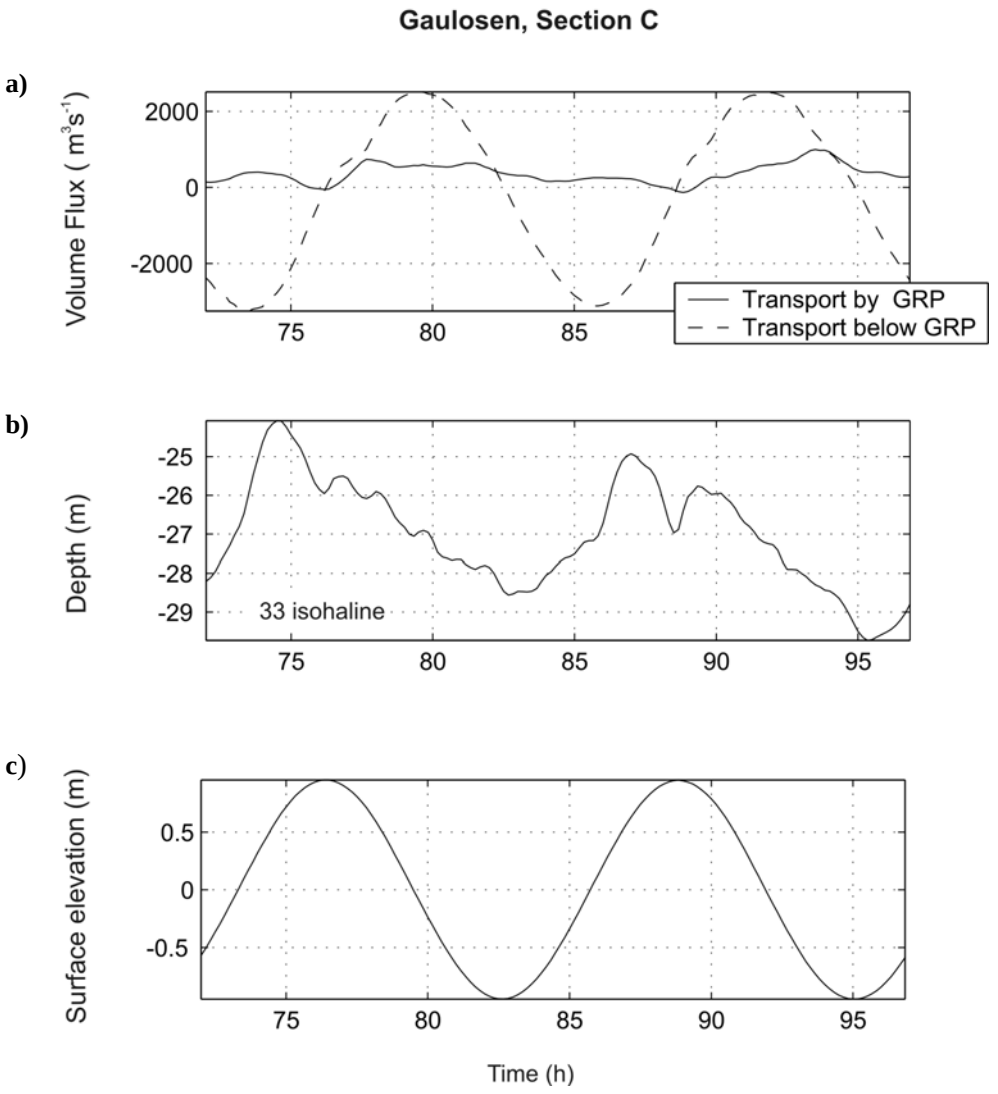

Figure 5.17 Upper plot, **a)**, shows transports through Section C separated into the transport by the Gaula River plume (GRP) (solid line) and beneath the plume (dashed line). The two lower plots demonstrate the tidal activity by the **b)** barotropic and **c)** baroclinic tides.

5.4 Discussion

Rotation

That rotation of the earth may have significant effects on river plumes was shown by Eidnes (1982) and McClimans (1979; 1980). It was also demonstrated in Chapter 4 for a river discharge into an idealized basin. The development of the Orkla River plume the first day is also quite similar to the results described in Chapter 4. Since the Orkla river transports the freshwater towards the left shore there is a greater effect of background rotation. The path of the jet is longer before hitting the shore on the other side of the fjord than would be the case if the discharge were directed the middle of the basin. In Gaulosen, with a width of around 3 km, compared to 2 km in the Orkdal Fjord, the plume is also seen to turn according to the Coriolis effect. There is, however, no indication of the formation of an anticyclonic circulation as found in the Orkdal Fjord. Beneath the plume in the jet part there is observed anticyclonic circulation patterns in both fjords.

Another interesting result is that one of the effects of the internal tides is an enhancement of the anticyclonic circulation in the Orkdal Fjord. This is also more in accordance with the observations described in McClimans (1979). The development of the Nidelva River has the general characteristic of a river plume discharging into a wide basin, i.e. a higher Kelvin number case (Garvine, 1995). It is also observed that the anticyclonic circulation of the bulge regions acts upon the discharge causing it to divert to the left rather than to the right, which is expected from the Coriolis effect.

River plume interaction

The interaction between two river plumes is described for the ORP and GRP in particular. When the plumes collide, either with a solid wall or with another plume, internal, bore-like waves are generated that travel away from the point of collision. Bores are also observed to generate when gravity currents collide in the laboratory, an analogous situation to the colliding river plumes (Simpson, 1997). Internal bores mix water as they propagate, and such phenomena may thus contribute to mixing between the plume water and the ambient. These bores will be discussed further in chapters 6 and 8.

After the collision, the ORP was the forced to submerge beneath the GRP, and the fronts occluded. Simpson (1997) describes similar behaviour for the gravity currents colliding in the laboratory.

Spiral eddies

The baroclinic process of occlusion of two different water masses in a third water mass result in a y-shaped front, where the tail of the letter y is the occluded part of the frontal system. A cyclonic eddy is seen developing at the end of the tail soon after the occlusion occurs. It seems to be formed as the increased shear along the occluded front causes it to break and engulf water from one side of the front to the other. There is thus a distortion of the frontal boundary in a cyclonic manner and a cyclonic eddy develops. This eddy become a feature of the front separating the ORP and GRP, and was advected with the buoyancy driven flow out of the Cross Fjord. The extension of the frontal boundary is though small, only a few 100 m, and the growth the eddy is thus limited. When expanding into the Seaward Basin the ORP and GRP, which are partly mixed with each other, will interact with the NRP. This interaction results in a horizontal shear across the front that causes the eddies to grow and wind up into spiral eddies. The spiral eddies described from the numerical results presented in this chapter thus seem to result from both barotropic and baroclinic processes. For simplicity, these spirals are described for simulations that are not forced by tides.

Internal tides

Internal tides are generated as the barotropic tides interact with stratification across the Tautra sill. In the Knight Inlet the power drawn from the barotropic tide is fed into the internal tide (Stacey, 1985). Energy of the internal tide dissipates within this inlet and leads to mixing which is important for the circulation in the inlet. There may be a similar situation in the Trondheim Fjord, which is interesting since the tide is considered to be the main source of energy in the fjord (Jacobson, 1983). During specific periods the results presented by Stacey indicate also significant contributions from non-linear waves. Figure 5.15 illustrates how both internal tidal waves and non-linear high frequency waves are generated across the Tautra sill.

The focus of this study is on how freshwater is spread from rivers. The effect of the internal tide in the Orkdal Fjord, which is actually a half-open basin, is therefore a particularly interesting result. The regulation of the freshwater outflow from this part of the plume is also found for the results presented in the next chapter.

5.5 Summary and conclusions

Simulations have been performed using NCOM to study the effects of background rotation and tides on the spread of freshwater from rivers. Results have shown that both have significant effects on the resulting flow. The rotation of the earth affects the development of the plumes and induces circulations that are important for mixing between the water of river origin and ambient water.

Spiral eddies are reproduced at the interface between water of different density. The patterns observed at the surface are very similar to some of the spiral eddies shown in images presented in Munk et al. (2000). In this study, the eddies are found to develop from frontal occlusion processes. Horizontal shear causes the eddies to grow further and to eventually wind up the local frontal interface into cyclonic spirals.

Baroclinic tide are generated when the barotropic tides interact with the stratification across the Tautra sill. Internal tidal waves are observed to propagate around the Seaward Basin. The effect of this internal tide on the spread of freshwater is most evident in the Orkdal Fjord. There is a resonance of the internal tide in this part of the fjord. This results in a retarded outflow from the Orkdal Fjord occurring twice a day. During this period, freshwater is accumulated in the fjord leading to a subsequent energetic outflow.

URN:NBN:no-3496

Chapter 6

Effect of internal tides and rotation of the earth at the spread of freshwater from rivers in the Trondheim Fjord

A particular solution

URN:NBN:no-3496

Abstract

The Navy Coastal Ocean Model (NCOM) is used for high-resolution simulations of the Trondheim Fjord for April 2002. The results show that river plumes are affected by internal waves and modified by the effect of the earth's rotation, as discussed in Chapter 5. These new findings are related to previous observations and descriptions of the physical environment of the fjord.

Keywords: fjord, river plumes, frontal occlusion, spiral eddies, internal tide, internal tidal resonance.

6.1 Introduction

Simulations are presented for the Trondheim Fjord for April 2002. This was a period of weaker winds that favors a study of river plume dynamics. The effect of background rotation and tidal forcing studied in Chapter 5 will here be studied in a more realistic fjord flow. The studies of Jacobson (1977; 1983) are used as a reference for the surface flow. The simulation results are also used to explain some of the behavior observed in some of the observations presented in Jacobson and reviewed in Chapter 2. A comparison between observations and simulations will be presented in the following chapters.

6.2 Model configuration

High and low resolution simulations

The simulations are started with a chosen, horizontally homogeneous vertical stratification. It is then run with forcing obtained from monitoring data (Table 6.1). To reproduce the flow and hydrographic conditions of the fjord, the simulations should be spun up for at least a few months. High resolution is required for the simulations in order to resolve the physical processes attributed to the freshwater discharges. Simulations with a horizontal grid spacing of 100 m are, however, too computationally expensive to be run over such a long period. A configuration with coarser resolution is therefore applied. After approximately 3 months, the results are interpolated to a high resolution grid (Figure 6.1). To distinguish between these two set ups, I will refer to them as TrFjord-100 and TrFjord-500: The former has a horizontal grid spacing of 100 m and the latter 500 m. The bottom matrix for TrFjord-100 was shown in Figure 5.2. The configurations are otherwise similar as described in Section 5.2. The TrFjord-500 configuration was initiated on 20 December 2001. Salinity and temperature data from a vertical CTD profile at Station 15 on that day were interpolated vertically to the model grid. The model was then started with uniform horizontal distributions of salinity and temperature and zero velocities.

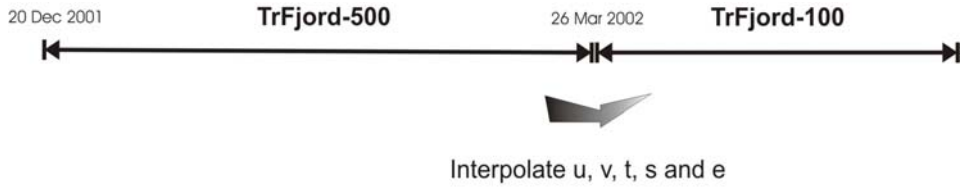

Figure 6.1 The Trfjord-500 configuration is run for about 3 months before the results are interpolated from a grid of 500 m horizontal spacing to a grid of 100 m.

Forcing

Tidal forcing is implemented by defining the elevation at the outer open boundary. Four tidal components are included in the simulations: K_1, M_2, S_2, and N_2. The amplitude, period and phase for each component are used to calculate the elevation. The data are provided by Statens Kartverk.

TrFjord-500 is forced with wind. This will be discussed further in the next section. Wind gauges were set up in the area around the Cross Fjord, Gaulosen and the Orkdal Fjord for three weeks from the last week in March 2002 to the middle of April 2002. The weather was generally calm all trough this period, and this persisted almost to the end of April. The TrFjord-100 configuration that is run for this calm period is thus run without the forcing by wind.

A heat flux routine is implemented in NCOM. The routine calculates the heat flux based on atmospheric data of wind stress, cloudiness, humidity and air temperature in addition to local sea temperature. The calculation also accounts for the length of the day at the particular time of the year. The results presented in this Chapter will be mostly from April 2002.

Daily values of river discharges for Orkla, Gaula, Nidelva, Stjørdalselva, Verdalselva and Steinkjærelva were provided by NVE (Norges vassdrags- og energidirektorat). The temperature of the river water is set to be equal for all rivers and is based on temperature measurements of the Orkla River water. The data are provided by Kraftverkene i Orkla. During the winter this temperature may be close to zero. A minimum value of 2 °C is applied to

discharged river water. River discharges in April 2002 for the six rivers included in the simulations are given in Figure 6.2. In the beginning of the month, the discharge of Orkla is low compared to that of Gaula. Both discharges are then around 100 $m^3 s^{-1}$ until the spring flood starts around 22 April.

Table 6.1 Forcing applied for the NCOM simulations. The river water has been given daily temperatures based on data from Kraftverkene i Orkla. Daily values are used for river discharges and for the atmospheric data used in the heat flux calculations. Wind stresses are calculated based on wind observations with a 3 h interval. The effect of wind stress is not included in TrFjord-100 (see text).

Data	Location	Source
Atmospheric Data		
Wind	Ørlandet	met.no
Air temperature	Ørlandet	met.no
Humidity	Ørlandet	met.no
Cloudiness	Ørlandet	met.no
River Discharge		
Orkla	Bjørset/ Syrstad	NVE
Gaula	Haga Bru	NVE
Nidelva	Rathe	NVE
Stjørdalselva	Hegra Bru	NVE
Verdalselva	Grunnfoss	NVE
Steinkjærelva	Hakedalsbrua	NVE
Tides		
N2, M2, S2, K1	Bjørset	Statens Kartverk

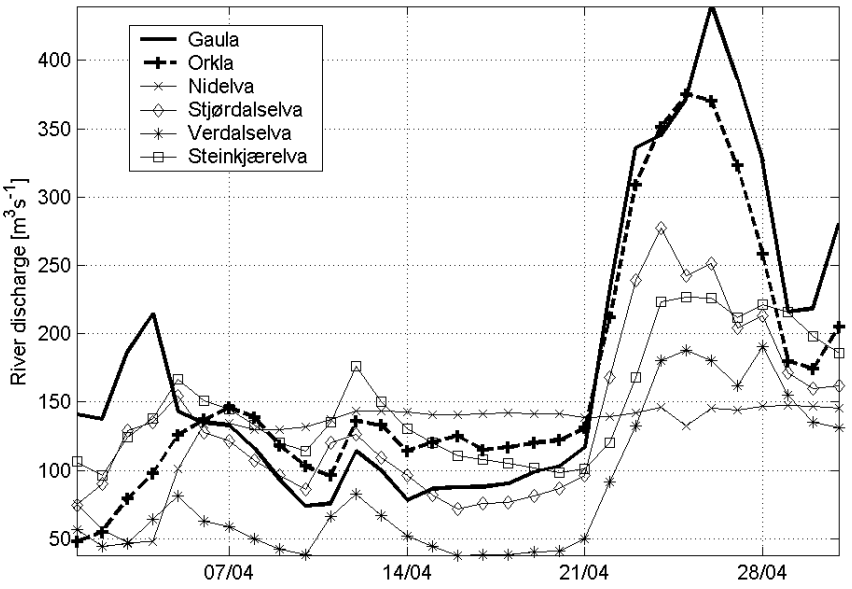

Figure 6.2 River discharge for the six largest rivers in the Trondheim Fjord from the period 1 April 2002 to 30 April 2002. Data are provided by NVE (Norges vassdrag og energidirektorat).

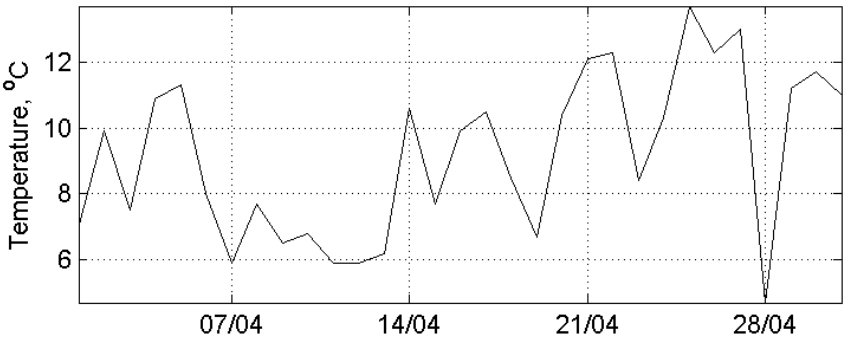

Figure 6.3 Air temperature from Ørlandet, data are plotted for t = 13:00 h each day. Data are provided by met.no.

URN:NBN:no-3496

6.3 Model spin-up: TrFjord-500

There are only two stations situated around the fjord that can provide us with a complete set of atmospheric data. These stations are at Ørlandet and Værnes (Figure 2.1). Ørlandet is located near the fjord inlet. Being closer to the open ocean, there are generally stronger wind events here than inside the fjord where the wind is damped by topography. On the other hand, due to local topography, Værnes is less windy than the air over the wide fjord. Clearly, it is not possible to feed the model with a realistic wind field based on data from only these two stations. A horizontally uniform wind was therefore applied. The TrFjord-500 has been run with data from both stations. To evaluate the simulations, the results have been compared with data from Station 15 for February and March 2002. This is the station located closest to the area of interest, where a vertical CTD profile is available for each month. The data give information on seasonal variation of the hydrography.

As one might expect the results showed high sensitivity to the choice of wind data. The best fit between model results and data from Station 15 was found when data from Ørlandet were applied. The simulated salinity and temperature profiles are shown in Figure 6.4. The model data are plotted with a 6 h interval for 12 March 2003. The simulated salinity and temperature in the surface varies during the day. This seems to be due to the tidal transport of freshwater plumes back and forth past the location. The upper wind-mixed layer is reproduced at approximately the same depth as seen from the field data at Station 15. One of the modelled salinity profiles shows a close fit with measured salinity of the surface layer. The simulated temperature for the upper surface layer, on the other hand, deviates with nearly 2 °C from the measurements. This may be related to the way the attenuation depth for short wave radiation is defined in the heat flux calculations. The layer depth in the calculations is fixed at 18 m until 1 April and from then at 5 m. These depths are typical for a winter and a spring situation in the fjord (Sakshaug and Killingtveit, 2000). The results have shown some sensitivity to the choice of these depths, which is reasonable, since this depth varies and is also different for different parts of the basin.

Discrepancies between simulations and data are found for both salinity and temperature at intermediate depths, i.e. from 20 m to 120 m. The main cause is likely related to the fact that the model does not include exchange

with the ocean outside. The different layers in the fjord are replaced due to the changing hydrographic conditions of the ocean outside the fjord inlet (Chapter 2). The longer period the model is run, the greater is the error by excluding this exchange. I have started the model run on 20 December. An earlier start, for instance in November, gave larger discrepancies. However, the model needs to spin up over a period of months in order to provide realistic input fields to the high resolution TrFjord-100.

The model results from the TrFjord-500 simulation for 26 March 2002 is interpolated from the coarse 500 m grid to the high-resolution 100 m grid of TrFjord-100 (Figure 6.1). The interpolation has been performed in Matlab using the function *griddata* with triangle-based cubic interpolation. The TrFjord-100 configuration is then run for approximately 1 month.

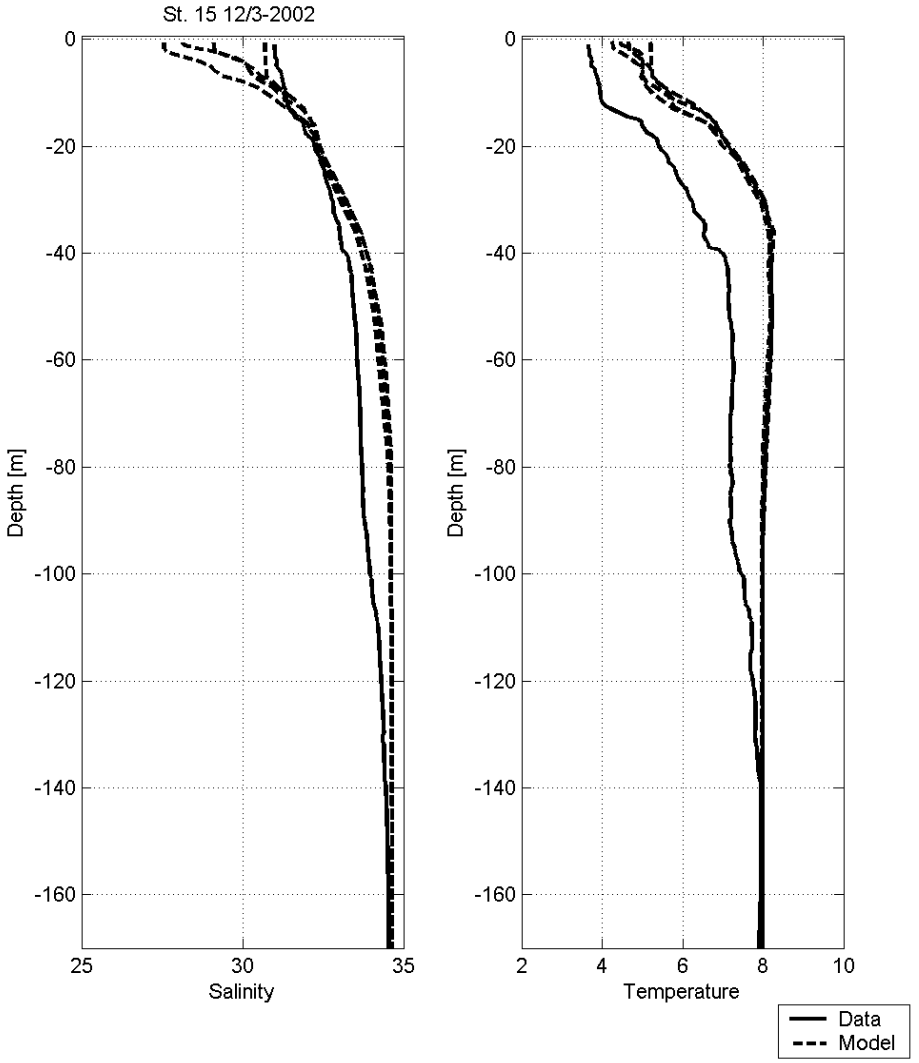

Figure 6.4 Vertical profiles of salinity and temperature at Station 15, located outside Rødberg. The dashed lines are obtained from simulations and the solid line shows field data. See text for further discussion.

6.4 Results for April 2002

The results presented below are from the simulation using the TrFjord-100 configuration.

Internal tides

The phase and amplitude of the internal tide are calculated based on the depth of the 33 isohaline for 12 April 2002, and are shown in Figure 6.5. The phase in Figure 6.5 b) reveals an amphidromic system including at least three amphidromes in the Seaward Basin. One amphidrome is located just outside Viggja. Another amphidrome is located in Flakk Fjord and a third one near the shore just east of Trondheim. Along the northern shore of the Seaward Basin, between the two amphidromes, the largest amplitude of the internal tide is found with values up to 15 m. The phase increases in both directions from the Tautra Sill. This indicates that internal Kelvin waves are generated in both directions at the sill.

In the Orkdal Fjord, the amplitudes increase from nearly zero near the outlet and to around 12 m at the head of the fjord, characteristic for wave resonance.

The internal wave speed is estimared to be $c_f^{33} \approx 0.56 \text{ m s}^{-1}$, close to the phase velocity of the internal tide studied in Chapter 5. The amplitudes of the internal tide in Gaulosen is comparatively small with amplitudes of 1-5 m.

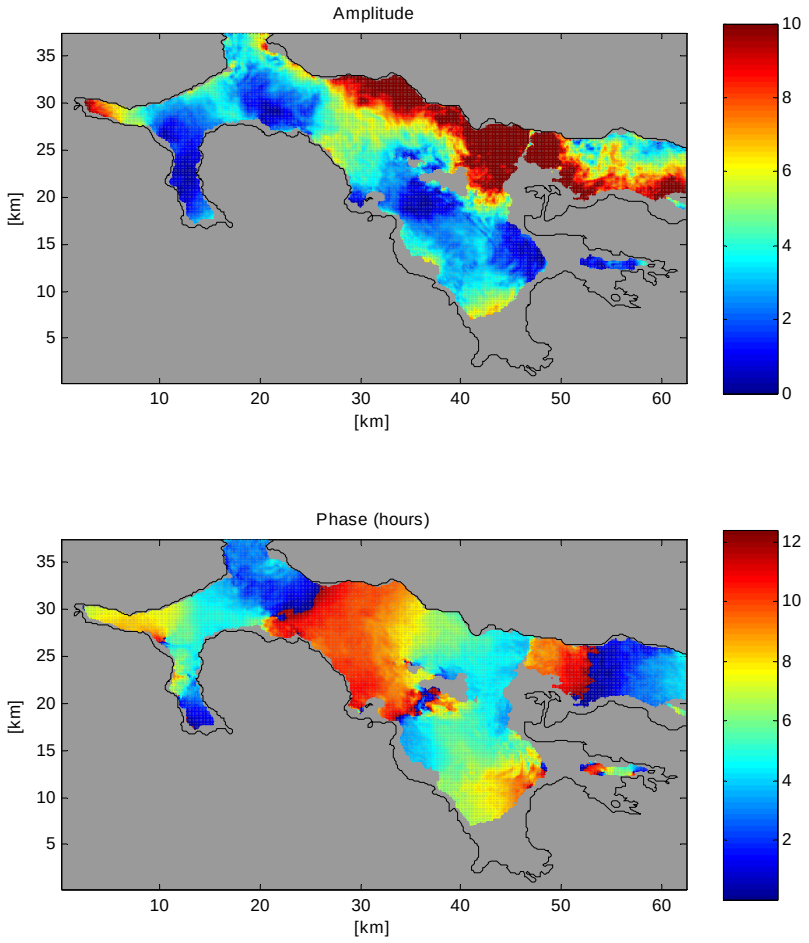

Figure 6.5 The amplitude and phase of internal tides in the Seaward Basin based on Fourier analysis of the depth of the S = 33 isohaline.

Interaction between the Orkla River Plume and the internal tides

The resonance of the internal Kelvin wave in the Orkdal Fjord results in enhanced currents in the relatively shallow surface layer. An internal gravity wave itself causes no total transport, but it influences the thin layer of fresh water in the surface. Due to the discharge from the Orkla River, the surface flow is normally directed out of the Orkdal Fjord. As the crest of the internal wave propagates into the fjord, however, and amplifies due to resonance, the surface currents associated with the wave prevent outflow of freshwater from the fjord. A snap shot of this situation is given in Figure 6.6 d). The accumulation of freshwater in the Orkdal Fjord thus starts right after surface high tide and continues until low water is reached. This pattern is also reflected in Figure 6.7 b) which shows the transport of the surface layer across Section B, i.e. the transport above the isohaline defined by S = 22. The dashed line in the same plot shows the mean transport during one tidal period. The transport across the section is larger than the amount of discharged river water, (Figure 6.2), which is expected since the plume entrains ambient water on its way outward. There are also waves of shorter wavelengths propagating into the fjord. The calculated transport seems also to be altered by these waves.

Another process that may result in variability of the transport is the anticyclonic circulation in the region. The plume-internal tide interaction seems to result in an actually stronger anticyclonic circulation. This circulation is initially formed as the Coriolis force acts on the buoyant outflow from the Orkla River, as discussed in the previous chapters. During ebb tides the plume velocity is at its strongest, since the river cross sectional area is at a minimum, which then may cause additional intensification of the anticyclonic circulation. The correlation between large river outflow velocity and strong anticyclonic circulation is found by Fong (1998) and is also confirmed by similar tests performed with NCOM for the idealized basin presented in Chapter 4. A strong backwater that re-circulates some of the ORP water was observed in May 1977 when an extensive field survey was conducted in the Orkdal Fjord to map the influence of the Orkla river discharge on the local fjord environment (McClimans, 1979). The

anticyclonic circulation was attributed to the effect of the rotation of the earth on the buoyant jet of freshwater issuing from the Orkla River. This effect was studied further in a series of laboratory experiments with river plumes in a rotating basin (McClimans, 1980). Simulations presented in the present chapter and in the previous two chapters further confirm the formation of anticyclonic circulation as a consequence of background rotation. The results presented here do, however, show that this circulation may be enhanced by the local effect of the internal tide in the fjord.

As the tide starts to rise again the accumulated freshwater in the Orkdal Fjord is released. The pile up of freshwater results in an energetic outflow, first toward Gaulosen (Figure 6.6 b)) and then along the western side of the Cross Fjord, (Figure 6.6 c)).

The surface velocities associated with internal waves seem to be comparable with the plume velocities, i.e. around 0.1-0.3 m s^{-1}. The internal tide causes a periodic lock up of potential energy in the Orkdal Fjord and a strong outflow is formed when this energy is released. This flow in turn affects the outflow conditions from Gaulosen. The internal tide thus changes the character of the freshwater outflow from the area and may accordingly be of importance for the way the plumes mix with ambient fjord.

As the buoyant water flows out of the Orkdal Fjord, it forms frontal boundaries toward the ambient waters that have a relatively strong convergence and enhanced mixing. A stronger convergence at the frontal boundary between the two plumes is further observed as the ORP water flows into the western part of the Cross Fjord. The fronts weaken again when the freshwater flow from the Orkdal Fjord reduces. These results might explain why the convergence associated with freshwater fronts in the area is not permanent, but is observed to occur suddenly and then vanish again 1 or 2 hours later. This was observed both 10 and 12 April 2002 for fronts observed in the Cross Fjord. The salinity in the area was measured through two days in 1975. A plot of the salinity distribution at different stages of the tide is presented in Chapter 2. This figure also shows that the outflow from the Orkdal Fjord is not continuous but changes during the tidal period.

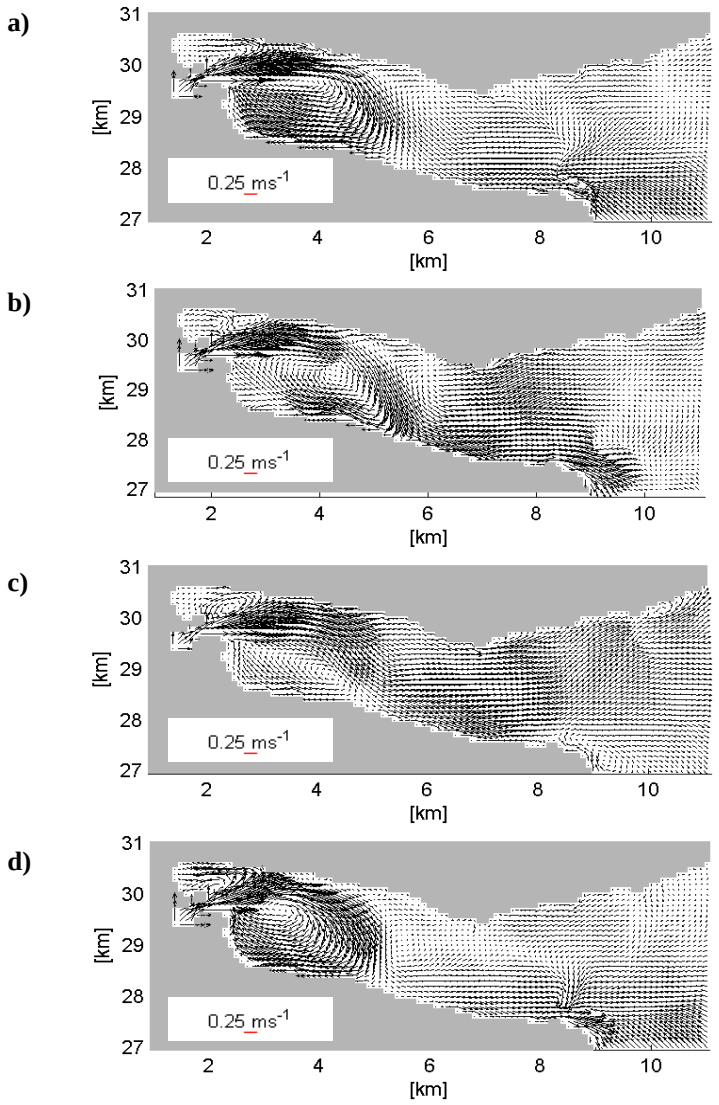

Figure 6.6 The surface currents in the Orkdal Fjord during one tidal cycle 12 April 2002. The currents are shown for internal **a)** rising tides (06:00), **b**) flood (09:00), **c)** falling tides (11:00), and **d)** ebb (14:00).

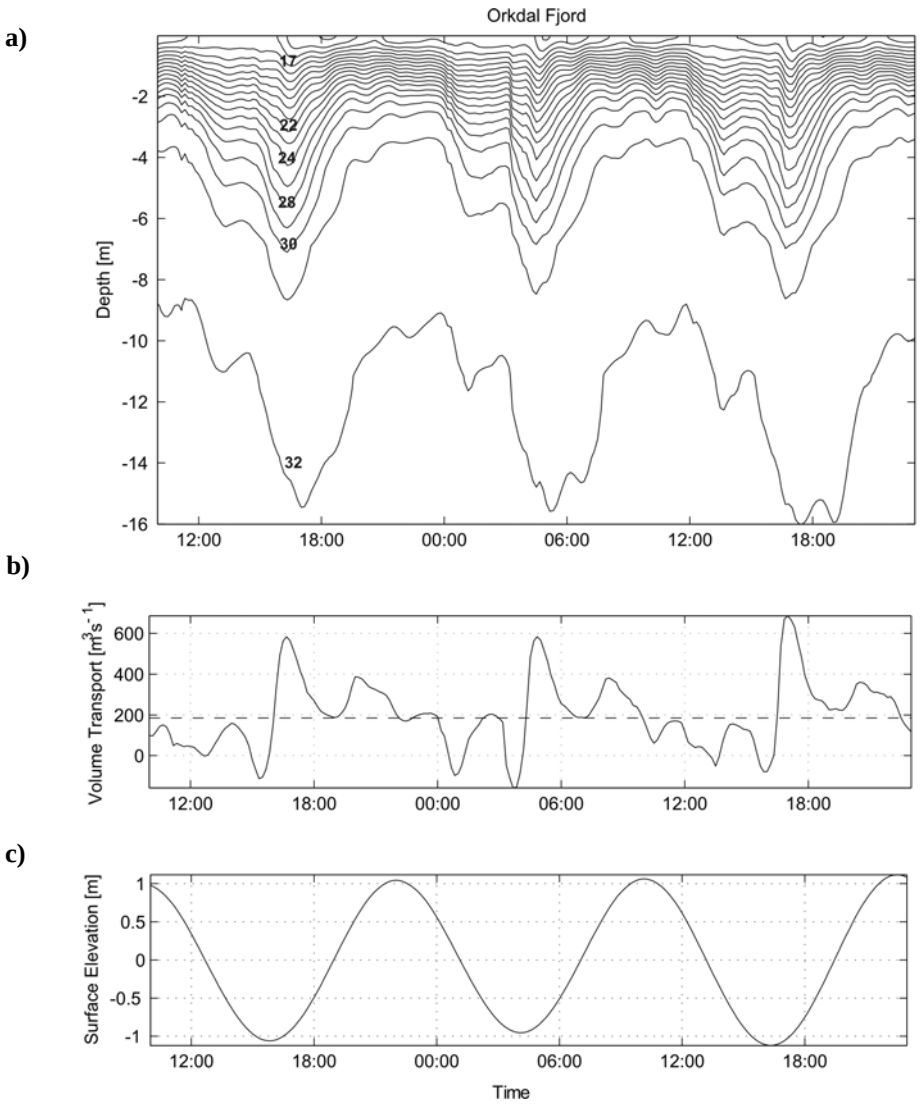

Figure 6.7 a) The vertical distribution of salinity is shown for a 36 h period for a location in the middle of Section B (Figure 5.3) in the Orkdal Fjord in **a)**. In **b)** the volume transport across Section B and above the isohaline defined by S = 22 is shown. The dashed line shows the mean transport calculated over one tidal period. In **c)** the surface elevation is shown for comparison.

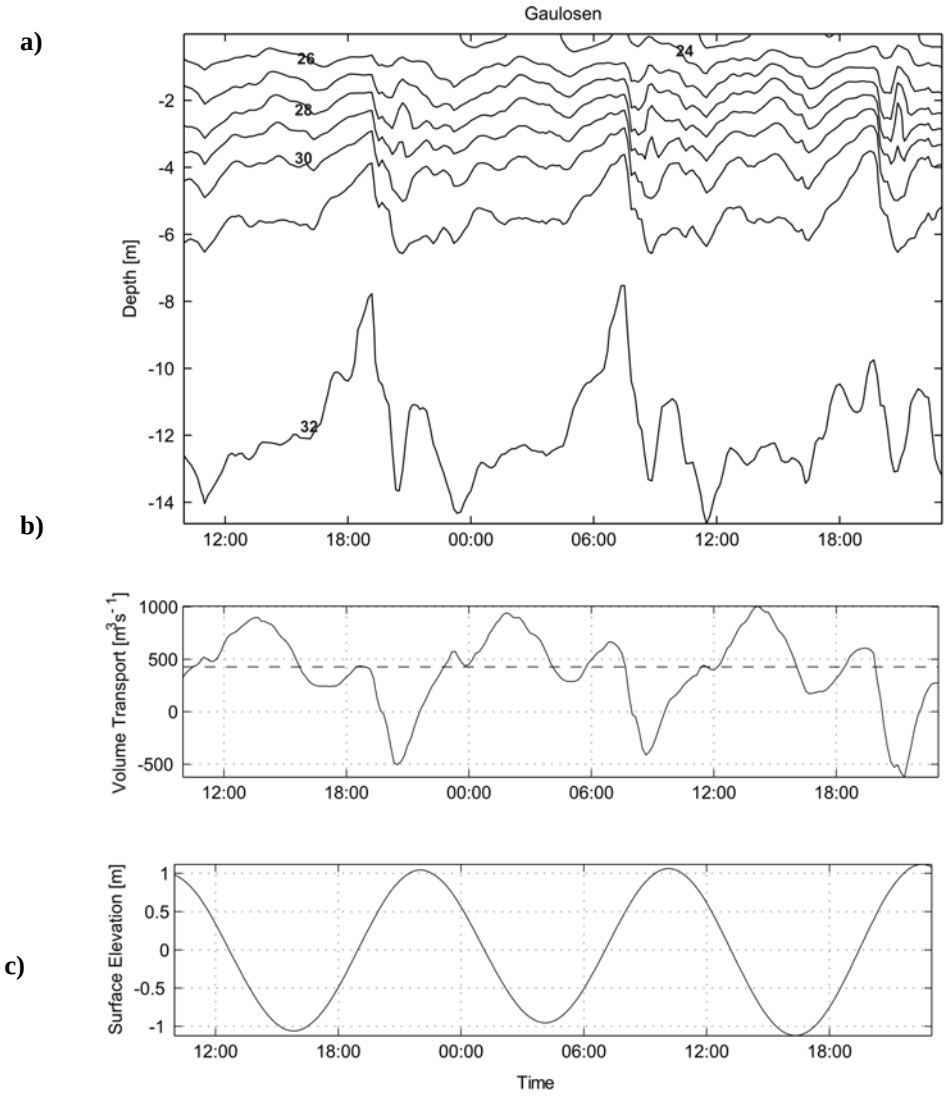

Figure 6.8 a) The vertical distribution of salinity is shown for a 36 h period for a location in the middle of Section C (Figure 5.3) in Gaulosen. In **b)** the volume transport across Section C and above the isohaline defined by S = 26 is shown. The dashed line shows the mean transport calculated over one tidal period. In **c)** the surface elevation is shown for comparison.

URN:NBN:no-3496

Interaction between the Orkla River Plume and the Gaula River Plume

Figure 6.8 a) shows the internal wave activity in Gaulosen. The internal tide in Gaulosen has a small amplitude compared to the standing wave in the Orkdal Fjord in Figure 6.7 a). There is, however, an internal wave of shorter wavelength occurring each tidal cycle. This wave is generated when GRP and ORP collide. In the previous chapters we have seen that such a collision may lead to the generation of internal bores travelling away in both directions from the collision line, and which further mixes the water of the plumes with the more saline and warmer water below. The internal bore-like wave seen in Figure 6.8 seems to be generated in a similar manner. The associated surface convergence is relatively strong, about -0.002 s^{-1} at the largest, and influences the GRP as it passes. There is also an indication of an internal wave propagating in the other direction towards the Orkdal Fjord after the collision, but this wave is short-lived.

The volume flux above the isohaline, S = 26, across Section C in Gaulosen is shown in Figure 6.8 b). Generally, the outflow is larger than the mean during falling tides and vice versa during rising tides. There is a variability during rising tides, though, where the flux increases and then decreases again during a short period of approximately 1 h. This event seems to be related to the passing of the internal bore explained above, and demonstrates the effect of surface currents related to internal waves.

After the collision, the ORP is observed to intrude into Gaulosen. The GRP is thus partly forced back into Gaulosen along its southern shore, and partly toward Byneset where a thin part of the plume still manages to flow out of the fjord.

A cyclonic eddy develops along the southern side of the GRP, as is seen in the snap-shots presented in Figure 6.10. The eddy is formed from a baroclinic instability that is initiated as a tongue of ORP water intrudes into the GRP. The energetic eddy then develops at the boundary separating the two water masses, (Figure 6.10). ORP water is entrained into the eddy and forms a spiral towards the centre. It has a character similar to that of the spiral eddies studied in Chapter 5 with associated strong belts of convergence and vorticity, and similar to the spiral eddies studied by Eldevik and Dysthe (2002). The eddy advects with the flow into the Cross Fjord, where it

eventually weakens and disappears. The whole process repeats itself each tidal cycle.

The greatest velocities in the fjord are generally found in the buoyant upper layer, the exceptions are in contractions where the depth or the width of the fjord gives rise to large velocities associated with the barotropic tidal currents. Jacobson (1977) commented that the vertical influence of the discharged freshwater from the rivers reaches 5-10 m during flood, and 15 – 20 m during ebb. Below this depth the currents are weaker and tidally dominated. In Gaulosen a similar pattern is found for the v-velocity (Figure 6.9). The plot shows how the flow is directed out of the fjord except for a short period of inflow in connection with the internal bore described above. During falling tides the influence of the buoyant upper layer and associated velocities is found to reach to about 10 m depth. As the tides rise, the similar depth is found to be less than 5 m. These depths are smaller than those given by Jacobson. Intuitively, these will change according to the amount of discharged river water and also with the distance away from the river mouth since the plume thickens due to mixing as it flows away. Below 10 m, the weaker velocities correlate well with falling and rising barotropic tides, a correlation which is also found for the flow in the Orkdal Fjord. Jacobson did not suggest a mechanism to explain why the vertical influence of the river water varied with the tides, but my work implies a relation to the internal tide.

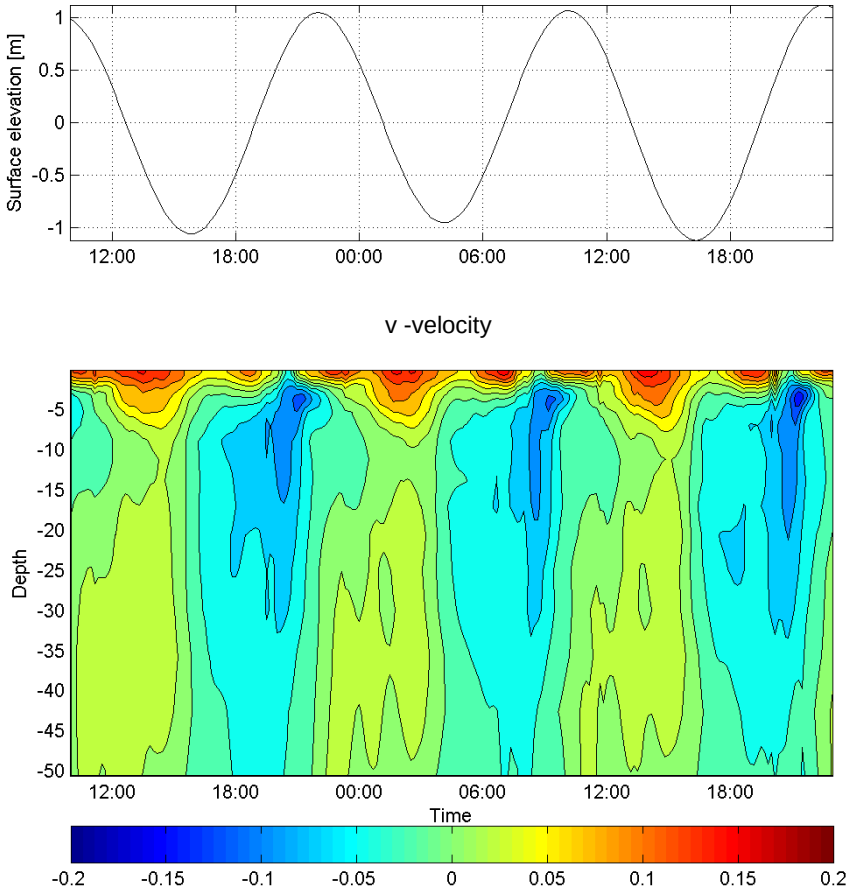

Figure 6.9 The surface elevation (upper plot), and the v-velocity (m s^{-1}) at a location in the middle of Section C, plotted against time and depth. Positive values indicate flow out of Gaulosen, while negative values display flow into the fjord.

The Cross Fjord

The surface temperature of the Seaward Basin is displayed in Figure 6.10 a). The coldest water is found near the rivers where cold water is discharged into the fjord. The water becomes warmer farther away from the river mouths. As we have seen in chapters 4 and 5, water below is mixed into river plumes in the part of the plume that separates the jet dominated flow from the subcritical flow farther downstream. The fresh and in this case cold water discharged, is therefore mixed vertically with more saline and warmer water from below. The simulated surface water is stratified where both temperature and salinity increase with depth. The surface is further heated due to the relatively high air temperatures in addition to solar radiation.

Surface currents associated with the internal tide also influence the interaction between the ORP and GRP in the Cross Fjord. The effect is local, but the currents in the Cross Fjord are naturally also greatly influenced by the periodic variation of the freshwater outflow from the Orkdal Fjord.

As the tide starts to rise, the internal tide induces in the western part of the Cross Fjord surface currents that are directed toward the Orkdal Fjord. At the same time, the outflow of ORP water starts. The latter flow is consequently initially steered toward Gaulosen. As time progresses, the relatively fresh ORP also flows along the west side of the Cross Fjord. The force of this water pushes Gaula water toward Byneset to the eastern side of the Cross Fjord (Figure 6.11). As the buoyant outflow from the Orkdal Fjord reduces, the outflow from Gaulosen enhances and pushes the ORP into a thicker plume constrained by the coast on the western side of the Cross Fjord. During this period, the vertical temperature distribution in Figure 6.11 suggests a vertical overturning at 4-8 m depth beneath the GRP. Beneath the outflow of the GRP water near the surface, however, a return flow is observed that transports a band of colder water along the eastern shore of the Cross Fjord. It is this band that is seen in Figure 6.11 between 6 and 8 m depth.

When the background rotation was introduced in the previous chapter we saw that the plumes were deflected to the right and formed coastal trapped currents. When tides were included, the flow became more complex. The GRP is characteristically thicker in the eastern part of the Cross Fjord. Otherwise, the periodic outflow of freshwater from the Gaulosen and the

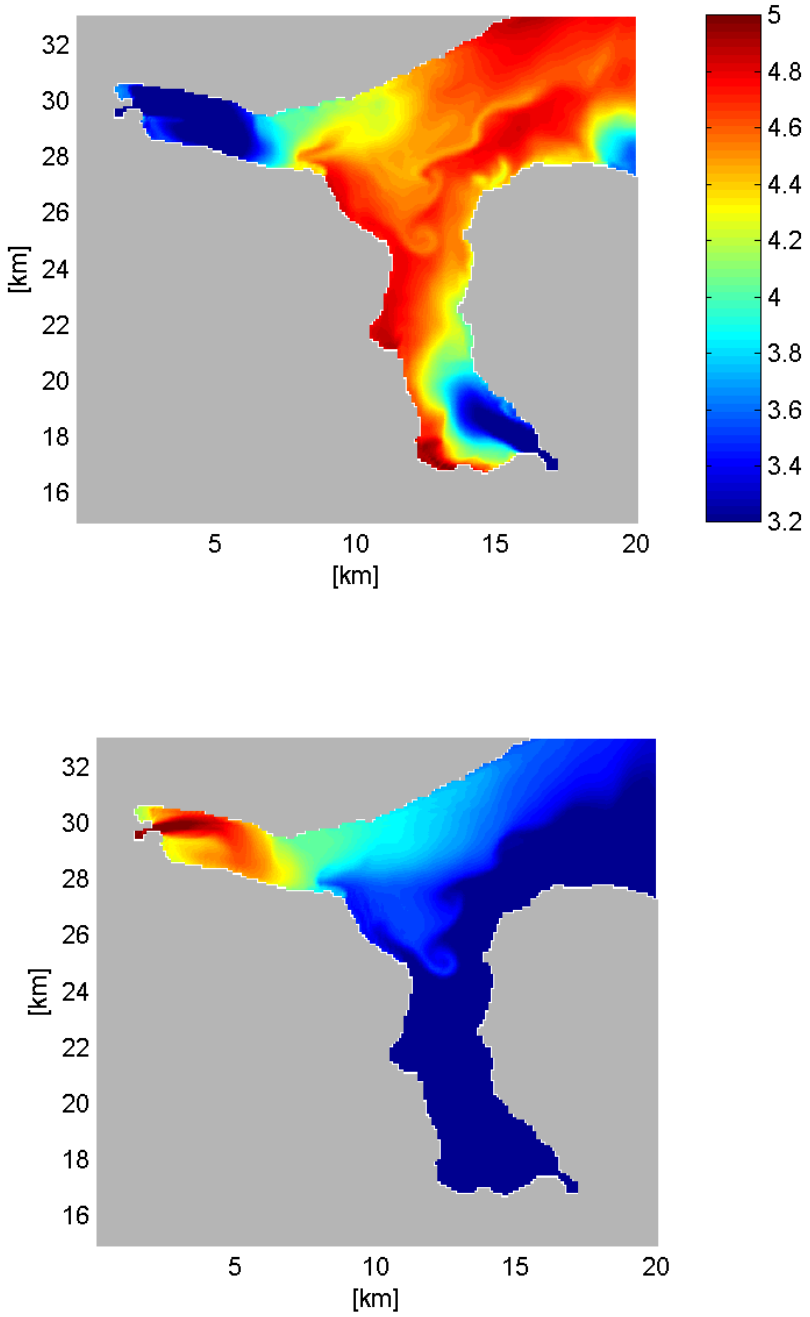

Figure 6.10 The surface temperature (^{o}C) **a)** and the surface distribution of a passive tracer applied to the discharged Orkla water, **b)**. The snapshot is taken 2:00 at 12 April 2002.

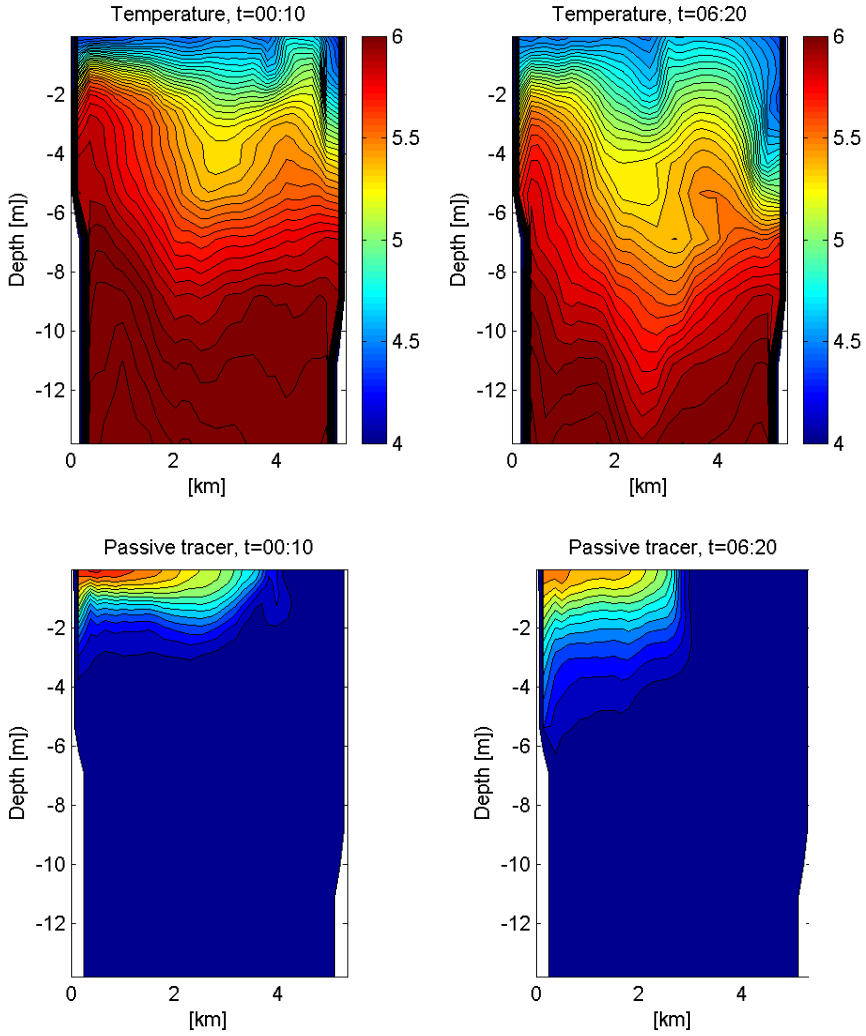

Figure 6.11 Vertical sections of temperature (upper panel) and a passive tracer (lower panel) along Section A in the Cross Fjord.

URN:NBN:no-3496

Orkdal Fjord seems to prevent a further geostrophic adjustment of the plumes.

The Seaward Basin

The initial field of temperature, as it was reproduced from TrFjord-500, shows a generally higher temperature in the Orkdal Fjord, Gaulosen and the Cross Fjord than in the rest of the Seaward Basin. TrFjord-500 is run with a uniform wind stress. The mean direction of wind speeds greater than 5 m s^{-1}, calculated for the last month before running the TrFjord-100 configuration, is from the east. The warmer water along the southern shore may therefore be due to wind induced upwelling of warmer water found at greater depths.

The coldest water, between 2 (minimum) and 3 ^{o}C is found in association with the four rivers entering the Seaward Basin: Orkla, Gaula, Nidelva and Stjørdalselva, (Figure 6.12 a)). The Åsen Fjord also has temperatures within this range. There is an intrusion of warmer water at the southern shore of this fjord. This is water in the Stjørdal River Plume (SRP) that is warmer due to vertical mixing. The generally low temperatures found in the Åsen Fjord indicate that this is a quite calm part of the fjord. This is confirmed by studying the simulated currents.

Warmer water is further observed to flow in from Agdenes and into the northern side of the Flakk Fjord, Figure 6.12 a). The generally warmer surface water in the Cross Fjord is due to vertical mixing of warmer water below as the river plumes propagate through the area. The water entrained is warmer than other parts of the fjord at the same depth, as already discussed. There is, however, an indication of an inflow of warmer water from Agdenes in the northwestern part of the Cross Fjord.

The surface distribution of a passive tracer used to track water of Orkla River origin is given in Figure 6.12 c). The passive tracer was implemented for Orkla at the start of the TrFjord-100 simulations on March 26 2002. It shows that the ORP flows trough the Cross Fjord along its western shore, and then forms two branches. One is directed out toward Agdenes and the other is directed eastward along the shore of Fosen. There is a tidal flushing of the water of Orkla origin in and out of the channel connecting the Seaward Basin with the ocean outside. As the water flushes back and forth it is mixed with

warmer water in the channel. Part of this warm water flows into the Seaward Basin, as seen from the surface distribution of temperature (Figure 6.12). This contradicts the surface current maps of Jacobson (1977; 1983). He describes a cyclonic current pattern throughout the tidal cycle. The simulations presented above show an inflow along the northern side. Jacobson, however, includes an outflow from the Cross Fjord toward Agdenes, during ebb, consistent with the model results.

As the water of Orkla origin reaches the Strind Fjord it is mixed and distributed over a relatively large area. Important mixing agents in this area are eddies. These eddies are generated as the tidal flow interacts with topography. They are found close to the shore, as described in Jacobson, (1977; 1983). Farther away from the shore in the Strind Fjord there are two cyclonic eddies. These are frontal spiral eddies of the type discussed in Chapter 5. A cyclonic gyre is located over Midtfjordsgrunna (Figure 6.12). It is associated with bands of convergence that wind up in a spiraling fashion towards the center of the gyre. The gyre is visible in the temperature field as spiraling bands of lower temperature. The cyclonic circulation over Midtfjordsgrunna is already observed on 6 April 2002, and is more or less persistent, even though the strength, area of circulation and location change slightly during the tidal cycle. The gyre seems to be initiated by the interaction of the NRP and SRP and is found only in the upper fresh layer, similar to the cyclonic eddies generated at the frontal boundary. The SRP prevents the NRP from propagating eastward along the shore and it is therefore forced northward toward Tautra. The gyre is further forced by tides.. The tidal currents in this area are strong due to the topographic contraction at the Tautra sill, both vertically and horizontall.

Water of Orkla origin is also seen in Figure 6.12 b) to be entrained into the gyre. I use the term gyre for this cyclonic circulation since it is dominating the eastern part of the Seaward Basin and it seems to be more or less a permanent feature of the flow there. A similar circulation in the area is described also by Jacobson (1977; 1983). He also includes another gyre in the western part of the basin during rising tide, but this is not seen in the simulations.

The NRP turns from an eastward to a westward direction during one tidal period. There is a correlation with the rising and falling tides, but there is a

a)

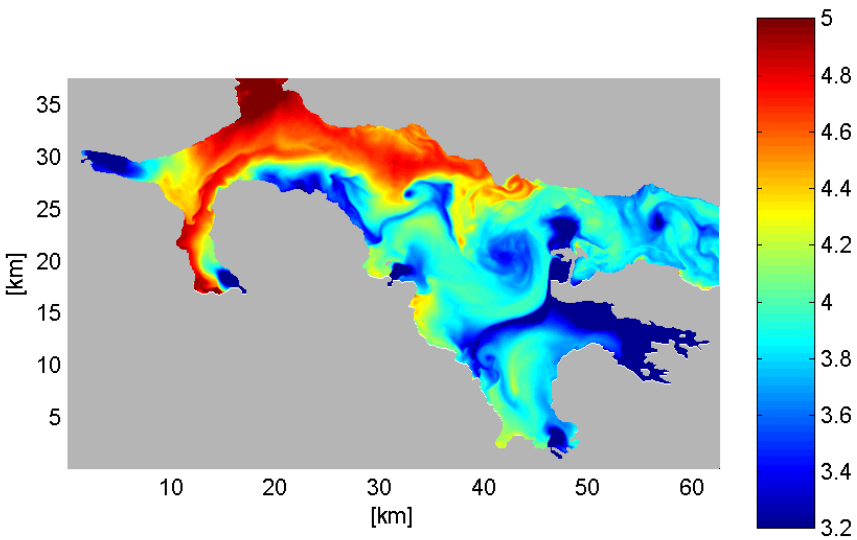

b)

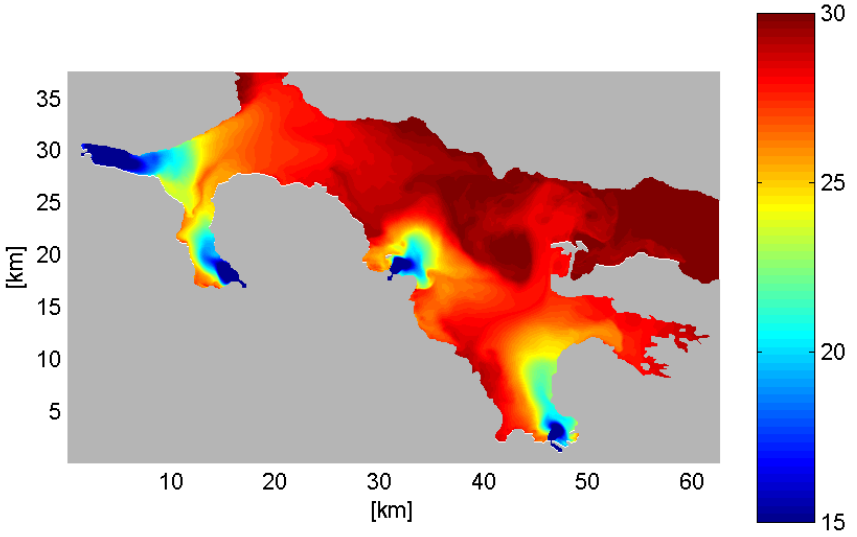

c)

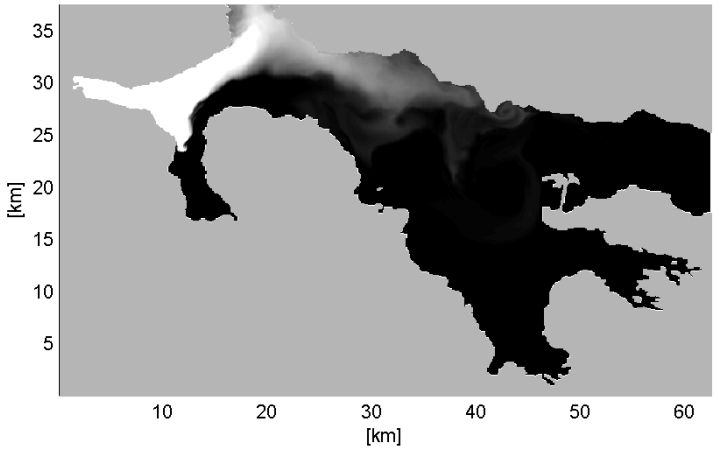

Figure 6.12 The surface distribution of **a)** temperature (^{o}C), **b)** salinity and **c)** a passive tracer (Relative scale), 00:00 am 12 April 2002.

lag with regard to maximum tidal currents. This lag seems to be due to an interaction by internal tides that influence the local currents as they propagate along the shore. In general, the surface flow in the basin is dominated by internal wave activity and by horizontal density gradients. The internal Kelvin wave has already been discussed at several times, but the convergence and divergence regions associated with shorter wavelengths are also distinct features of the surface currents. The currents in the Seaward Basin are otherwise dominated by the sharp frontal boundaries attributed to the freshwater discharges into the basin.

6.5 Summary

The results from the April 2002 simulations show that freshwater fronts, spiral eddies and internal waves are ubiquitous features of the surface waters in the Trondheim Fjord, as discussed in Chapter 5 based on more simplified simulations. For this spring situation with moderate freshwater run off, the interaction between stratification and the tide across the Tautra Sill generates an internal tide that is important for the freshwater transport in the surface layer and which also affects the interaction between the different river plumes in the Seaward Basin. It would be interesting to have similar results from the rest of the year but this is still too expensive computationally. To run the TrFjord-100 simulation for 1 month took about a third of this in real time on 16 processors at the SGI Origin 3800L machine at NTNU and required approximately 4000 CPU h. The amount of data produced are also enormous. One sample containing essential information about currents and hydrography from the whole fjord is approximately 0.5 GB.

In view of the April 2002 simulations, I obtained a new understanding of the earlier measurements. Jacobson (1977) describes observations where he shows that the hydrographic situation in the Cross Fjord, Gaulosen and the Orkdal Fjord varies greatly during a tidal cycle. He further points out that the depth of freshwater influence is different during rising tides and falling tides. This is consistent with the internal tides simulated in TrFjord-100. Eddies are also observed in the area at different places at different stages of the tidal cycle. There are discrepancies between the surface current maps presented by Jacobson and the results presented here. This is to be expected. The surface maps of Jacobson are based on measurements widely spread in time and space. The physics of the surface layer is highly complex and depends on the size of the river discharges and vertical stratification. This situation is further complicated by wind. In a wide fjord such as the Trondheim Fjord the effect of wind stress on the fresh upper layer may be significant. This effect has not been considered here.

The simulations in this and the two previous chapters have been to some degree evaluated on the basis of previous studies. In the next chapter observations from April 2002 are presented and related to the simulations.

These will give further information on the validity of the results, and in this sense comprise a model validation.

Chapter 7

Simulated and measured bottom currents in the Trondheim Fjord

URN:NBN:no-3496

URN:NBN:no-3496

7.1 Introduction

The focus of this thesis has been on the physics of the buoyant surface layer and the NCOM model has accordingly been configured for theTrondheim Fjord with this in mind. It is therefore valuable to see how well the model reproduces currents at greater depths. In the period from January to August 2002, 16 bottom current meters were placed in Trondheimsleia and the Trondheim Fjord. Currents 5 m above seabed were measured every 10 minutes using Aandereraa RCM 7 current meters. The data are kindly provided by STATOIL ASA to be used for model validation. The locations that are relevant for this study are shown in Figure 5.3 (St. A to St. D). These have been continuously monitored during the study period of Chapter 6 and constitute a benchmark for validation. In this present chapter the current meter data are compared with model simulations.

7.2 Simulated and measured bottom currents

Figure 7.1 and Figure 7.2 display simulated and measured bottom current data for stations A to D. Station A is located in the channel connecting the Seaward Basin with the ocean outside. The currents in the area are tidally dominated, with greater velocities during falling tides than during rising tides, probably due to a local topographic effects. Maximum velocities coincide with rising and falling tides and minimum velocities are found at the tidal extremes. A high agreement is seen between data and simulation results, indicating that the model performs well regarding to barotropic tidally dominated flow and that the topography of the area is well resolved. There is a trend, though, that the model seems to slightly overestimate the currents. This may be due to the relatively large z level thickness employed in the deeper part of the fjord. The agreement between data and simulation results is good throughout the period simulated. A correlation constant is calculated and is found to vary from 0.75 to 0.88 in the period from 6 April to 14 April.

Station B is located in the deeper part of the Seaward basin. There is also a tidal dominance here. The tidal currents are weak, though, due to the greater depths and width of the Seaward Basin. The simulations produce a cyclonic residual boundary current around the basin, probably due to tidal rectification. The tidal flow is further found to be stronger into the basin

along the southern shore, and stronger out of the basin along the northern shore. The discrepancies between measured and simulated currents at Station B are found to be greater than at Station A. There are intervals where the measured data show very low velocities, less than 2 cm s^{-1} during the same periods as the model produce maximum velocities for the same location. The correlation constant is also found to vary from values near zero to negative values around –0.6. In the part of the fjord where Station B is located, tidal currents produce at times an enclosed cyclonic gyre. Lower velocities are also found in simulation results around 1 km to the north, closer to the center of the cyclonic circulation, which are more in accordance with the measurements. The discrepancies may also be explained from possible errors in the measurements. The period of nearly no currents appears to occur abruptly. This is a general trend, and not only for this particular period.

In Figure 7.2 the bottom currents for stations C and D are displayed. These two stations are located on each side of the Tautra sill at around 40 m and 190 m, respectively. The correspondence between measurements and simulations is very good for Station D, the correlation constant is found to be 0.94 ±0.04 in the period from 6 April to 14 April. As for Station A, there is a small overestimation of the currents. The good agreement between data and model results is found throughout the simulation with TrFjord-100. Considering Station D on the other hand, the model does not seem to be able to reproduce an event which occurs each tidal cycle and which produces current velocities up to 40 cm s^{-1}. This is not the greatest velocity observed for the period, the measurements of the currents at this location were as high as 70 cm s^{-1} in the beginning of April. In general, the correlation between observations and simulations varies during the period. This may be understood from the high complexity of the area where Station D is located. Internal waves of different characteristics are generated as the tides flush back and forth over the sill, as seen in chapters 5 and 6. These waves influence the local velocities and may also lift heavier water above the sill and generate density driven bottom currents that produce high velocities.

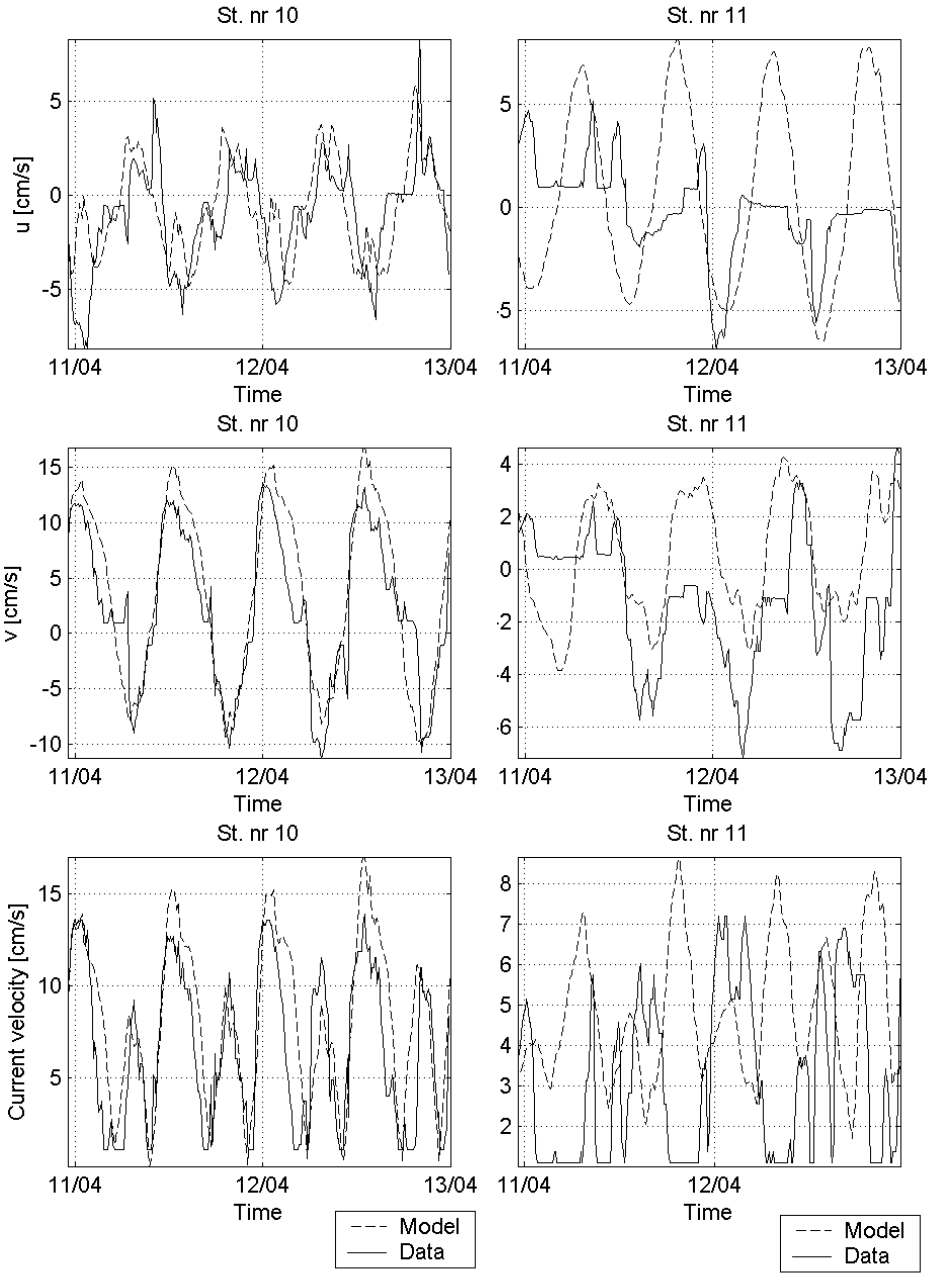

Figure 7.1 Bottom current data at around 550 m and 500 m for Station A (left) and Station B (right), respectively.

URN:NBN:no-3496

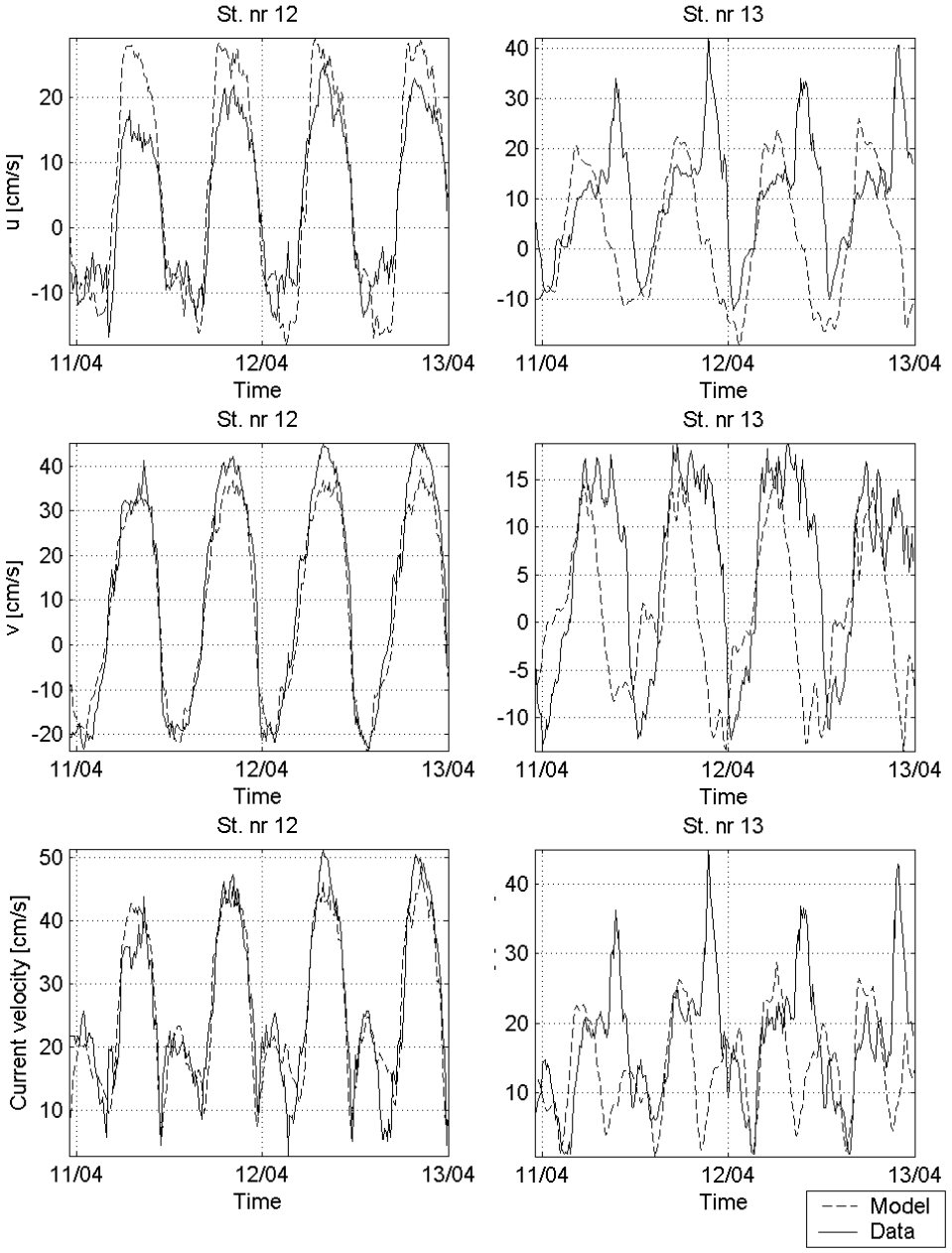

Figure 7.2 Bottom current data at around 40 m and 190 m for Station C (left) and Station D (right), respectively.

URN:NBN:no-3496

7.3 Discussion and Conclusion

Despite the relatively poor vertical resolution employed near the bottom of the Trondheim Fjord, the currents are relatively well reproduced. This is to be expected for a barotropical dominated flow at these depths. There are, however, also other physical events that may influence the currents, such as overflows of dense water across a sill separating two basins of the fjord. This seems to be the case across the Tautra sill resulting in high velocities at Station D. This is also seen from a high correlation between high velocities and high salinities at this location. This is not reproduced in the model due to its coarse vertical resolution at these depths.

The measured salinity and temperature are not included in this evaluation study. In general the variations of these are not within the resolution of the instruments measuring them, the exception is at station D where periods of denser water is seen that is not reproduced by the model. Otherwise, the salinity of the deepest layer of the fjord is about 0.5 less than measured salinity. At shallower depths the discrepancies are within 0.1 – 0.3.

The model does not account for the exchange between the Trondheim Fjord and the ocean outside, probably resulting in the deviation between simulations and data. There are a couple of events, one in March and one in June, that indicate an intrusion of denser water into the fjord replacing the deep layer. The model does not simulate events that are forced by changes in the external density field. In general though, the currents near the bottom are well reproduced by the simulations with NCOM.

URN:NBN:no-3496

Chapter 8

A qualitative model validation study based on aerial photography

Photo taken toward the head of Gaulosen. To the left in the photo the small plume formed from a creek is seen. The Gaula river plume jet is seen from increased sea surface roughness in the middle of the photo.

URN:NBN:no-3496

8.1 Introduction

Images of the sea surface may potentially be used to evaluate model results and to give further information of subsurface physics and phenomena. In this chapter I will present some aerial photos taken in the Cross Fjord area and relate these observations to simulation results.

When dealing with large sets of data as the ones produced by NCOM, it is useful to have effective ways to study the data and to visualize important features of the flow. My favorite tool in this study is the surface divergence field. This 2–D field contains information on high frequency internal waves, eddies and freshwater fronts. These all have surface signatures in the surface divergence field. This is also a property that may be utilized to document and investigate the physics of the real fjord. Freshwater fronts are associated with surface convergence that results in the accumulation of floating debris. Such fronts are further characterised by cusps pointing in toward the side containing the lightest water. These properties have been examined for instance by Cooper et al. (2001).

Internal waves are associated with both horizontal convergence and divergence at the surface that in sum do not result in accumulation. The divergence field at the surface is often visible as slick lines or as regions of increased roughness. Other features associated may also be visible, such as the spirals slicks shown in Munk, (2001). Propagating internal hydraulic jumps may also be detected as patterns at the surface.

Aerial photos in addition to images obtained from a web camera that monitored a part of the Cross Fjord from September to October 2002 showed many interesting surface expressions in the Trondheim Fjord, e.g. the photos shown in the front page of chapters 4 and 5. In this chapter the focus will be on April 2002. Aerial photos from this period, at different locations in the fjord, showed structures that were difficult to interpret. Only after performing the high-resolution simulations did I discover possible explanations for these observations. These also give information on how well the model reproduces important physical processes in the area.

At the end of the chapter a particular aerial observation is included from October 2000, when a structure was observed in the Cross Fjord that

consisted of two lines that formed a cross. This pattern is reproduced in simulations performed with NCOM.

8.2 Results

Spiral eddies

Two aerial photos from 6 April 2002 are shown in Figure 8.1. The photos are adjusted using Local equalization in Corel Photo Paint. This makes the structures more visible. The structure seen in Figure 8.1 appears to be related to surface convergence; e.g. the accumulation of foam is seen in the original photo. The two bands of convergence wind up cyclonically towards a common center. This is a similar shape of convergence line as reproduced by simulations for the initial phase of spiral eddy development. Simulated surface currents for 08:00 and 09:00 on 6 April 2002, close to the time the photo was taken, are shown in Figure 8.2. The simulated cyclonic eddy is located further south, approximately 1 km or so, compared to the photo in Figure 8.1. This eddy is, as we have seen in Chapter 6 for 12 April 2002, generated as a consequence of baroclinic instability that grow along front separating the ORP and GRP water. The eddy seen in Figure 8.2 merges at an earlier point with a similar feature issuing from Børsa. This is not observed in the simulation for 12 April 2002. The conditions on 6 April are slightly different. During this period, the Gaula discharge is larger than the Orkla discharge. The eddy is accordingly generated further out from Gaulosen. It then propagates into Gaulosen before continuing out the Cross Fjord, again following the flow of relatively fresh water of the GRP. Unfortunately, there are no data to give us further information on this eddy structure, and we do not have any more photos from the same area at the same stage of the tidal cycle. The latter would have given further information on whether there is an eddy generated during each tidal cycle as suggested by the model results. Aerial photos were taken the next day were taken at a later stage of the tides. There is, however, an indication of a spiral eddy structure further out in the Cross Fjord that day. This is observed from spiral slick structures.

A cyclonic eddy occurring during rising tides is included in the surface current maps by Jacobson (1977; 1983), as mentioned in Chapter 6. The salinity found in association with this eddy, though, is much lower than the

surrounding water, with differences up to 10 at 1 m depth. The simulation produces an eddy that accumulates at its centre the more saline water located between the two plumes where the plume has not yet occluded. Slightly fresher and colder water, however, is accumulated along the convergence lines spinning up the eddy.

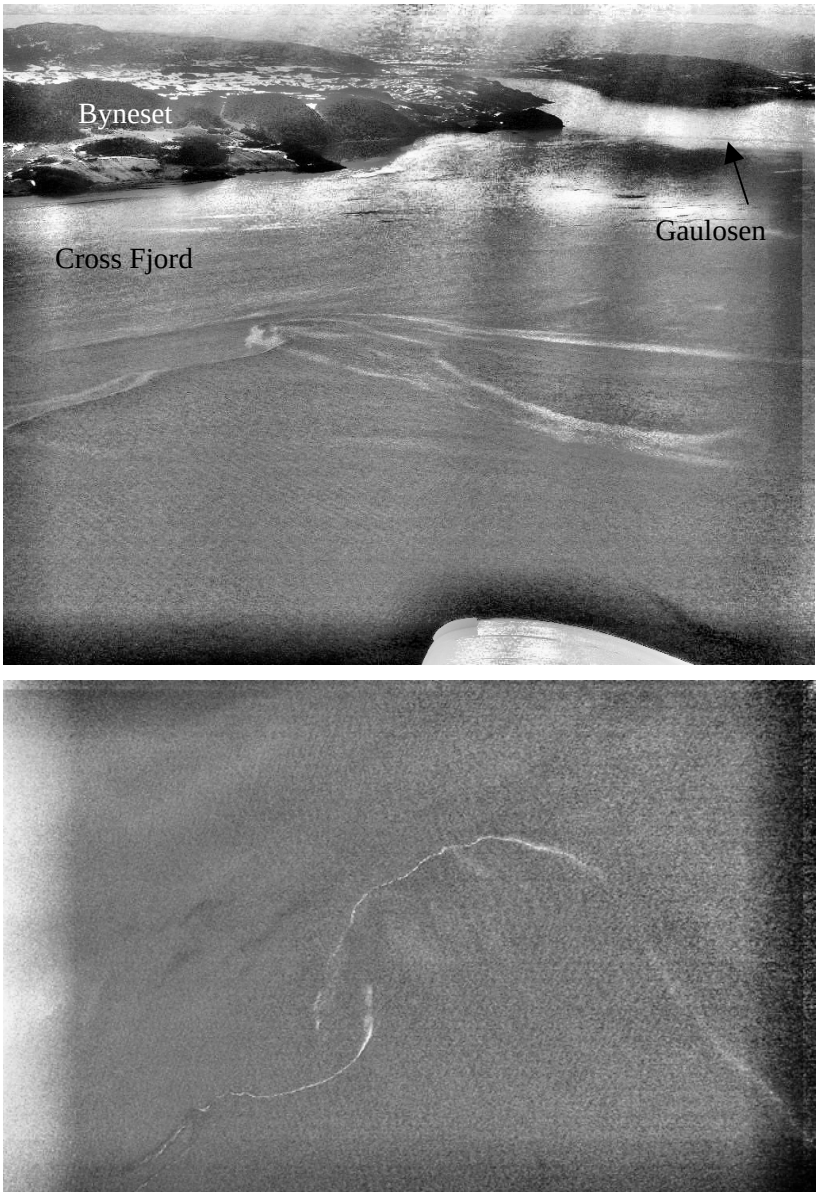

Figure 8.1 The upper photo is taken on 6 April 2002 between 8:00 h and 9:00 h with the camera view toward the head of Gaulosen and from the Cross Fjord. The southwestern part of Byneset is seen to the left in the photo. The lower photo is a close up of the structure seen in the middle of the upper photo and is taken a few minutes later.

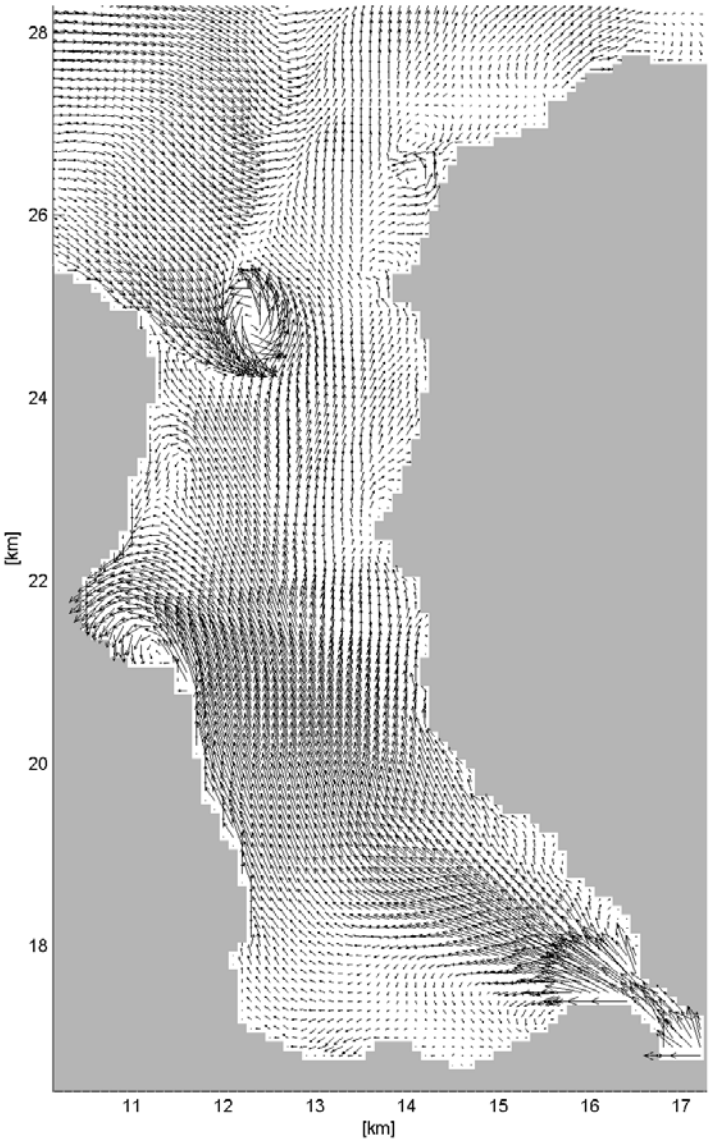

Figure 8.2 Simulated surface currents 6 April 2002 at t = 8:00 h, approximately a half to one hour before the time of the photos shown in Figure 8.1.

Internal bore in Gaulosen

Another aerial photography taken around 08:00-09:00 h on 6 April 2002, in Gaulosen is shown in Figure 8.3. The surface water in the fjord is dark brown. The Gaula water brings a lot of humus into the area giving the GRP this colour. There are smaller creeks, located around the shore of Gaulosen, that supply the area with negligible amounts of fresh water. This water, however, sometime brings mud that has a brighter colour than the Gaula water and acts as a surface current tracer in the system. (Such a fresh layer was found floating on top of the Gaula water). It is most likely traces of this water that is seen accumulating near the line crossing Gaulosen seen in Figure 8.3. Bits of ice are also seen as white spots and which may also be used to trace the surface current patterns. The line seen in Figure 8.3 is quite smooth. There is no trace of cusps and troughs that are characteristic of freshwater fronts. It crosses the fjord in a more or less straight line, except the part that deflects inward on the northeast side of the fjord. There seems to be some convergence along the line, enough to accumulate the muddy water floating at the top, even though it is partly spread behind to the right of the line. The bits of ice are also more dispersed in the area. Since this was a rather calm day, wind effects are not considered to be of importance. One explanation is that the duration of the convergence is too short to accumulate pieces of ice that are spread over a relatively large area.

An alternative explanation of the above is that the convergence line is only passing, and accumulates only nearby floating material. Internal waves are associated by both convergence and divergence, but which in time prevents an accumulation at a given location. The structure may be the signature of an internal bore. One type of bore has only one convergence line at the head of a rotor. There is only one convergence line detected from the photos taken the same day. The simulation results support this explanation. As seen in Chapter 6 an internal wave of soliton character is generated in connection with the collision between GRP and ORP This was observed on 12 April 2002, but the same is the case on 6 April 2002. The two convergence lines related to this wave leaves signatures in the surface currents as seen in Figure 8.3. There is further an indication in the simulation of a deflection of the front on the northeastern side of the fjord, as seen from the photo.

Figure 8.3 Photo from Gaulosen taken on 6 April 2002 between 08:00 h and 09:00 h. The lower photo is the same as the upper photo adjusted by using local equalization in Corel Photo Paint.

The Cross Fjord

Figure 8.4 shows three photos taken from Byneset and towards the other side of the fjord. The first picture is taken at 14:12 h and one slick is seen near the outlet of the Cross Fjord. A few minutes later two other photos are taken from a location farther to the south at Byneset. There seems to be a total of three slicks, marked with numbers 1 to 3, captured by the photos. Near the Byneset side of the fjord, the convergence is observed from changes in surface roughness due to the effect the divergence field has on capillary waves. Farther out, the band is seen as slicks. In the last photo the furthermost slick is observed, the convergence related to this seems to be less intense; this was also the general impression of the waves as they propagated into the fjord

Internal waves were also observed on 10 April 2002. The surface convergence associated with these waves was very strong. We put out a plastic bag and filled it with water ahead of the first convergence band. The bag was observed to be drawn into the front, then submerged and return to the surface behind the front. This rotational behaviour is typical for an internal bore, in this case an undular internal bore (A few CTD measurements at both sides of the fronts showed that this was not a freshwater front). There were three bands observed with a distance of around 200 m and waves had a speed of approximately 0.5 m s^{-1}. The surface water was boiling along the convergence lines and this was observed to be stronger for the first band and became weaker for the other two (Figure 8.5).

Convergence related freshwater fronts observed during surveys in 2002 and in 2001 were all observed to be weaker than the one observed on 10 April 2002. This may indicate that the associated vertical velocity is much stronger and the hydrostatic assumption might in this sense be even more questionable. Furthermore, these waves with wavelengths of approximately 200 m are certainly not well resolved by the model. The generation mechanism on the other hand might be.

The horizontal surface divergence field shows a complicated interference pattern of internal waves (Figure 8.7). As we have seen in chapters 5 and 6, internal waves are generated at the Tautra sill. There are also waves that propagate into the Seaward Basin from the channel connecting the Seaward

Basin with the sea outside. As the waves propagate into the basin they interact with previous waves that are reflected by the walls in the basin. By studying animations of the divergence field, waves can be tracked from the Tautra sill that then interact with waves issuing from the contraction starting at Rødberg, and then propagate as a single wave with distinct bands of convergence and divergence into the Cross Fjord. The model thus indicates that the waves observed in the Cross Fjord may be partly generated as far away as the Tautra sill. The model however is not regarded to be ideal for studying these kinds of wave phenomena. On the other hand, it may be used to produce preconditions for the wave generation, and a more suitable model may then be used to study how the waves propagate in the fjord.

Two photos of foam fronts are given in McClimans (1978). One of these is from the Orkdal Fjord and was similar to the ones in figures 8.4 and 8.5 (McClimans, personal communication). The foam accumulation along this front was explained as a wind effect. In this case the wind direction was opposite to the propagation direction of the front. Another photo of foam fronts may have a similar explanation. This photo is shown in Figure 8.6. I believe that these are internal waves or an undular internal bore that are generated at the Tautra sill, and that wind blows foam into the fronts as suggested by MCClimans (1978). This view is supported by the simulation results. The photo is also used as an example of multiple front generations related to river plumes (Simpson, 1997). This multiple front phenomena is suggested to be explained from internal waves generated when a river plume flows over a stratified ambient. As mentioned in Chapter 4, this phenomenon is observed in the Cross Fjord. It is unlikely though that the observation presented in Figure 8.6 has this explanation.

Figure 8.4 Photos taken from the west side of Byneset on 10 April 2002. The two uppermost photos are taken farther out in the Cross Fjord than the lower one. See text for further explanation.

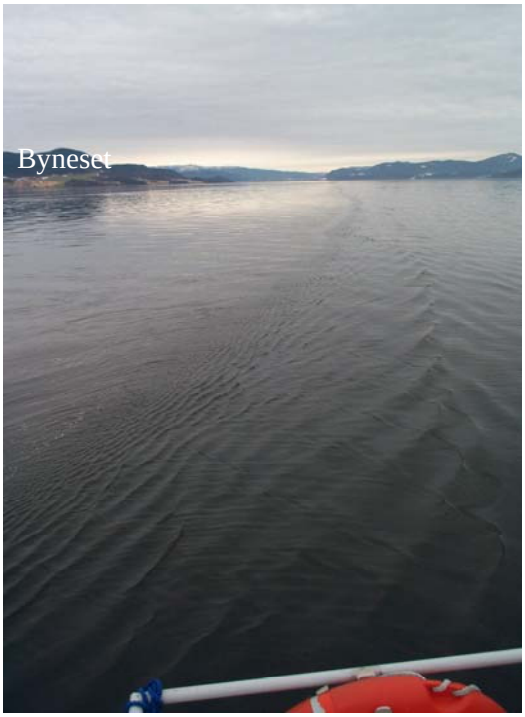

Figure 8.5 Bands of convergence observedin the Cross Fjord on 10 April 2002.

Figure 8.6 Foam fronts observed in the Flakk Fjord. The photo is taken from Byneset viewing toward Fosen.

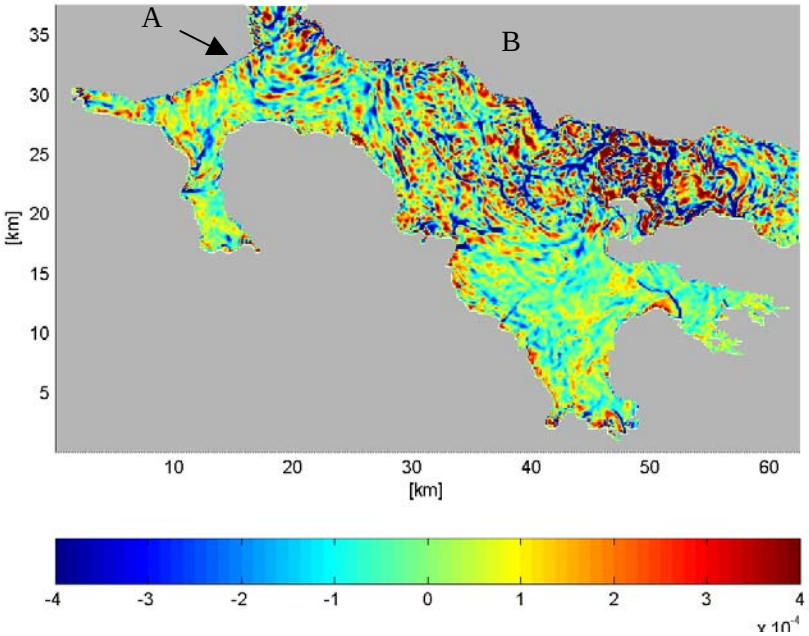

Figure 8.7 Horizontal divergence of the surface. The snap shot is taken on 10 April 2002 at t = 14:00. A: Bands of divergence and convergence associated with internal

waves propagating into the Cross Fjord. B: Bands of divergence and convergence associated with internal waves generated at the Tautra sill.

The Cross in the Cross Fjord

I will now show an observation of an unique feature from aerial photography that has been reproduced in model simulations. It consists of two crossing convergence lines. It actually resembles the shape of a cross, and it is observed in the Cross Fjord[1] (Figure 8.8 a)). The cross feature is found in the middle. A characteristic freshwater front with cusps related to the frontal boundary of the baroclinic coastal current around Byneset, can also be seen. Figure 8.8 b) shows the horizontal divergence at the surface calculated from the simulation results. There are many complex patterns of divergence and convergence that are due to wave interactions. The generation of the cross seems to be caused by the interaction between the ORP and GRP. Three of the convergence lines forming the cross are related to horizontal density fronts. The fourth line, the one in the lower left corner of the two pictures, is associated with an internal bore generated after the two currents collide. This internal bore will eventually propagate away from the area, leaving behind a y-shaped structure.

[1] The name of the Fjord is literally translated from Norwegian, i.e. it is not named after our observation

a)

b)

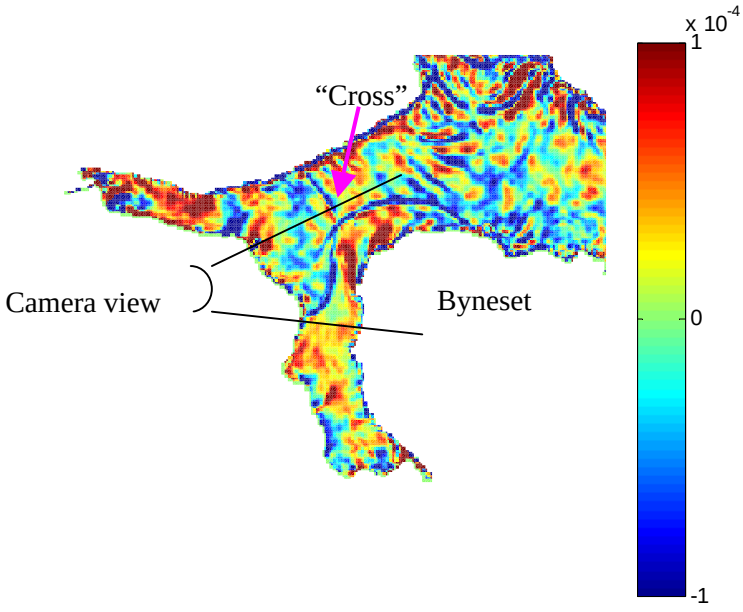

Figure 8.8 Photography from the area covering parts of the Cross Fjord. The mouth of Gaulosen is to the right. **b)** Horizontal surface divergence calculated from the simulations. The modelled cross is seen further out in the Cross Fjord than in the picture displayed in **a)**.

URN:NBN:no-3496

8.3 Summary and conclusions

Aerial photos and other types of remote imaging show many interesting surface signatures of subsurface processes and phenomena in the Trondheim Fjord. Possible explanations of these observations are suggested using the high-resolution numerical simulations of the Trondheim Fjord. The details of the simulations and images indicate that the model gives a good representation of the physics of the surface waters.

A more systematic imaging of the sea surface can give observations of processes with both a high spatial and temporal resolution. Quantitative information such as wavelength, phase and speed of internal waves may further be obtained if the photos are in addition geo-rectified. This is a relatively simple and inexpensive way of obtaining valuable information that may contribute to increasing the insight into important physical processes in a particular coastal area. The images may also be used to evaluate model results.

URN:NBN:no-3496

Chapter 9

Summary

URN:NBN:no-3496

URN:NBN:no-3496

The main focus of the research presented in this thesis has been on how freshwater discharge from rivers spreads in the Trondheim Fjord. The problem has been approached by using the Navy Coastal Ocean Model (NCOM) to perform simulations of river discharges into both idealized and more realistic environments. The study has been performed to address three main questions:

A. How does the rotation of the earth influence river plume development in the Trondheim Fjord ?

B. What happens when two different plumes meet and interact?

C. How does the tidal forcing influence the river plume behavior and development in the Trondheim Fjord?

The studies by McClimans (1979; 1980; 1983) and Eidnes (1982) showed that the rotation of the earth might significantly change the development and behavior of river plumes in Norwegian fjords. Their results were based on both field data and on simulations of river discharges into idealized basins in a rotating tank in the laboratory. The results from the laboratory modelling have been used to evaluate how well the model performs when simulating river plume development in a fjord environment. This has been a subject in Chapter 4, and a qualitative agreement was found between the two different types of modelling of river plumes. The simulations performed with NCOM thus further support the findings by McClimans and Eidnes. A river plume in a rotating basin of the scale typical for fjords deflects to the right, hits the shore and then forms a coastal trapped density driven current. This partly answers question A. Other issues that are relevant for river plume development in a fjord environment are addressed in Chapter 4; how the plume flow develops in time, how it mixes with the surrounding water and what happens when a river discharges into a stratified ambient.

In Chapter 5 the main objective was to study freshwater spread in the Trondheim Fjord. The simulations were to some degree simplified for so to

keep focus on particular processes. In this research, questions A and B were approached by performing simulations without forcing of tides. The effect of the rotation of the earth was already studied in Chapter 4, and further studied in Chapter 5 for the discharges into the Seaward Basin. The background rotation had a slightly different effect at the different river plumes due to the different local topography around the discharges. For example, the Orkla and Gaula discharge into relatively narrow arms of the Trondheim Fjord, while Nidelva discharges into the widest part of the fjord.

When two river plumes collide, internal bores are generated and the plume of highest density is forced to submerge beneath the other. These results are similar to those described by Simpson (1997) for colliding gravity currents. Another interesting result related to Question B is that eddies form at the occluded part of the front after a collision. As time progresses and the different plumes nearly cover the whole surface of the Seaward Basin, horizontal cyclonic shears developed across the fronts. The eddies formed when fronts occluded were now able to grow on the barotropic shear and are found to wind up the frontal interfaces into spirals. The cyclonic eddy, the y-shaped frontal system, and the submerging of one plume beneath the other are similar to the dynamics of the meteorological analogue of occluded fronts (see for instance Wallace and Hobbs, 1977).

Spiral eddies have been observed in a large number of images taken from space shuttles (Munk, 2000). In addition to Munk, there have been a few studies in recent years that consider these spiral eddies and discuss which mechanisms cause eddies to form in such large numbers. Eldevik and Dysthe (2002) and Shen and Evans (2002) have reproduced spiral eddies in numerical simulations of idealized cases and show how spiral eddies form from baroclinic and barotropic instabilities, respectively. The spiral eddies in the Trondheim Fjord simulations are naturally related to baroclinic processes, but the simulations also showed that barotropic shear may be important for the eddies to grow to fully developed spirals

Tides were forced to see how this influenced the surface flow in the Trondheim Fjord (Question C). During a cruise in 2001, some field observations of the hydrographic conditions in the Cross Fjord hinted that the tidal forcing greatly affected the river plume development in the area. The simulation also showed how the plumes greatly varied with the tides,

consistent with the observations. However, the model produced a surface flow that in the Orkdal Fjord that was in the opposite direction of the tidal currents. A more detailed study based on the numerical simulations showed that the flow in the area is significantly influenced by the internal tide. This is a very interesting result. It has also been used to further understand previous field observations that previously have been difficult to explain.

Subsequently, I simulated the Trondheim Fjord for a realistic situation. I chose the spring of 2002, and April in particular, for two reasons. Firstly, there were observations from the period that could be used to evaluate the model results. Secondly, this was a calm period and the problem of not having a representative wind field in the fjord was thus avioded. The model results were described in view of the processes and phenomena described in Chapter 5 and compared to relevant previous studies. Again the internal tide was shown to have a significant effect on the surface flow in the fjord. This in turn influenced the interaction between the different plumes.

In the two following chapters, the objective was to evaluate the simulation results presented in Chapter 6. Bottom current measurements were presented in Chapter 7 together with the simulated currents. Even though discrepancies were found between observations and simulations, I consider the overall agreement to be fairly good. The deep currents of the fjord are dominantly barotropic except for a few baroclinic events, such as overflows of denser water across sills. The high horizontal resolution of the Trondheim Fjord simulations thus reproduces the barotropic tidal currents well.

In Chapter 8, I used simulation results to explain surface patterns that were seen in photos of the fjord surface. Subsurface processes and phenomena were described that are likely to produce the patterns observed in the photos. The consistency found further confirms the model results, though only qualitatively.

The model results in the present thesis have been justified by comparing the results with previous observations and research in addition to newer observations. This evaluation has mainly been of a qualitative character. I find this to be adequate with regard to the main goal of the research presented, namely to identify processes and phenomena that influences the spread of freshwater in the Trondheim Fjord. In any future study with the objective to quantify the importance of the different processes, a more

quantitative validation study will be required. The research presented in this thesis can be used to plan observational programs that can give more relevant and useful data for this purpose. Another challenge is to obtain a realistic representation of wind in the fjord to study what effect this has on the fjord circulation.

References

Baines, P.G., *Topographic effects in stratified flows*, 482 pp., Cambridge University Press, 1995.

Blumberg, A.F. and G.L. Mellor, A description of a three-dimensional coastal ocean circulation model, In *Three-Dimensional Coastal Ocean Models*,(Ed. N. Heaps), American Union, New York, 208 pp. , 1987.

Britter, R.E. and J.E. Simpson, Experiments on the dynamics of a gravity current head, *Journal of Fluid Mechanics*, *88*, 223-240, 1978.

Cooper, A.L., R.P. Mied and G.J. Lindemann, Evolution of freely propagating, two-dimensional surface gravity current fronts, *Journal of Geophysical Research-Oceans*, *106* (C8), 16887-16901, 2001.

Eidnes, G., Turbulent entrainment over tetthetsgrenseflater, Hovedfagsoppgave i geofysikk, Univeristetet i Oslo, Oslo, 1982.

Eldevik, T. and K.B. Dysthe, Spiral eddies, *Journal of Physical Oceanography*, *32* (3), 851-869, 2002.

Emery, W.J. and R.E. Thomson, *Data analysis methods in physical oceanography*, 634 pp., Pergamon Press, 1998.

Fong, D.A., *Dynamics of freshwater plumes: observations and numerical modelling of the wind-forced response and alongshore freshwater transport.* Massachusetts Institute of Technology, 172 pp. 1998.

Fujiwara, T., L.P. Sanford, K. Nakatsuji and Y. Sugiyama, Anti-cyclonic circulation driven by the estuarine circulation in a gulf type ROFI, *Journal of Marine Systems*, *12* (1-4), 83-99, 1997.

Garvine, R.W., A dynamical system for classifying buoyant coastal discharges, *Continental Shelf Research*, *15* (13), 1585-1596, 1995.

Garvine, R.W., Radial spreading of buoyant surface plumes in coastal waters, *Journal of Geophysical Research*, *89* (C2), 1989-1996, 1984.

Holland, W.R., J.C. Chow and F.O. Bryan, Application of a Third-Order Upwind Scheme in the NCAR Ocean Model, *Journal of Climate*, 11(6), 1487-1493, 1998.

Jacobson, P., Resipientundersøkelse av Trondheimfjorden, River and Harbour Laboratory Report STF60 F76082, 1977.

Jacobson, P., Physical Oceanography of the Trondheimfjord, *Geophysical Astrophysical Fluid Dynamics*, *26*, 3-26, 1983.

James, I.D., A numerical model of the development of anticyclonic circulation in a gulf-type region of freshwater influence, *Continental Shelf Research*, *17* (14), 1803-1816, 1997.

James, I.D., Modelling pollution dispersion, the ecosystem and water quality in coastal waters: a review, *Environmental Modelling & Software*, *17* (4), 363-385, 2002.

Ludvigsen, M., I.H. Ellingsen, Ø.T. Ødegaard and B. Sortland, Model supported AUV freshwater distribution surveys in the upper layers of deep fjords, *OCEANS 2003*, 2003.

Luketina, D.A. and J. Imberger, Characteristics of Surface Buoyant Jet, *Journal of Geophysical Research*, *92* (C5), 5435- 5447, 1987.

Marmorino, G.O., C.Y. Shen, N. Allan, F. Askari, D.B. Trizna, C.L. Trump, and L.K. Shay, An occluded coastal oceanic front, *Journal of Geophysical Research*, *103* (C10), 21,587-21,600, 1998.

Marmorino, G.O. and C.L. Trump, Gravity current structure of the Chesapeake Bay outflow Plume, *Journal of Geophysical Research*, *105* (C12), 28,847- 28,861, 2000.

Martin, P.J., A description of the Navy Coastal Ocean Model Version 1.0, *NRL Report: NRL/FR/7322-009962*, *Naval Research Laboratory, Stennis Space Center*, 39, 2000.

Maxworthy, T., J. Leilich, J.E. Simpson and E.H. Meiburg, The propagation of a gravity current into a linearly stratified fluid, *Journal of Fluid Mechanics*, *453*, 371-394, 2002.

McClimans, T.A., Fronts in Fjords, *Geophysical Astrophysical Fluid Dynamics*, *11*, 23-34, 1978.

McClimans, T.A., Orklaforsøket, River and Harbour Laboratory Report STF60 A79094, 1979.

McClimans, T.A., River plumes in a rotating basin, River and Harbour Laboratory Report STF60 A80108, 1980.

McClimans, T.A., Laboratory simulations of river plumes and coastal currents, *ASME Paper FED*, *8*, 3-9, 1983.

McClimans, T.A., Estuarine Fronts and River Plumes, in *Physical Processes in Estuaries*, edited by J. Dronkers, and W. van Leussen, Springer-Verlag, 1988.

McClimans, T.A., Entrainment/detrainment along river plumes, in *Recent Research Advances in the Fluid Mechanics of Turbulent Jets and Plumes*, (P.A. Davies and Valente Neves, Ed.) Kluver Academic Publishers, 1994.

Mellor, G.L. and T. Yamada, Development of a turbulence closure model for geophysical fluid problems., *Geophysics and Space Physics*, *20*, 851-875, 1982.

Mellor, G.L., An equation of state for numerical models of oceans and estuaries, *Journal of Atmospheric and Ocean Technology*, *8*, 609-611, 1991.

Morey, S.L., P.J. Martin, J.J. O'Brien, A.A. Wallcraft and J. Zavala-Hidalgo, Export pathways for river discharged fresh water in the northern Gulf of Mexico, *Journal of Geophysical Research-Oceans*, *108* (C10), 3303, doi: 10.1029/2002JC001674, 2003.

Morey, S.L., W.W. Schroeder, J.J. O'Brien and J. Zavala-Hidalgo, The annual cycle of riverine influence in the eastern Gulf of Mexico basin,*Geophysical Research Letters*,*30*(16), 1867, doi:10.1029/2003GL017348, 2003.

Munk, W., Spirals on the sea, *Scientia Marina, 65*, 193-198, 2001.

Munk, W., L. Armi, K. Fischer, and F. Zachariasen, Spirals on the sea, Philosophical Transactions of the Royal Society of London: Mathematical, Physical and Engineering Sciences 456:1217-1280

O'Donnell, J., Convergence and Downwelling at a River Plume Front, *Journal of Physical Oceanography*, *28*, 1481- 1495, 1998.

Pond, S. and G.L. Pickard, *Introductory Dynamical Oceanography*, 329 pp., Butterworth -Heinemann, 1995.

Pritchard, M. and D.A. Huntley, Instability and Mixing in a smal Estuarine Plume Front, *Estuarine, Coastal and Shelf Science*, *55*, 275-285, 2002.

Sakshaug, E. and Å. Killingtveit, *Trondheimsfjorden*, 336 pp, Tapir forlag, 2000.

Shen, C.Y. and T.E. Evans, Inertial instability and sea spirals, *Geophysical Research Letters*, *29* (23), 2002.

Simpson, J.E., *Gravity Currents in the Environment and the Laboratory*, 244 pp., Cambridge University Press, 1997.

Stacey, M.W., Some Aspects of the Internal Tide in Knight Inlet, British-Columbia, *Journal of Physical Oceanography*, *15* (12), 1652-1661, 1985.

Stigebrandt, A., Vertical Diffusion Driven by Internal Waves in a Sill Fjord, *Journal of Physical Oceanography*, *6*, 7-17, 1976.

Stigebrandt, A., Some Aspects of Tidal Interaction with Fjord Constrictions, *Estuarine and Coastal Marine Science*, *11*, 151-166, 1980.

Stigebrandt, A. and J. Aure, Vertical mixing of basin waters of fjords., *Journal of Physical Oceanography*, *19*, 917-926, 1989.

Stommel, H. and H.G. Farmer, Control of the salinity in an estuary by a transition, *Journal of Marine Research*, *12*, 13-20, 1953.

Tang, Y.M., R. Grimshaw, B. Sanderson and G. Holland, A numerical study of storm surges and tides, with application to the North Queensland coast, *Journal of Physical Oceanography*, *26* (12), 2700-2711, 1996.

Turner, J.S., *Buoyancy effects in fluids*, Cambridge University Press, 1973.

Vlasenko, V., N. Stashchuk and K. Hutter, Water exchange in fjords induced by tidally generated internal lee waves, *Dynamics of Atmospheres and Oceans*, *35*, 63-89, 2002.

Wallace, J.M. and P. Hobbs, *Atmospheric Science. An introduction survey*, 467 pp., Academic Press. Inc., 1977.

Ødegaard, Ø.T., B. Sortland, I.H. Ellingsen, D. Slagstad, G. Johnsen and E. Sakshaug, An interdisciplinary marine research programme. How to promote generative interaction between marine scientists, modellers and engineers, *OCEANS 2002*, *1*, 595-602, 2001.